UNIVERSITY OF CALIFORNIA, MERCED

Photophysical Properties of II-VI Semiconductor Nanocrystals

by

Ke Gong

A dissertation submitted in partial satisfaction of the requirements for the degree Doctor of Philosophy

in

Chemistry and Chemical Biology

in the

Graduate Division

of the

University of California, Merced

Dissertation Committee:

Professor Anne M. Kelley, Chair
Professor David F. Kelley, Advisor
Professor Tao Ye
Professor Michael Scheibner

2015

The dissertation of Ke Gong, titled *Photophysical Properties of II-VI Semiconductor Nanocrystals*, is hereby approved:

_____ Date: _____
David F. Kelley

_____ Date: _____
Tao Ye

_____ Date: _____
Michael Scheibner

Chair: _____ Date: _____
Anne M. Kelley

University of California, Merced

TABLE OF CONTENTS

PAGE

ACKNOWLEDGEMENTS

I would like to express my great thanks in many forms. First of all, financial support from teaching assistant positions in general chemistry, as well as GSR positions funded by two grants from National Science Foundation and Department of Energy, were the primary means of support. These positions allowed me to complete my degree in four and a half years by concentrating most of my time and energy on research.

Most importantly, I want to express my deepest thanks and appreciation to my advisor, Professor. David F. Kelley. His continuous guidance and encouragement enlightened and supported me during my graduate career. Without Prof. Kelley's effective direction, patience, creative ideas, and solid scientific knowledge, to complete this huge amount of work would not have been possible. It should be acknowledged that some parts of this dissertation come from articles written and supervised by Prof. Kelley. My honest thanks go to him for these essential contributions.

I would give my extended gratitude to Professor. Anne M. Kelley, who shares great spectroscopic knowledge and distinctive points of view in the research, as well as the members of Dr. Kelley's joint group, specifically Dr. Zhongjie Jiang, Dr. Gary Beane, Dr. Chen Lin and Youhong Zeng. I also would also like to give thanks to Sandia National Laboratories and their staff for measurement of TEM images and temperature dependent optical properties that were crucial to the progress of my dissertation.

Finally, I would like give my best regards to my family - my wife and new born baby, Mathew especially. Their continuous and warm support gave me a strong determination to finish the dissertation and my Ph.D at UC Merced.

The text, figures and tables of this dissertation is a reprint of the materials as they appear in the Journal of Physical Chemistry C, Journal of Physical Chemistry Letter (American Chemical Society journals) and Journal of Chemical Physics (American Institute of Physics journal). The co-authors, David Kelley, Youhong Zeng, Gary Beane and Xichen Cai from UC Merced and James E. Martin, Lauren E. Shea-Rohwer and Ping Lu from Sandia National Laboratories listed in these publications directed, supervised and participated research which form the basis for the thesis/dissertation.

CURRICULUM VITAE

WORK SUMMARY

Research Area: synthesis, spectroscopy, photophysics and photochemistry of semiconductor nanostructures, quantum dot based LEDs and solar cells

Lab Skills: expertise in nano-structure design, femtosecond pump-probe transient absorption technology, time-correlated single photon counting technology, thin film fabrication

Teaching Experience: quantum chemistry, general chemistry, solid state physics

---

EDUCATION

Ph.D. PI: David F. Kelley

Chemistry, University of California, Merced, 2015

M.S. PI: Gregory Kalyuzhny

Chemistry, San Diego State University, US, 2011

B.S. PI: Haiqian Zhang

Applied Chemistry, Nanjing University of Aeronautics and Astronautics, China, 2006

RESEARCH (Founding Resources: *DOE*, *NSF*, *ERFC Sandia National Lab*)

- Study of shell inhomogeneity, lattice strain limitation and strain release caused trapping process of CdSe/CdS quantum dots (QDs), 2013-2015
- Study of surface-charging created positive trion of CdSe based core/shell QDs, 2014-2015
- Study of effects of solvent and interfacial sharpness on trion Auger process of CdSe based core/shell QDs, 2014-2015
- Mechanistic study on thermal quenching of II-VI quantum dots, 2012-2013
- Raman study on II-VI CdSe QDs and CdSe-based core/shell QDs, 2013-2015
- Study on extinction coefficients, oscillator strengths and radiative lifetime of CdSe, CdTe, CdTe/CdSe, and CdSe/CdS QDs, 2012-2015
- Fabrication of QD-polymer complex, surface derivation and bio-labeling of QDs, 2008-2011
- Synthesis and optical properties of ultra-small ZnSe and ZnTe nanowires&nanoplatelets, InSe, $CuInSe_2$ (CIS) nanosheets and Cu_2ZnSnS_4 (CZTS) nanoparticles, 2009-2011
- Photovoltaic device fabrication of II-VI semiconductor quantum dots (QDs), 2010-2011

PROFICIENT SKILLS

- **Device Fabrication**: spinning-coating, chemical deposition, lithography
- **Materials Characterization**: SEM, TEM, XRD, FT-IR, UV-Vis and Fluorescence spectroscopy, photoconductivity and electroluminescence testing, Mass spectroscopy, NMR, HPLC, atomic absorption
- **Electrochemistry**: CV, SWV, DPV

- **Programming/Graphing**: LabVIEW, Fortran, Matlab, Digital Micrograph, Origin

---

ACADEMIC ACHIEVEMENT

Papers In Preparation

- ***Ke Gong***, Gary Beane and David Kelley. Auger and Electron Trapping Dynamics in Core/Shell Quantum Dots Having Sharp and Alloyed Interfaces.. In Preparation.
- Jamie Grenland, Chen Lin, ***Ke Gong***, David F. Kelley, and Anne Myers Kelley. Resonance Raman Investigation of Interaction between Aromatic Dithiocarbamate Ligands and CdSe Quantum Dots. In Preparation.

Peer-Reviewed Papers

- ***Ke Gong***, Gary Beane and David Kelley. Strain Release in Metastable CdSe/CdS Quantum Dots. *Special Issue, Chemical Physics*, 2015
- Chen Lin, ***Ke Gong***, David F. Kelley, and Anne Myers Kelley. Electron-Phonon Coupling in CdSe/CdS Core/Shell Quantum Dots. *ACS Nano*, 9, 8131-8141,2015
- ***Ke Gong*** and David Kelley. Lattice Strain Limit in Uniform Shell Deposition in Zincblende CdSe/CdS Quantum Dots, *JPC Letters*, 6, 1559-1562, 2015.
- ***Ke Gong*** and David Kelley. Surface Charging and Trion Dynamics in CdSe based Core/Shell Quantum Dots. *JPCC*, 119, 9637-9645, 2015.
- Chen Lin, ***Ke Gong***, David Kelley and Anne Kelley. Size-Dependent Exciton-Phonon Coupling in CdSe Nanocrystals Through Resonance Raman Excitation Profile Analysis. *JPCC*, 119, 7491-9498, 2015.
- ***Ke Gong***, James E. Martin, Lauren E. Shea-Rohwer, Ping Lu and David Kelley. Radiative Lifetimes of Zincblende CdSe/CdS Quantum Dots. *JPCC* , 119, 2231-2238, 2015.
- ***Ke Gong*** and David Kelley. A Predictive Model of Shell Morphology in CdSe/CdS Core/Shell Quantum Dots. *The Journal of Chemical Physics*, 141,19704, 2014.
- ***Ke Gong***, Youhong Zeng and David Kelley. Extinction Coefficients, Oscillator Strengths and Radiative Lifetime of CdTe, CdSe and CdTe/CdSe Nanocrystals. *JPCC*, 117, 20268-20279, 2013.
- Xichen Cai, James E. Martin, Lauren E. Shea-Rohwer, ***Ke Gong*** and David Kelley. Thermal Quenching Mechanism in II-VI Semiconductor Nanocrystals. *JPCC*, 117, 7902-7913, 2013.
- ***Ke Gong***, Haiqian Zhang. Research on the Reinforcing Influence of Silane Coupled Carbon Fiber Reinforced Plastic. *Journal of Lubrication Engineering*, 32(4), 142-144, 2007.

Presentation

- "Thermal quenching mechanism in II-VI semiconductor nanocrystals". Xichen Cai, James E. Martin, Lauren E. Shea-Rohwer, ***Ke Gong*** and David Kelley, EFRC PI meeting, **2013**
- "Thermal quenching mechanism in II-VI quantum dots". Xichen Cai, James E. Martin, Lauren E. Shea-Rohwer, ***Ke Gong*** and David Kelley, 61st Pacific Conference on Spectroscopy and Dynamics, **2013**
- "Synthesis and optical properties of nanocrystals, nanowires and nanoplates of ZnSe and ZnTe". ***Ke Gong***, Aaron C. Johnston-Peck, Joseph B. Tracy and Gregory Kalyuzhny, 241st ACS National Meeting & Exposition, **2011**
- "Synthesis, Chemical and Optical Properties of Magic-Size Semiconductor Nanocrystals (MSNCs)". Minho Jung, ***Ke Gong***, Stephen Cook, and Gregory Kalyuzhny, Gordon Research Conference on Clusters, Nanocrystals& Nanostructures, **2009**

Thesis and Dissertation

- **Ke Gong**. Photophysical Properties of II-VI Semiconductor Nanocrystals, Ph.D Dissertation.

(2015 Fall expected)

- **Ke Gong**. Synthesis, Optical properties and Surface modification of Magic-size Semiconductor Nanocrystals, Nanowires and Nanoplatelets. M.S. Thesis, 2011.
- **Ke Gong**, Synthesis and Biological Functionalization of CdS Fluorescent Quantum Dots. Excellent Diploma Thesis, 2006.

ACTIVITIES

- Membership of American Chemical Society, 2011-2014
- Graduate Student Researcher, University of California, Merced, 2012-2015
- Teaching Assistant for Inorganic& General Chemistry, University of California, Merced, 2011, 2014
- Teaching Assistant for General Chemistry, San Diego State University, 2008-2011

HONORS & AWARDS

- Graduate Dean Dissertation Fellowship, 2015-2016
- Summer Research Fellowship (Chemistry and Chemical Biology), 2013-2015
- Edgar E. & Catherine L. Hardy Scholarship, 2010
- First Class Scholarship for Excellent Graduate Student and Merit Graduate Student, 2006-2007
- First Class Scholarship for Excellent Student and Merit Undergraduate Student, 2002-2006

LIST OF FIGURES

PAGE

LIST OF TABLES

PAGE

ABSTRACT OF DISSERTATION

Title: Photophysical Properties of II-VI Semiconductor Nanocrystals
Name: Ke Gong
Degree: Doctor of Philosophy
Institution: University of California, Merced, 2015
Committee Chair: Anne M. Kelley

As it is well known, semiconductor nanocrystals (also called quantum dots, QDs) are being actively pursued for use in many different types of luminescent optical materials. These materials include the active media for luminescence downconversion in artificial lighting, lasers, luminescent solar concentrators and many other applications. Chapter 1 gives general introduction of QDs, which describe the basic physical properties and optical properties. Based on the experimental spectroscopic study, a semiquantitative method-effective mass model is employed to give theoretical prediction and guide. The following chapters will talks about several topics respectively. A predictive understanding of the radiative lifetimes is therefore a starting point for the understanding of the use of QDs for these applications. Absorption intensities and radiative lifetimes are fundamental properties of any luminescent material. Meantime, achievement of high efficiency with high working temperature and heterostructure fabrication with manipulation of lattice strain are not easy and need systematic investigation.

To make accurate connections between extinction coefficients and radiative recombination rates, chapter 2 will consider three closely related aspects of the size dependent spectroscopy of II-VI QDs. First, it will consider the existing literature on cadmium selenide (CdSe) QD absorption spectra and extinction coefficients. From these results and fine structure considerations Boltzmann weighted radiative lifetimes are calculated. These lifetimes are compared to values measured on very high quality CdSe and CdSe coated with zinc selenide (ZnSe) shells. Second, analogous literature data are analyzed for cadmium telluride (CdTe) nanocrystals and compared to lifetimes measured for very high quality QDs. Furthermore, studies of the absorption and excitation spectra and measured radiative lifetimes for CdTe/CdSe Type-II core/shell QDs are reported. These results are also analyzed in terms of a Boltzmann population of exciton sublevels and calculated electron and hole wave functions. Much of the absorption data and fine structure calculations are already in the literature. These results are combined with new measurements of radiative lifetimes and electron-hole overlap calculations to produce an integrated picture of the II-VI QD spectroscopic fundamentals. Finally, we adopt recent synthetic advances to make very monodisperse zincblende CdSe/CdS quantum dots having near-unity photoluminescence quantum yields (PLQYs). Due the absence of nonradiative decay pathways, accurate values of the radiative lifetimes can be obtained from time resolved PL measurements. Radiative lifetimes can also be obtained from the Einstein relations, using the static absorption spectra and the relative thermal populations in the angular momentum sublevels. One of the inputs into these calculations is the shell thickness, and it is useful to be able to determine shell thickness from spectroscopic measurements. We use an empirically corrected effective mass model to produce a "map" of exciton wavelength as a function of core size and shell thickness. These calculations use an elastic continuum model and the known lattice and

elastic constants to include the effect of lattice strain on the band gap energy. Radiative lifetimes calculated both experimentally and theoretically are checked and the size dependence is compared to previous studied Type-I, II and single component particles.

However, it is not enough to just understanding these basic photophysics of absorption and emission. The emission intensities (related to QYs) also change with changes of the temperature. The temperature dependent PLs of II-VI QDs is extensively studied, but most of this work is at low temperatures. Temperatures well above ambient are of interest to lighting applications and in this regime both the reversible and irreversible loss of quantum yield (thermal quenching) are serious impediments to the implementation of QDs in commercial devices. Chapter 3 will elucidate the mechanism of static thermal quenching, in which the reduction of QYs does not affect the PL decay kinetics, on CdSe, CdTe and CdSe/ZnSe QDs as a function of particle sizes/shapes, surface composition and surface ligands. Through systematic experiments, this part of the dissertation discusses several possible mechanisms (e.g. structural, activated excited state, and electronic charging) and examines which the dominant cause for loss of QY at high temperature is. The more practical step is to develop the synthetic method of highly luminescent and stable core/shell QDs with minimum thermal quenching, which greatly enhance the energy efficiency of light emitting and photovoltaic devices.

As the nonradiative Auger processed are induced by surface charging described in chapter 3, static and time-resolved fluorescence and high and low power transient absorption results on CdSe/CdS and CdSe/ZnSe core/shell particles are presented in chapter 4. Two CdS shell thicknesses were examined and all of the particles had either octadecylamine (ODA) and tributylphosphine (TBP) or just ODA ligands. The results can be understood in terms of a mechanism in which there is a thermal equilibrium between electrons being in the valence band or in chalcogenide localized surface states. Thermal promotion of a valence band electron to a surface state leaves the particle core positively charged. Photon absorption when the particle is in this state results in a positive trion, which undergoes a fast Auger recombination, making the particle nonluminescent. A lack of TBP ligands results in more empty surface orbitals and therefore shifts the equilibrium toward surface trapped electrons and hence trion formation. Low- and high-power transient absorption measurements give the trion and biexciton lifetimes and the ratio of the trion to biexciton Auger lifetimes are examined and compared to the degeneracies of Auger pathways. We also study the shell thickness and composition dependence of Auger times, which is compared to the scaling factors of effective volume and electron-hole overlap considerations.

Core/shell QDs often exhibit much higher luminescence quantum yields (QYs), more stability, and are depicted as having a nearly spherical core and a shell of very nearly uniform thickness, which results in a very simple picture of surface passivation. The uniformity of the shell is crucial in obtaining QDs with well passivated surfaces. However, transmission electron microscope (TEM) images disprove the ideal situation. Defects and thickness inhomogeneity in shell materials are treated qualitatively as an analog to film thickness inhomogeneity in epitaxially grown thin films. More quantitatively, the extent to which the shell thickness of core/shell particles is constant can be determined by time-resolved PL studies that measure the dynamics of hole tunneling to acceptors that are adsorbed on the shell surface due that tunneling rates varies strongly with core-acceptor separation. Careful

analysis of the hole transfer kinetics reveals the extent of shell thickness inhomogeneity, however, it may be complicated by the distribution of numbers of adsorbed acceptors. All the considerations can be incorporated into a model we establish in Chapter 5for the distribution of measured hole tunneling rates. From this analysis the distribution of shell thicknesses can be extracted from the luminescence kinetic results. This approach is therefore a sensitive measure of the distribution of tunneling distances. Thus, any defects or structural irregularities that allow the hole acceptors to adsorb closer to the particle core increases the hole tunneling rate and can be detected and quantified.

A quantitative treatment of the lattice strain energy in determining the shell morphology of CdSe/CdS core/shell nanoparticles is presented in chapter 5. We use the inhomogeneity in hole tunneling rates through the shell to adsorbed hole acceptors to quantify the extent of shell thickness inhomogeneity. The results can be understood in terms of a model based on elastic continuum calculations, which indicate that the lattice strain energy depends on both core size and shell thickness. This model assumes thermodynamic equilibrium, i.e., that the shell morphology corresponds to a minimum total (lattice strain plus surface) energy. Comparison with the experimental results indicates that CdSe/CdS nanoparticles undergo an abrupt transition from smooth to rough shells when the total lattice strain energy exceeds about 27eV or the strain energy density exceeds 0.59 eV/nm^2.

The predictions of this model are not followed for CdSe/CdS nanoparticles when the shell is deposited at very low temperature and therefore equilibrium is not established. The effects of lattice strain on the spectroscopy and photoluminescence quantum yields of zincblende CdSe/CdS core/shell quantum dots are examined. The quantum yields are measured as a function of core size and shell thickness. High quantum yields are achieved as long as the lattice strain energy density is below ~0.85 eV/nm^2, which is considerably greater than the limiting value of 0.59 $eV/nm^2$for thermodynamicstability of a smooth, defect free shell, as previously reported in chapter 5. Thus, core/shell quantum dots having strain energy densities between 0.59 and 0.85 eV/nm^2 can have very high PL QYs, but are metastable with respect to surface defect formation. Such metastable core/shell QDs can be produced by shell deposition at comparatively low temperatures (< 140 °C).Annealing of these particles causes partial loss of core pressure, and a red shift of the spectrum.

CHAPTER 1. GENERAL INTRODUCTION TO SEMICONDUCTOR NANOCRYSTALS

1.1Basic properties

Semiconductor nanocrystals are small nanocrystals with the size range from a few nanometers (nm,10^{-9} m) to tens, even hundreds of nanometers. In bulk materials, physical, chemical and optical properties are not affected by the size and have been well studied in the past decades. However, these nanocrystals exhibit properties that are strongly dependent on their size, shape and morphology. When the size of a spherical nanocrystal is smaller than the corresponding bulk Bohr radius, the free charge carriers experience "quantum confinement" in all three spatial dimensions. As a result, the electronic properties of quantum dots are intermediate between those of bulk semiconductors and molecules, and the electronic energy levels are "quantized". That is why these semiconductor nanocrystals are also called quantum dots (QDs).

The QDs we studied here involve transition metal element (Group 12, 2B) and chalcogen group element (Group 16, 6A). The synthesized II-VI metal chalcogenide QDs in this dissertation contains cadmium selenide (CdSe), cadmium telluride (CdTe), cadmium sulfide (CdS) and zinc selenide (ZnSe).

The first physical property everyone wants to know is the crystalline structure. Similar to their bulk counterparts, the II-VI QDs usually have wurtzite and (or) zincblende (ZB) structures. The compounds that crystallize with ZB arrangement include zinc sulfide (ZnS), gallium arsenide (GaAs), zinc telluride (ZnTe) and CdTe. It is same as the diamond structure seen in the case of single-element crystals in which it has a face-center-cubic (FCC) unit cell. However, the wurtzite structure has a version of the single-element hexagonal close-packed structure like the diamond and the materials with this structure include CdS and CdSe. In some cases, some materials could have either or both crystalline structures, which depends on the synthetic conditions used to synthesize the particle, particle ligand/solvent interaction and impurities.

The second is the lattice mismatch between seeded core material and deposited shell material during epitaxial growth. To fabricate the so-called core/shell heterostructures, the mismatch will play a great role and will greatly affect the shell condition and optical properties.

The third is the shape and morphology, which will be well illustrated by the transmission electron microscopy (TEM). The shapes are well correlated with synthetic conditions. Usually, the high temperature with strong coordinating ligands will generate rod-like QDs and medium temperature with weak/medium coordinating ligands will yield spherical QDs. Low-dimensional nanomaterials, like nanodisks and nanoplates can be synthesized with quite low temperatures. With the assistance of strong-binding ligands, like phosphonic acid, the shell on the wurtzite and zinc blende cores will tend to form dot-rod and dot-tetrapod morphologies respectively. In Chapter 5 the effect of lattice strain arising from the lattice mismatch on shell morphology and related topics is systematically studied.

1.2Optical properties

When quantum dots are photoexcited, the incident photon excites an electron from the valence band (VB) into the conduction band (CB), leaving behind a hole in the VB. The bound state of an electron-hole pair is called an “exciton”. The energy difference between the bottom of the CB and the top of VB is called “band gap”. The band gaps of bulk II-VI semiconductor materials are listed in figure 1.1. On top of figure 1.1, the percentage number

indicates the lattice mismatch between that specific material and CdSe and the row below gives the values of bulk band gap.

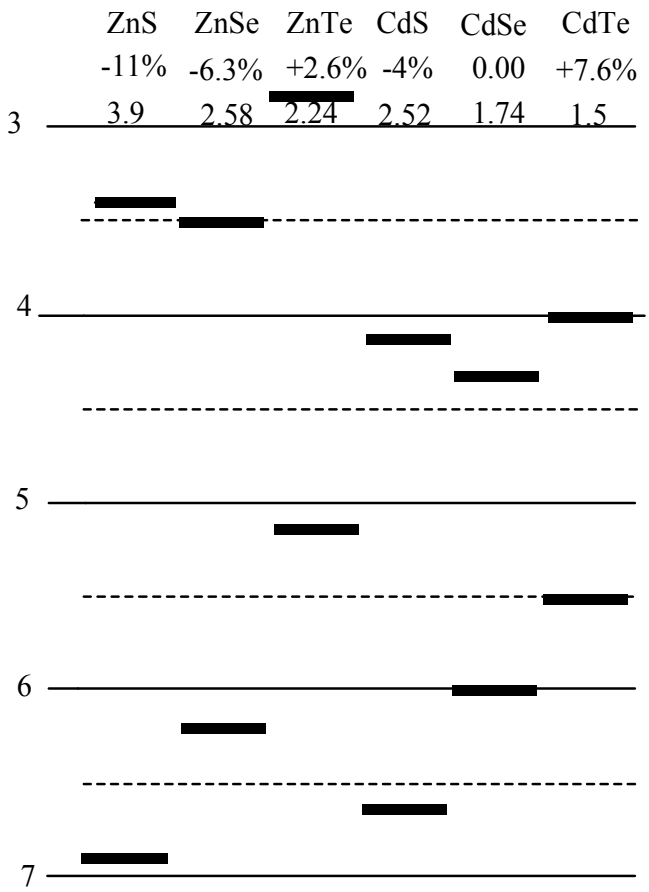

Figure 1.1. Band alignments of bulk II-VI semiconductor materials. The energy has units of electron volts (eV).

Based on the band energy offsets, there are three types of core/shell heterostructures. The first and most common is Type-I structures, in which the energy of CB and VB of the core material are lower and higher than those of the shell, respectively. Therefore, the photo-generated exciton (both electron and hole) will be confined in the core. This kind of material includes CdSe/ZnSe, CdSe/ZnS, and CdS/ZnS. As the exciton is relatively separated from surface states which may act as hole or electron traps, the emission quantum yields of Type-I are usually better than bare core.

The second is Type-II structure, in which the energies of CB and VB of the core particle are both higher than those of CB and VB of the shell material and vice versa, such as CdTe/CdSe and ZnTe/CdSe. In the former case, the electron is delocalized into shell, but the hole is still confined in the core. The electron-hole overlap decreases with the increasing shell thickness. Surprisingly, the common Type-II structures significantly enhance the quantum yield.

The last is “Type-1½” or “quasi-type-II” structures, like CdSe/CdS QDs. The CB is almost degenerate with tiny band offset but large VB offset confines the hole in CdSe. In this dissertation, we will investigate CdSe/ZnSe, CdTe/CdSe and CdSe/CdS QDs.

Relating optical properties, absorption and emission processed are most concerned and connected through Einstein coefficients. These quantities will be detailed in chapter 2, including integrated extinction coefficients, radiative lifetimes and oscillator strength. In most expressions, there is a refractive index factor. It arises from the relationship between energy density and electric field in a dielectric medium. This quantity is more generally a complex quantity given by $n + i\kappa$, and it depends on frequency. Far from any resonances, where the material is essentially nonabsorbing, the refractive index is essentially purely real and varies only slowly with frequency. Typical refractive indices for the visible and near-infrared region are around 1.3 to 1.7 for most liquids, and often larger for crystals. As the integrated absorption cross-section scales as 1/n, absorption strengths can also differ in different environments because of local field effect. The specific case related to CdSe/CdS will be explained in chapter 2.

1.3A theoretical tool

To understand the spectroscopic properties of QDs, effective mass models (EMM) are employed to give semiquantitative guide. The quantitative description of size-dependent electronic properties, the particle-in-a-sphere model is introduced. Generally, this model assumes an arbitrary particle with effective masses in a spherical potential well of certain radius. The corresponding wavefunction is a product expression of spherical harmonic and spherical Bessel function over the radius. The wavevector is the n-th zero of a specific Bessel function divided by the radius of the sphere, which allows the energy of the particles to be solved. The particle described here is confined to an empty sphere, but the nanoparticle consists of semiconductor atoms. With these approximations, the nanocrystal problem now is reduced to the particle-in-a-sphere form and the photogenerated electron and hole can be treated as particles moving in a sphere of constant potential.

Within the effective mass approximation (EMA), the bulk conduction and valence bands are treated as simple isotropic bands. According to Bloch's theorem, the electronic wavefunction is in a bulk crystal is a product of a function with periodicity of the crystal lattice and an envelope function, called Bloch functions. The energy of these wavefunctions is typically depicted in a band diagram, a plot of energy (E) versus wavevector (k). From the diagram, the effective mass (m*) accounts for the curvature of the CB and VB at k=0. (see figure 1.2) and the energy of the CB (E_c) and VB (E_v) are described as equations 1.1 and 1.2

$$E_c=\hbar^2k^2/(2m_e^*)+E_g \qquad \text{equation. 1.1}$$

$$E_b=-\hbar^2k^2/(2m_h^*) \qquad \text{equation. 1.2}$$

where Eg is the bulk band gap, m_e^* and m_h^* are the effective mass of electron and hole. With the help of EMA, the semiconductor atoms in the lattice are ignored and the electron and hole are treated just as free moving particles, but with smaller mass compared to stationary mass (m_0). For instance of CdSe QDs, $m_e^*=0.11\ m_0$ and $m_h^*=0.44\ m_0$.

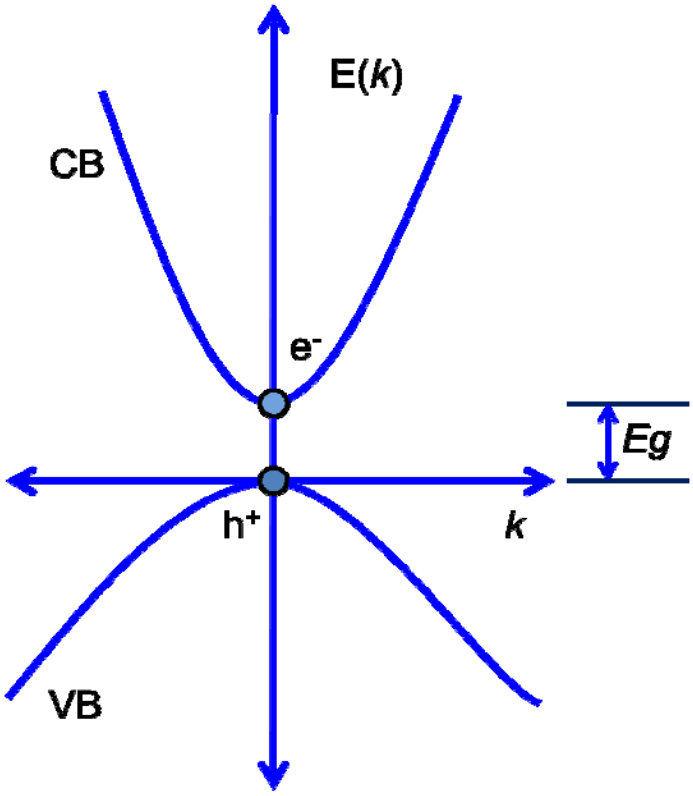

Figure 1.2. Band diagram for a simple two band model for quantum dots. Eg is the bulk band gap.

To use EMA in the case of nanocrystals, we have to assume the crystallites can be treated as a bulk sample. Then, the wavefunction in a single particle is written as a linear combination of Bloch functions, in which the expansion coefficients ensure that the sum of the wavefunction satisfies the spherical boundary condition of the nanocrystal. If the periodic function has a weak dependence on k, then the wavefunction is approximated as the periodic function (at k=0) multiplied by the single particle envelope function. The former component can be estimated with approximation of linear combination of atomic orbitals, and the left part is addressed by the particle-in-a sphere model mentioned previously. For spherical nanocrystals with a potential barrier that is approximated as infinitely high, the envelope functions of the carriers are given by the particle-in-a-sphere solutions.

For II-VI QDs, the CB is well described with EMA because it arises only from s orbital of the cation with J=1/2 (double degeneracy) at k=0. However, the VB comes from p atomic orbitals and 6-fold degenerate at k=0, including the spin. The simple VB diagram shown in figure 1.2 is not a good approximation any more, and this 6-fold degeneracy gives rise to VB substructures.

While the bands are still treated to be parabolic, due to strong spin-orbit coupling, the VB degeneracy at k=0 is split into $J_{3/2}$ and $J_{1/2}$ subbands, where the subscript stands for the total angular momentum J=l+s., where l and s are the orbital and spin contribution to the total angular momentum. Away from k=0, the $J_{3/2}$ band is further split into $J_m=\pm 3/2$ and $J_m=\pm 1/2$ subbands, where J_m is the projection of J. The former and latter one stands for heavy hole

(hh) and light hole (lh), respectively. However, the $J_{1/2}$ band is well separated from $J_{3/2}$ bands, and referred to as the split-off-hole (soh) subbands. The arrangement of these subbands is shown in figure 1.3.

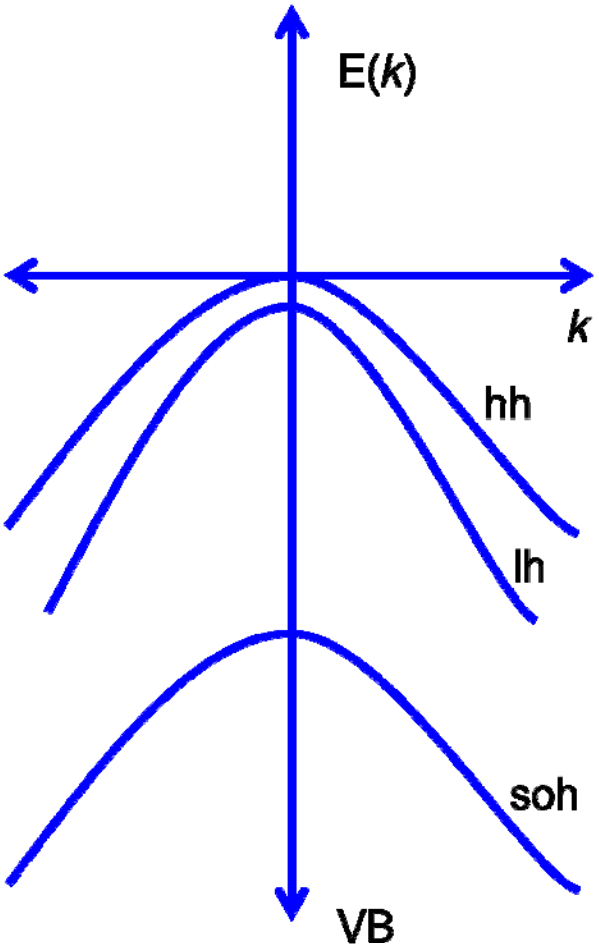

Figure 1.3. Band diagram for valence band model of II-VI QDs (e.g. CdSe).

The fine structure of lowest energy exciton (band-edge exciton) arises from the shape anisotropy and electron-hole exchange interaction. In figure 1.4, the band-edge exciton of wurtzite CdSe is split into two 4-fold degenerate states due to the reduction from spherical shape to uniaxial symmetry. As the exchange interaction is proportional to the overlap between the electron and hole, in small nanocrystal the exchange interaction will further split the states. In this case, the important quantum number is the total angular momentum, J. Because of angular momentum of hole and electron is 3/2 and 1/2, the band-edge exciton has a 5-fold degenerate J=2 states and a 3-fold degenerate J=1 states. If both effects are included, the good quantum number is the projection of J along the unique crystal axis, J_m.

Figure 1.4. Energy-level diagram of fine structures of the band-edge exciton. In the sphere, the band-edge exciton is 8-fold degenerate. This degeneracy is split by the shape anisotropy, wurtzite c-axis and the exchange interaction.

The $J_m=\pm2$ sublevels are optically forbidden in the electric dipole approximation, therefore no emission is observed from this state. Relaxation of the exciton into this state is referred to the *dark* exciton, which will cause longer radiative lifetime. Because two units of angular momentum are required to relax to the ground state from $J_m=\pm2$ sublevels, and this process is forbidden by the approximation of electric dipole transition. The energy levels and absorption strengths of these sublevels are shape and size dependent and the overall fine structure effect is detailed in chapter 2.

CHAPTER 2. EXTINCTION COEFFICIENTS, OSCILLATOR STRENGTHS AND RADIATIVE LIFETIMES OF CDSE, CDTE, CDTE/CDSE AND CDSE/CDS NANOCRYSTALS.

2.1 Introduction of fundamental spectroscopy

Semiconductor quantum dots (QDs) are small particles with size range from several nanometers to tens of nanometers, which confines the motion of conduction band electrons and valence band holes, or excitons (bound pairs of conduction band electrons and valence band holes) in all three spatial directions. The unique size-dependent optical properties are actively investigated for use in various luminescent optical materials, such as the active media for luminescence downconversion artificial lighting, lasers, luminescent solar concentrators and so on. To accurately predict the radiative lifetimes is a starting point for the design of QDs based applications.

Absorption intensities and radiative lifetimes are two basic quantities for luminescent materials. Both are related to the oscillator strength in a very straight forward way through the Einstein A and B coefficients. The radiative rate can be calculated for a single oscillator from the integrated extinction coefficient.[1]

$$A = \frac{8\pi\ 0.2303\, n_f^3}{N_a\, c^2\, n_a} \left\langle \nu_f^{-3} \right\rangle^{-1} \int \frac{\varepsilon(\nu)}{\nu} d\nu \approx 2.88x10^{-9} n^2 \left\langle \tilde{\nu}_f^2 \right\rangle \int \varepsilon(\tilde{\nu})\, d\tilde{\nu} \qquad \text{equation. 2.1}$$

where N_a is Avogadro's number, c is the speed of light, $\varepsilon(\nu)$ is the molar extinction coefficient ($Lmol^{-1}cm^{-1}$) at frequency ν, ν_f ($\tilde{\nu}_f$) is the fluorescence frequency (wavenumber), brackets denote an averaged quantity, and n_a and n_f and the refractive indices of the surrounding solvent at the absorption and luminescence frequency, respectively. In a good assumption that the absorption and luminescence spectra are narrow (full with at half maxima, FWHM ~ 27 nm) and the Stokes shift is less than 10 nm, the left part of equation 2.1 will equal to the right side with $n = n_a = n_f$. A closely related quantity is the oscillator strength, given by[1c]

$$f = \frac{4m}{e^2} \frac{0.2303\, n_a c \varepsilon_0 \left\langle \nu_a \right\rangle}{N_a \left| f_{LF} \right|^2} \int \frac{\varepsilon(\nu)}{\nu} d\nu \qquad \text{equation. 2.2}$$

where m is the electron mass, e is the electron charge, ε_0 is the permittivity of free space, f_{LF} is the local field factor, the correction for the magnitude of the electromagnetic field inside the dielectric material. In equation 2.2, f_{LF} is evaluated with the dielectric parameters at the absorption frequency. Local field factors can be far from unity with large deviation[2] and the calculation of the oscillator strengths will give various values based on variation of local field factors.. From equation 2.2, the equation will be converted to

$$A = \frac{2\pi \left(n_f^3 / n_a^2 \right) e^2 \left(\left\langle \nu_a \right\rangle^{-1} / \left\langle \nu_f^{-3} \right\rangle \right) \left| f_{LF} \right|^2}{\varepsilon_0 mc^3} f \simeq \frac{2\pi n e^2 \nu^2 \left| f_{LF} \right|^2}{\varepsilon_0 mc^3} f \qquad \text{equation. 2.3}$$

where in this case f_{LF} is evaluated with the dielectric parameters at the fluorescence frequency. If the Stokes shift is small (a good approximation for spherical nanoparticles), then the dielectric parameters at the absorption and fluorescence frequencies are the same, giving equal local field factors for absorption and fluorescence. Therefore, the local field factors cancel in the relationship between the integrated extinction coefficients and the radiative lifetime, equation 2.1. Now it gives a very simple conclusion for the case of absorption and fluorescence from a single oscillator, equation 2.1 is easy to evaluate if the ε(ν) spectrum is available. Because of the local field factors, evaluation of the oscillator strengths is more problematic. But most importantly, since the quantities that are most

frequently obtained from and used in experiments are the spectra and radiative lifetimes, these are the quantities with which we will be most concerned in chapter 2.

In spite that the equation 2.1 is quite simple with two quantities to solve, there have been few attempts to quantitatively connect absorption spectra and radiative rates of QDs. This is mainly because determination of these rates and comparing measured values to those calculated from the absorption spectra is not easy to do; reliable and accurate measurements of integrated extinction coefficients and radiative lifetimes are not easy to make. Furthermore, evaluation of equation 2.1 is complicated by the fact that in the II-VI QDs, there is a Boltzmann population of different exciton levels, some of which have allowed and some of which have forbidden transitions to the ground state. Thus, following photon absorption, relaxation occurs to different bright and dark states. Therefore, luminescence comes from a temperature-dependent distribution of states, each having its own oscillator strength and radiative rate. The Boltzmann populations in these different angular momentum sublevels depend on the sizes and shapes of the QDs. Generally, the Boltzmann-weighted average of these relaxation rates is referred as the radiative rate for the exciton.[3] In the absence of carrier trapping and non-radiative processes, this is the intrinsic luminescence decay rate.

On one hand, it is not trivial to determine size-dependent extinction coefficients, which accompanies with several underlying problems. The straightforward way to do is: just measure the absorption spectrum and the mass of the QDs precipitated from a known volume of solution. If the QD size is known from TEM imaging, then the extinction coefficient can be easily calculated. However, there are definitely some unreacted precursors in a QD sample and an unknown mass of organic ligands on the precipitated particles. Both of these problems complicate determination of the ε(ν) spectrum. Subsequent evaluation of equation 2.1 requires knowing the energetics and spectroscopy of the angular momentum fine structure. The lowest energy exciton in II-VI semiconductor nanocrystals has thermally accessible sublevels that that have large oscillator strengths as well as sublevels that are "dark", having zero oscillator strength.[4] The expression of thermal populations in the angular momentum fine structure, C_{fs} is given by[5]

$$C_{fs} = \frac{\sum_i f_i \exp(-E_i / k_B T)}{\sum_i \exp(-E_i / k_B T)} \qquad \text{equation.2.4}$$

where k_B is the Boltzmann constant, E_i and f_i is the energy and fraction of the total absorption oscillator strength in the *i'th* transition, respectively. There are eight thermally accessible angular momentum sublevels in the $1S_e$-$1S_{3/2}$ exciton. Rapid equilibration with the population of the dark states effectively increases the radiative lifetime. This is not a small effect; in the absence of crystal field mixing, five of the eight fine structure sublevels are dark. These states are separated by energies on the order of several to several tens of meV. Their relative energies, and hence their thermal populations depend strongly on particle size and shape. This analysis is further complicated by the fact that in wurtzite nanocrystals the crystal field mixes and shifts dark and bright states in a way that is also size and shape dependent. In addition to thermal populations of the lowest energy exciton ($1S_e$-$1S_{3/2}$)sublevels, the (dark) $1S_e$-$1P_{3/2}$ exciton is also thermally accessible,[6] with energies and hence relative populations that are also size dependent. The effect of size-dependent populations and oscillator strengths of these states must be considered in a calculation of the radiative lifetime in these nanocrystals.

On the other hand, it is more problematic of accurate measurement of the radiative lifetimes. QD ensembles are typically quite inhomogeneous, showing strongly nonexponential photoluminescence (PL) decays. The nonexponential PL decays are mainly due to inhomogeneities in the nonradiative rates, which means that different particles have different types of defects that can serve as nonradiative recombination centers. For any subset of the particles having the same nonradiative rate, the observed decay time is related to the sum of radiative and nonradiative rates.

$$\tau_{obs} = \left(k_{rad} + k_{nr}\right)^{-1} = \left(\tau_{rad}^{-1} + \tau_{nr}^{-1}\right)^{-1} \qquad \text{equation. 2.5}$$

Inhomogeneous values of the nonradiative rate, k_{nr}, result in a nonexponential PL decay from an ensemble of particles. Each value of k_{nr} gives a different decay time and thus a different component in the overall ensemble PL decay. For any particle in the inhomogeneous distribution, the PL quantum yield (Φ) is related to the radiative and nonradiative decay rates or times,

$$\Phi = \frac{k_{rad}}{k_{rad} + k_{nr}} = \frac{\tau_{nr}}{\tau_{nr} + \tau_{rad}} \qquad \text{equation. 2.6}$$

Thus, the QDs samples having higher quantum yields have smaller nonradiative rates and the ensemble gives the PL decay kinetics more close to a single exponential decay. As the quantum yield approaches unity, the time constant of this exponential gives the radiative lifetime. In chapter 2 and the dissertation, we will assume that a subset of the particles has a zero nonradiative rate. It follows that these particles give rise to the longest decay component and that this component corresponds the radiative lifetime. Evaluating this decay time from an experimental PL decay can be done in several different ways. In chapter 2, we will take it to be the longest component obtained by fitting the decay to a triexponential. In cases where the longest component dominates the decay, its time constant can be accurately and uniquely determined. However, the central assumption that this corresponds to the radiative lifetime may not always hold and needs to be carefully considered. Two particular situations are described here. First, if all the QDs in the ensemble have significant nonradiative decay rates, then the longest component of the measured PL decay will be a lower limit on the radiative lifetime. This may be expected when the density of surface or interfacial defects is high and the ensemble quantum yield is low. Second, very slowly decaying delayed luminescence can occur following reversible population of low-lying surface or defect trap states. If population of these traps is reversible, then the trap states serve as a reservoir of excited states and can result in PL decay components that are longer than the nominal radiative lifetime. Because of both complexities, this assumption will have to be examined in the analysis of each of the experimental results.

Differing from the low-QY single component CdSe or CdTe QDs, core/shell QDs often exhibit much higher QYs and are much more stable than their bare-core analogs. The reason is that coating with a shell material can effectively isolate the electron and/or hole wavefunctions from the surface, which contains dangling bonds and defects. These surface defects act as electron-hole recombination centers, causing nonradiative decay of photogenerated excitons. This results in exciton lifetimes that are less than the radiative lifetime, and photoluminescence (PL) QYs that are less than unity. Increasing shell thickness reduces the electron and/or hole densities at the particle surface and thereby reduces the effect of surface defects on the QYs as well as enhances photostability and chemical resistance. One typical core/shell QDs is the heterostructures with Type-I band alignment, in

which both electron and hole are confined in the core materials, such as CdSe/ZnSe. The large and small band offset in the conduction and valence band will confine the electron more in the core materials than the hole, thus, the hole still have a little tunneling in to the shell materials and are close to the surface or defect states , which usually limits the enhancement of QY.

Type-II nanocrystals consist of two different materials in which the band offsets are such that the lowest exciton has the electron spatially separated from the hole. The most extensively studied type-II system is CdTe/CdSe core/shell particles. In this case the hole is localized in the CdTe core and the electron in the CdSe shell. This results in greatly reduced electron-hole overlap and hence very long radiative lifetimes of the lowest exciton. The extent of electron-hole overlap depends on the core size and shell thickness. In the case of CdTe/CdSe there is a significant lattice mismatch, causing core compression.[7] Lattice strain can dramatically affect the band offset and hence the electron-hole overlap. The extent of electron-hole overlap in these core/shell particles can be understood in terms of electron and hole wavefunctions, calculated from an effective mass model.[7] In addition to all of the difficulties in comparing measured and calculated radiative lifetimes in single component QDs, type-II particles also have electron-hole overlap and lattice mismatch considerations.

The conduction and valence band offsets are such that CdSe/CdS is a "type-1½" or "quasi-type-II" core/shell QD. CdSe and CdS have nearly the same conduction band energies, so the electron is delocalized throughout the QD. The valence band has a considerable offset, localizing the hole in the CdSe core. Photoexcitation produces holes that are well isolated from surface trapping processes, and this result in highly photostable particles having high QYs. Recently Nan et al reported a low temperature synthesis of very high quality zincblende CdSe/CdS core/shell QDs.[8] The PL QYs of these QDs are very high and remains high for relatively thick shells. Part of the reason of obtaining high quantum yield is due to small lattice mismatch between CdSe and CdS (4%).

In this chapter, we consider four closely related aspects of the size dependent spectroscopies of II-VI QDs. First, we consider existing literature on CdSe QD absorption spectra and extinction coefficients. From these results and fine structure considerations we calculate Boltzmann weighted radiative lifetimes. These lifetimes are compared to values we have measured on very high quality CdSe and CdSe/ZnSe core/shell nanocrystals. Second, analogous literature data are analyzed for CdTe nanocrystals and compared to lifetimes measured for very high quality QDs. Furthermore, studies of the absorption and excitation spectra and measured radiative lifetimes for CdTe/CdSe core/shell QDs are reported. These results are also analyzed in terms of a Boltzmann population of exciton sublevels and calculated electron and hole wave functions. Much of the absorption data and fine structure calculations are already in the literature. These results are combined with new measurements of radiative lifetimes and electron-hole overlap calculations to produce an integrated picture of the II-VI QD spectroscopic fundamentals. Finally, radiative lifetimes of a series of zincblende CdSe/CdS core/shell particles having different shell thicknesses. These values are obtained directly from time-resolved measurements and compared to values obtained from static spectra and the evaluation of equation 2.1. Agreement between values obtained from these completely different approaches is checked.

2.2 Experimental Section

Optical measurements.

In the time resolved photoluminescence studies, samples were excited with very low intensity 410 nm pulses at 1 MHz from a cavity-dumped frequency-doubled Coherent MIRA laser. The luminescence was imaged through a ¼ m monochromator with a 150 groove/mm grating onto a Micro Photon Devices PDM 50CT SPAD detector. TCPC decays are accumulated using a Becker-Hickle SPC-630 board. The overall temporal response function of the system is about 400 ps.

Quantum yield measurements were made using the same samples as the time resolved luminescence measurements. The static luminescence spectra were measured on a Jobin-Yvon Fluorolog 3 with a CCD detector. Sample spectra were compared with spectra of R6G (assumed to have a 95% QY) taken with the same excitation wavelength and the same absorbance at that wavelength. The wavelength dependence of the CCD detector was taken into account in calculating the nanoparticle quantum yield. This was done by measuring the spectrum of a calibrated tungsten lamp and constructing a detector sensitivity curve. The excitation wavelength is 510 nm.

Photoluminescence excitation (PLE) measurements were obtained from the intensities of PL maxima with respective excitation at various wavelengths, corrected by the intensities of lamp efficiencies at corresponding wavelength. The PLE spectra were normalized with lowest energy exciton intensity and compared to raw absorption spectra directly.

Chemicals.

Cadmium oxide (CdO, 99.5%), trioctylphosphine oxide (TOPO, 90%), octadecylamine (ODA, 90%), tellurium (Te, 99.8%), oleylamine (technical grade, 70%), octylamine (99%), sodium diethyldithiocarbamate trihydrate ($NaDDTC{\cdot}3H_2O$),cadmium acetate dihydrate ($Cd(Ac)_2{\cdot}2H_2O$),trioctylphosphine (TOP, 97%), tributylphosphine (TBP, 97%), octadecene (ODE, 90%), hexane (99.8%), methanol (MeOH, 98%), and toluene (99%) were obtained from Aldrich. Zinc oxide (ZnO, 99.9%), selenium (Se, 99%), oleic acid (OA, 90%), n-octane (98+%) and chloroform ($CHCl_3$, 99.8%) were obtained from Alfa Aesar. Octadecylphosphonic acid (ODPA, 99%) was obtained from PCI synthesis. ODPA and ODA were recrystallized from toluene before use. TOP, TBP, and ODE were purified by vacuum distillation. TOPO was purified by repeated recrystallization from acetonitrile. Methanol, toluene, and chloroform were purified by distillation from appropriate drying agents. All other chemicals were used as received.

Standard wurtzite CdSe particle synthesis.

0.4 mmol of CdO was mixed with 1.6 mmol (0.45 g) of stearic acid and 4g (5.0 ml) octadecene (ODE) which was heated to 250°C to get a colorless solution under N_2 flow. After cooling to room temperature, 3g of octadecyl amine (ODA) and 1g of trioctylphosphine oxide (TOPO) were added. The mixture was then heated to 280 °C. At this temperature, a selenium solution containing 4 mmol of Se, 0.944 g (4.7 mmol, 1.15 ml) of tributylphosphine (TBP) and 2.74 g (3.4 ml) ODE was quickly injected under N_2. The reaction is run at 255 °C. When CdSe nanoparticles reached to the desired size, the reaction mixture was cooled to room temperature. When the reaction mixture reached 100 °C, 5mL of toluene was added to prevent solidification. This synthesis results in monodisperse, highly luminescent particles with quantum yields of about 20%.

Larger size wurtzite CdSe particle synthesis (> 3.5 nm diameter).

0.2 mmol of CdO was mixed with 1.2 mmol (0.34 g) of oleic acid and 4.8g (6.0 ml) ODE which was heated to 250°C to get a colorless solution under N_2 flow. After cooling to room temperature, 1.0 g of ODA and 0.5 g of TOPO were added. The mixture was then heated to 280 °C. At this temperature, a selenium solution containing 1.0 mmol of Se, 0.30 g (1.5 mmol, 0.37ml) of TBP and 1.0 ml of ODE was quickly injected under N_2. The reaction is run at 255 °C for 1 – 2 min. When CdSe nanoparticles reached to the desired size, the reaction mixture was cooled to room temperature. This synthesis results in monodisperse, highly luminescent particles with quantum yields of about 40 - 50%.

Smaller size wurtzite CdSe particle synthesis.

0.4 mmol of CdO was mixed with 2.4 mmol (0.68 g) of stearic acid and 4.0 g (5.0 ml) ODE which was heated to 250°C to get a colorless solution under N_2 flow. After cooling to room temperature, 2.0 g of ODA and 0.7 g of TOPO were added. The mixture was then heated to 285 °C. At this temperature, a selenium solution containing 3.0 mmol of Se, 0.90 g (2.4 mmol, 1.1 ml) of trioctylphosphine (TOP) and 1.0 ml of ODE was quickly injected under N_2. The reaction is run at 255 °C for about 1 min. When CdSe nanoparticles reached to the desired size, the reaction mixture was cooled to room temperature. This synthesis results in monodisperse, highly luminescent particles with quantum yields of about 40 - 50%. The ideas underlying these optimizations are based on the relative rates of nucleation and growth, and are quite straightforward. Larger particles are obtained when nucleation occurs relatively slowly and ceases very early on in the synthesis. These conditions result in relatively few nuclei, and therefore growth of larger particles. The low concentrations used in the large particle synthesis facilitate this type of growth. Conversely, the conditions used for the small particle synthesis result in very rapid nucleation and a high concentration of nuclei. In both cases, the reaction is terminated while still in the strongly focusing regime. We find that this also gives the highest quantum yields, in accord with previous literature reports.[9]

Wurtzite CdSe/ZnSe core/shell particles synthesis.

This synthesis is similar to those described in the literature, which also provide extensive particle characterization.[10] The 0.1 M Se stock solution for ZnSe shell growth is made with 2 mmol (157.9 mg) Se, 0.48 ml (2.3 mmol) TBP and 19.5 ml ODE. The 0.1 M Zn stock solution is made with 2 mmol (162.74 mg) ZnO, OA: 8 mmol (2.52 ml), 17.5 ml ODE. CdSe particles with various sizes are synthesized based on the standard method. The reaction is quenched by cooling to room temperature. The final reaction solution is extracted by hexane: methanol (1:1 v/v) two times. The organic layer is separated and heated to 75 °C to remove the residual hexane and methanol.

In a typical ZnSe shell growth reaction, a mixture of ODE (2.0 mL), ODA (10 mg), and oleylamine (1.0 mL) was heated to 60 °C in a three-neck flask under argon flow, and then about 1.0 mL of purified CdSe core solution (containing about 1×10^{-7}mol of nanocrystals estimated by their extinction coefficients) was added to this flask. The amount of precursor solution for each injection was estimated using standard successive ionic layer adsorption and reaction (SILAR) procedure. The Zn and Se precursors were added dropwise into the reaction mixture at 230 °C respectively to grow 2 or 3 monolayers of ZnSe.

Zincblende CdTe particles and CdTe/CdSe core/shell particles.

The Te precursor solution is made by dissolving 0.1mmol (12.8 mg)Te in the mixture of 0.15 ml TOP, 0.15 mmol (50.17 mg) ODPA and 1 ml ODE. [10] The 0.1 M Se stock solution for ZnSe shell growth is made with 2 mmol (157.9 mg) Se, 0.48 ml (2.3 mmol) TBP and 19.5 ml ODE.

In a typical reaction, 0.2 mmol (25.7 mg) of CdO was mixed with 0.8 mmol (0.25 g) of oleic acid and 3.0 ml ODE and heated to 250°C to get a colorless solution under N_2 flow. Then the tellurium precursor (at ~100 °C) is loaded in a 3 ml syringe and quickly injected at 280 °C. The temperature is kept at 260°C for 2~3 min for the growth of the CdTe particles. Larger particles are obtained by increasing the volume of the cadmium precursor by dilution with ODE. After the core growth, the solution is cooled to230°C, and 2 ml Se precursor is added drop-wise for the growth of the CdSe layers. The reaction is quenched by cooling to room temperature. The CdTe and CdTe/CdS raw reaction solution is extracted by hexane:chloroform:methanol (1:1:1 v/v) twice. The polar layer is removed and the remaining particles are heated to 75 °C to remove the residual hexane, chloroform and methanol.

Zincblende (ZB) CdSe/CdS core/shell particles.

The zincblende CdSe core nanocrystals are synthesized and purified using the slightly modified procedures reported by Nan et al.[8] Zincblende shell deposition occurs from a cadmium-sulfur single precursor, cadmium diethyldithiocarbamate ($Cd(DDTC)_2$), at low temperature (140 - 145 °C).

In a typical synthesis, CdO (0.256 g, 0.2 mmol), oleic acid (1 mL) and 4 mL ODE were loaded into a 25 mL three-neck flask. After N_2 bubbling for 2 min, the flask was heated to 250 °C to form a transparent solution and then cooled to 40 °C. Se powder (0.0079 g, 0.1 mmol) was loaded into the flask. The flask was heated to 240 °C under N_2 flow at a heating rate of 40 °C/min. Needle tip aliquots were taken for UV−vis and PL measurements to monitor the size of zincblende CdSe QDs. The particles are then purified by repeated extraction. In these extractions, tributylphosphine (0.2 mL), octylamine (0.2 mL), hexane (3 mL), and methanol (6 mL) were added to the reaction solution at 50 °C and stirred for 2 min. After stirring was turned off, the colorless methanol layer was separated from the top ODE/hexane layer by syringe. This extraction procedure was repeated three times, but TBP was only added for the first time. The hexane left in the ODE layer was removed by argon bubbling at about 60 °C.

Subsequent CdS shell growth requires the synthesis of ($Cd(DDTC)_2$) for use as the single cadmium and sulfur precursor. In this synthesis, $Cd(Ac)_2{\cdot}2H_2O$ (10 mmol) was dissolved with 100 mL of distilled water in a 400 mL beaker. Into this solution, $NaDDTC{\cdot}3H_2O$ (20 mmol) dissolved in 60 mL of distilled water was added dropwise under vigorous stirring. A white precipitate of $Cd(DDTC)_2$ quickly forms. The mixture was stirred for another 20 min after mixing to ensure the reaction was complete. The white precipitate was separated from the solution phase by filtration and washed three times with distilled water. The final product in white powder form was obtained by drying under vacuum overnight. For each shell growth reaction, a 3 mL $Cd(DDTC)_2$-amine-octane solution (0.1 mmol/mL) was prepared by dissolving 0.1227 g of $Cd(DDTC)_2$ in a mixture of octane (1.5 mL), oleylamine (0.45 mL), and octylamine (1.05 mL).

In a typical CdS shell growth reaction, a mixture of ODE (2.0 mL), ODA (20 mg), and oleylamine (1.0 mL) was heated to 60 °C in a three-neck flask under argon flow, and then about 1.0 mL of purified CdSe core solution (containing about 1×10^{-7}mol of nanocrystals estimated by their extinction coefficients) was added to this flask. The amount of precursor solution for each injection was estimated using standard SILAR procedure. In this reaction cycle, addition of the precursor solution is done at 80 °C and growth occurs by heating the solution at a targeted temperature (140 °C for typical synthesis) for about 10 min, was continued until the desired number of CdS monolayers are obtained. The final reaction solution is purified, ligand exchanged with TBP/ODA, then dispersed in toluene or chloroform for the spectroscopic measurements.

Ligand exchange of purified particles.

The extracted sample is dissolved in 2 ml of ODE and added to a vial containing 1.0 g ODA (or 1.0 g ODA + 0.5 ml TBP, or 0.5 ml TBP, or 1 ml ODE), under nitrogen. The vial is heated to about 65 °C, and stirred continually for 12 hours, then cooled to room temperature. The ligand exchanged particles are extracted by chloroform: methanol (1:1 v/v) two times. In the case of ODA and ODA/TBP, the particles are precipitated and centrifuged. In the case of TBP and ODE, a phase separation occurs and the nonpolar phase is kept. The solid particles or ODE solution are dried under vacuum and kept under N_2.

2.3 Results and Discussion

2.3.1 CdSe nanocrystal spectroscopy

The original measurements of CdSe band edge integrated extinction coefficients were published more than a decade ago and show that these values increase linearly with particle radius.[11] Shortly thereafter, measurements of the band edge energies and lowest exciton extinction coefficients covering a wide range of CdSe and CdTe nanocrystals sizes showed that the extinction coefficient increases supra-linearly with increasing particle radius.[12] The spectral width of the lowest exciton peak can also vary with particle size, making it difficult to compare these sets of measurements. More recently, very accurate measurements of the size-dependent extinction coefficients for wurtzite CdSe QDs have been made by Jasieniak et al,[13] and for zincblende QDs by Capek et al.[14] These measurements show the same trend of increasing extinction coefficients with particle size, and are in good agreement for particles having diameters of about 5 nm. However, the older results[12] show significantly smaller extinction coefficients for the smaller particles. The increase of the extinction coefficient with particle size is a large effect. For example, comparing 3.0 and 6.0 nm CdSe particles, the extinction coefficient of a 6 nm nanocrystal is a factor of 3.5 larger.[13] This strongly increasing extinction coefficient indicates that the oscillator strength also increases with particle size, and to the extent that dark versus bright states population effects remain constant (to be discussed below), the radiative lifetime should decrease with increasing particle size. The ν^2 dependence in equation 2.1 goes the other way: larger particles emit further to the red and the ν^2 factor causes the radiative lifetime to increase with particle size. However, over this wavelength range the ν^2 dependence is a relatively small effect and only partially offsets the trend predicted from the increasing extinction coefficient. The measured extinction coefficients are quite large. For example reference 13 gives an extinction

coefficient of 2.7 x 10^5 L mol^{-1} cm^{-1} for 4.0 nm CdSe particles. The corresponding calculated oscillator strength is also quite large, about 1.6 (excluding the local field factor). In comparison, fully allowed transitions in organic dye molecules typically have oscillator strengths of about unity. In above cases, no attempt to connect these measurements to radiative lifetimes was made.

de Mello Donega and Koole have measured luminescence decays and fit the kinetic curves to a single exponential.[15] They suggest that the single exponential decay time reflects the radiative lifetime and find that these lifetimes increase with increasing particle size. The band gap decreases with increasing particle size and they find that there is a linear increase of the radiative rate (τ_{rad}^{-1}) with increasing band gap energy. It is argued that the decays are close to single exponentials, so that role of nonradiative processes affecting these rates does not need to be considered. The theoretical treatment in ref15 ignores the angular momentum fine structure, and argues that this is valid because some of the states are dark, and therefore don't contribute to the observed luminescence. However, this argument is not valid if the population equilibrates between the bright and dark sublevels, which it is known to do on a time scalethat is short compared to luminescence.[16] The dark levels do not undergo radiative decay and therefore serve as a reservoir of the exciton population, resulting in an increased effective radiative lifetime. Reference 15also reports that the results are in quantitative agreement with results reported by van Driel et al.[17] It is important to note that an increase in radiative lifetime with particle size is the opposite trend from what is expected, based on the reported size dependence of the extinction coefficients.[13] Larger particles have larger extinction coefficients, and based solely on this consideration, would be expected to have shorter radiative lifetimes. In a later paper, the strong size dependence of the radiative lifetime is corrected by Leistikow et al,[18] reporting that the radiative lifetimes are in the 15 – 20 ns range and almost size independent. This time scale is consistent with results reported by Crooker et al,[19] where the lifetime was determined from long-time tail of the PL decay. Although the lack of a strong size dependence is closer to being consistent with the trend expected from the size dependent extinction coefficients, the lifetimes reported by considerably shorter than the previously reported values.[15, 17]

To resolve these discrepancies, we have measured size-dependent absorption spectra and PL kinetics of CdSe and CdSe/ZnSe QDs. Two types of CdSe syntheses were done. First, we did a "standard" synthesis, producing particles with diameters ranging from 2.5 to 4.5 nm, depending upon reaction time. This synthesis has been previously described with detailed list in the Experimental Section, [20] and is based on the high temperature reaction of cadmium stearate with excess tributylphosphine selenium in a mixture of octadecene, octadecylamine and trioctylphosphine oxide. Slight variations of this method are very commonly used to produce CdSe particles over a wide range of sizes. This synthesis produces reasonably monodisperse, high quality particles having PL quantum yields of about 20%. Different particle sizes are obtained by pulling aliquots of the reaction mixture as the reaction proceeds. Absorption spectra of several different sized particles are shown in figure 2.1.We have also performed syntheses which are optimized to produce either smaller (< 3.5 nm) or larger (> 3.5 nm) particles, as shown in figure 2.2. The narrow spectral width of the exciton peaks indicates that these particles are very monodisperse. They also have considerably higher PL quantum yields, typically 40 – 50%. By varying the reaction time, smaller or larger particle sizes can be obtained which maintain these optical properties. A detailed comparison of the standard, larger and smaller particle syntheses is given in the

Experimental Section.

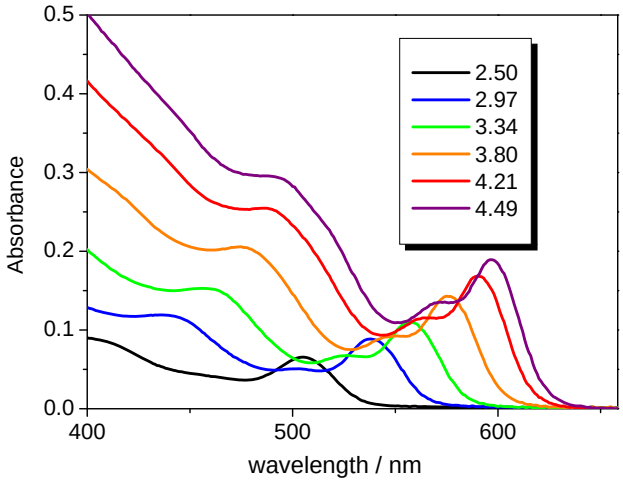

Figure2.1.Absorption spectra of several diameters of CdSe nanocrystals, as indicated.

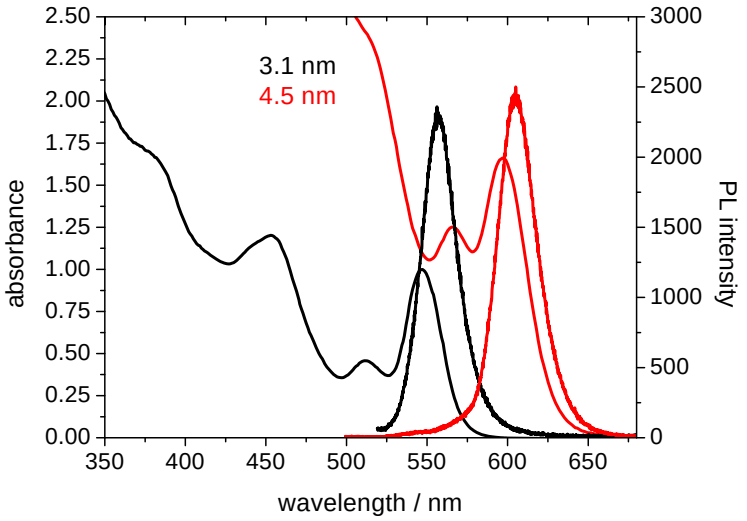

Figure 2.2. Absorption and PL spectra of smaller (3.10 nm) and larger (4.5 nm) CdSe particles from optimized syntheses, as indicated. The absorption spectra have been scaled so the absorption ratio at 355 nm matches the particle volume ratio.

The PL decays of particles from standard and optimized syntheses have been obtained and fit to triexponentials. This is done at low concentration and at very low fluence, to eliminate the possibility of concentration or fluence dependent artifacts. The signal to noise ratio of the experimental decays is quite high, and the long components can be determined quire accurately, to within a few nanoseconds. Plots of the long component decay times as a

function of particle size as shown in figure 2.3. These measured values can be compared to radiative lifetimes calculated from the absorption spectra. The absorption spectra in figures 2.1 have been scaled such that the 355 nm absorbance is proportional to the particle volume. Absorption cross sections far to the blue of the absorption onset are known to scale with particle volume,[11, 14] and with this scaling, the relative absorbances of the lowest excitons closely match the relative extinction coefficients given in reference 13 for all but the smallest particles. The extinction coefficients of the smallest particles are between the values given in references 12 and 13, but much closer to reference 13. Integrated extinction coefficients can be obtained from these absorption spectra by fitting each spectrum to several Gaussians and evaluating the area of the one corresponding to the lowest energy exciton. An example of this fitting is shown in figure SI-1 of appendix. We find that the size dependence of the integrated extinction coefficients increases approximately linearly with particle radius, in agreement with previously reported integrated extinction coefficients.[11] Similar results are obtained with the optimized particles.

Figure 2.3 shows that the longest decay components of the optimized particles are in good agreement with the radiative lifetimes calculated for spherical wurtzite particles. The calculation of the radiative lifetime curve is discussed below. Figure 2.3 shows that these measured times are significantly longer than those obtained from the standard synthesis particles. We suggest that this difference arises because all of the standard synthesis particles having finite nonradiative decay pathways, i.e., essentially all of the particles in any ensemble have a nonradiative decay component. This difference is not surprising; the standard synthesis particles have much lower PL quantum yields, indicating that the defects resulting in nonradiative decay are less effectively passivated. Since the radiative and nonradiative rates are additive, the long component of the measured PL decay curve actually gives a lower limit to the radiative decay time.

This conclusion is supported by results obtained from CdSe/ZnSe core/shell particles. The CdSe/ZnSe particles are better passivated than the CdSe particles, and the purpose of comparing the PL kinetics in the core and core/shell particles is to assess the role of nonradiative recombination in the PL decay kinetics. Absorption and PL spectra and a typical PL decay curve for CdSe/ZnSe particles having a 3.0 nm core and 0.6 nm thick shells are shown in figure 2.4.

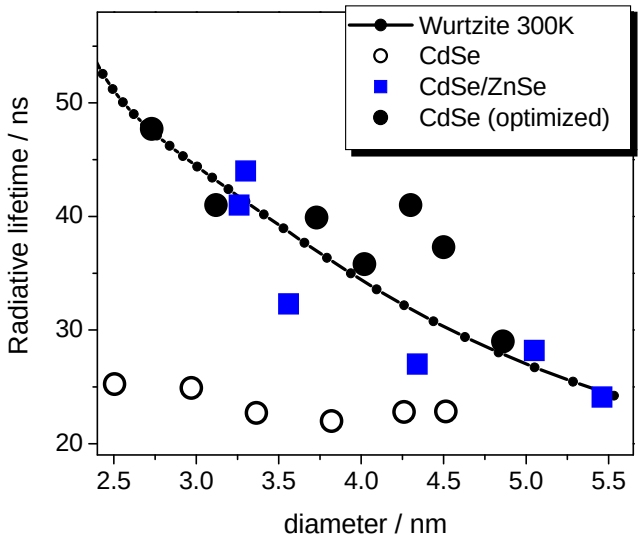

Figure 2.3. Experimental long decay components and radiative lifetimes calculated from integrated extinction coefficients. Experimental values are shown for standard and optimized CdSe particles and CdSe/ZnSe particles, as indicated. (The diameter of the core/shell particles is "effective" particle size, as discussed in the text.) The radiative lifetime curve is calculated on the basis of a 300 K distribution in the $1S_{3/2}$ hole fine structure and $1P_{3/2}$ hole levels of spherical wurtzite particles (black dotted curve).

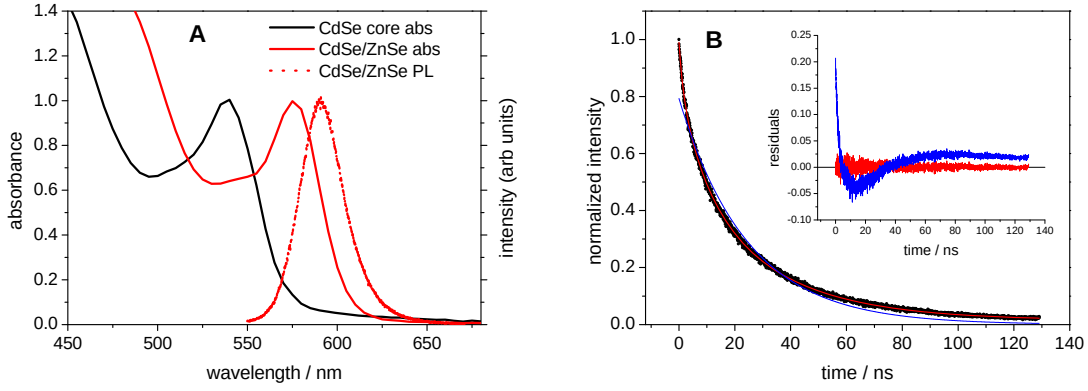

Figure2.4. (A) Absorption spectra of CdSe core (3.0 nm) and CdSe/ZnSe core/shell (3.0 nm core with a 0.6 nm shell) particles. The PL spectrum of the CdSe/ZnSe particles is also shown. (B) PL decay kinetics for a CdSe/ZnSe core/shell particles (black curve). Also shown are a fitted curve corresponding to 1.6 (15%), 9.4 (33%) and 32 ns (52%) components (red curve), and a single exponential decay corresponding to 20 ns (blue curve). The residuals from these fits are shown in the inset.

Comparison with the size dependent CdSe and CdSe/ZnSe lifetimes is complicated by the red shift of the absorption and PL spectra upon shell deposition. The red shift occurs because the electron and hole wave functions penetrate into the (energetically forbidden) ZnSe shell, slightly expanding the exciton volume. The "effective size" of these particles is therefore larger than that of the starting core. For the core/shell particles, we define the effective diameter as that of corresponding CdSe particles having the same lowest exciton energy. With this definition, deposition of the 0.6 nm thick shell used here increases the effective diameter of the smallest particles by about 0.5 nm. This effective diameter is used in plotting the measured CdSe/ZnSe radiative lifetimes in figure 2.3. Plotting the data in this fashion facilitates comparison with the CdSe experimental results and calculations. It correctly incorporates the ν^2 factor in equation 2.1, and the calculated fine structure splittings (discussed below). Comparison of size-dependent results calculated for CdSe core particles with the CdSe/ZnSe experimental results for particles having the same effective size tacitly assumes that the two types of particles have the same exciton extinction coefficients. That is, it assumes that to the extent that the exciton wavefunction is delocalized into the shell, that part of the wavefunction also contributes to the exciton oscillator strength. If the part of the wavefunction localized ZnSe contributes less or more on a per volume basis than that in CdSe, then the calculated radiative lifetime would be increased or decreased, respectively. We are unaware of any literature data on integrated extinction coefficients of the lowest excitons in type-I particles. We make the CdSe versus CdSe/ZnSe comparison on the basis of the core/shell effective sizes, noting the above caveat. Although there is some scatter in the experimentally measured radiative rates, figure 2.3 shows that the CdSe/ZnSe values are in agreement with the results of the optimized CdSe particles and the spherical wurtzite particle 300 K calculations.

Calculation of the radiative lifetimes from the integrated extinction coefficients must take into account the Boltzmann populations and relative oscillator strengths of the thermally accessible states. When there is a thermal equilibrium between more than a single absorbing and emitting state, equation 2.1 becomes[3]

$$A = 2.88x10^{-9} C_{fs} n^2 \tilde{\nu}^2 \int \varepsilon(\tilde{\nu}) d\tilde{\nu}\ ,\ C_{fs} = \frac{\sum_i f_i \exp(-E_i / k_B T)}{\sum_i \exp(-E_i / k_B T)} \qquad \text{equation. 2.7}$$

There are eight thermally accessible angular momentum sublevels in the $1S_e$-$1S_{3/2}$ exciton and considering only these states in the high temperature limit, we have that C_{fs} = 1/8. The energies and oscillator strengths of these sublevels vary with nanocrystal size.[4] In spherical particles, the lowest energy state is the doubly degenerate, optically dark J = ±2 level. The optically bright levels are a few to a few tens of meV higher in energy, with this splitting getting larger in smaller particles. This is comparable or somewhat smaller than k_BT (= 26 meV at 300 K), and the thermally equilibrated levels have significant, but not equal populations. We note that the energies and oscillator strengths of these levels also depend on the nanocrystal shape.[4] In even slightly prolate particles (aspect ratio of 1.15) the ordering of these levelsis changed, with the lowest energy level being the singly degenerate, optically dark 0^L level and the doubly degenerate bright $\pm1^L$ level at slightly higher energies. The result is that the calculated values of C_{fs} depend on the assumed particle shape. Accurate evaluation of C_{fs} also requires that thermal population of the four-fold degenerate $1P_{3/2}$ hole level also be considered (the $1S_e$-$1P_{3/2}$ exciton is therefore also eight-fold degenerate). The energy difference between the $1S_e$-$1S_{3/2}$ and $1S_e$-$1P_{3/2}$ excitons can be calculated as described

by Efros and Rosen,[6] and increases approximately linearly with the inverse of the particle diameter. These energy splittings are somewhat larger than the splittings between the different angular momentum sublevels, and vary from 57 to 21 meV over the range of 2.5 to 5.5 nm particles. These energies are also comparable with k_BT and including thermal population of these dark levels further decreases the calculated radiative rates. Realistic calculations involve 300 K Boltzmann populations in all of the $1S_{3/2}$ and $1P_{3/2}$ hole sublevels. As a simplest approximation, we consider the fine structure energy splitting of the $1S_e$-$1P_{3/2}$ exciton to be the same as in the $1S_e$-$1S_{3/2}$ exciton. Since all of the $1S_e$-$1P_{3/2}$ sublevels are dark, the calculation is insensitive to the exact energetics of these sublevels; this only affects the electronic partition function. Inclusion of the $1S_e$-$1P_{3/2}$ exciton is a significant effect and increases the electronic partition function on the order of 30%. Using the integrated extinction coefficients in reference 13, radiative lifetimes have been calculated for spherical particles having a wurtzite crystal structure at 300 K, and are plotted in figure 2.2. Prolate particles are calculated to have slightly shorter radiative lifetimes (a few nanoseconds), with the difference increasing with decreasing particle size.

Several trends are apparent in the experimental and calculated results. The experimental results from the optimized CdSe synthesis give longest decay components that are approximately 45 ns for the smallest particles and decrease with particle size to about 25 ns for the largest particles. These results are at odds with most of what is in the literature and opposite to the trend reported in references 15 and 17. The present results come closer to agreeing with the trend reported in reference 18, that are close to size independent, but reports considerably shorter times, about 15 – 20 ns. Part of the discrepancies may come from fitting procedures. Figure 2.4B shows that fitting the PL decay to a single exponential can result in an apparent lifetime that affected by nonradiative processes and therefore too small. However, we suggest that the comparison of the results from the standard and optimized syntheses directly bears on the main source of the literature discrepancies. The lifetimes obtained from the CdSe particles using the optimized synthesis and the core/shell particles are in agreement with the calculated values, while the CdSe particles obtained from the standard synthesis give shorter values. This comparison reveals that the main difference between these results and those in previous literature reports is simply particle quality – the presence or absence of surface defects that result in nonradiative decay. Only the particles from the optimized synthesis and the core/shell particles have minimal nonradiative decays and therefore yield accurate radiative lifetimes.

2.3.2 CdTe NANOCRYSTAL SPECTROSCOPY

The size dependence of the CdTe exciton energy has been reported by Yu et al,[12] and more recently by de Mello Donega and Koole[15] and by Kamal et al.[21] The results in references 15 and 21 are in excellent agreement with each other and the results in reference 12are only slightly different. The size dependent exciton extinction coefficients of CdTe nanocrystals have also been originally analyzed in reference 12 and more recently in reference 21 and by Groeneveldet.al.[22] These later studies report larger extinction coefficients than reference 12 for all particle sizes, but especially for the smaller particles. The small particle extinction coefficients reported in reference 22 are only slightly smaller than those in reference 21. From the integrated extinction coefficients, size-dependent oscillator strengths and radiative lifetimes can be calculated. As in the case of CdSe

particles, the corresponding total absorption oscillator strengths in the $1S_e$-$1S_{3/2}$ transition is very large, for example, we calculate f = 1.75 for a 5.0 nm particle (ignoring local field effects). Reference 21 reports considerably larger oscillator strengths, presumably because of the inclusion of local field effects. Reference 21 reports that the calculated radiative lifetimes are in the 10 – 13 ns range, increasing slightly with increasing particle size. This calculation assumes that the 1Se-$1S_{3/2}$ fine structure levels are equally populated; it applies a high temperature approximation. The 10 – 13 ns calculation ignores the $1P_{3/2}$ levels and concludes that calculated radiative are a factor of two larger if these levels are also included in the high temperature approximation. Measured radiative lifetimes have been reported in reference 15and by van Driel et al,[17] which give values increasing with particle size from 17 to 27 ns and 18 to 29, respectively, over the range of approximately 2.5 to 6.0 nm particles. We have synthesized high quality CdTe (and CdTe/CdSe) particles using the previously reported methods[7] and find experimental radiative lifetimes that are somewhat longer, but follow the same trend, varying from about 24 to 35 ns over the same range of particle sizes, as shown in figure 2.5.

The discrepancy between our measured radiative rates and those reported in references 15 and 17 may be due to differences in how the PL decays are analyzed. In the previous studies, the decay curves were fit to single or stretched exponentials, which ignores the inhomogeneous distribution of nonradiative decay rates. We fit the decay curves to a triexponential, and assign the dominant (longest) component to the radiative lifetime. As discussed above, this is correct because it allows for the possibility that some fraction of the particles have defects that result in a finite nonradiative decay rate. As also discussed above, if all of the particles exhibit some nonradiative decay, then the radiative lifetimes derived from this procedure are a lower limit to the actual radiative values.

Experimental results can be compared to those calculated from the integrated extinction coefficients in references 12, 15 and 21. The spectra and fine structure of CdSe and CdTe QDs are very similar, and as in the case of CdSe QDs, this calculation requires inclusion of Boltzmann populations in these levels. In both cases, the lowest two transitions in the absorption spectrum ($1S_e$-$1S_{3/2}$ and $1S_e$-$2S_{3/2}$) are somewhat overlapping. Deconvolution of these absorption features facilitates getting accurate estimates of the actual integrated extinction coefficients. The energies and oscillator strengths of the different fine structure levels depends on the particle size and we have calculated Boltzmann populations and oscillator strengths of these levels as a function of particle size. In the case of the zincblende CdTe, we calculate that small changes in the particle aspect ratio make very little difference in the calculated radiative lifetimes, so we only consider the case of spherical particles. With the correction for spectral overlap and the inclusion of the Boltzmann population of the angular momentum fine structure levels, calculated radiative lifetimes using the integrated extinction coefficients in references 12, 15 and 21 are shown in figure2.5. The experimental results are bracketed by these calculations. Based on the experimental methods, we expect that the extinction coefficients reported in reference 21 are probably the most reliable. These values lead to a significant underestimate of the radiative rates, particularly for the smallest particles. Although we have no definitive assignment for this discrepancy, we speculate that the splitting of the fine structure levels is slightly more than the calculations in reference 4a indicate. The increased splitting could be caused by perturbations such as surface charges.

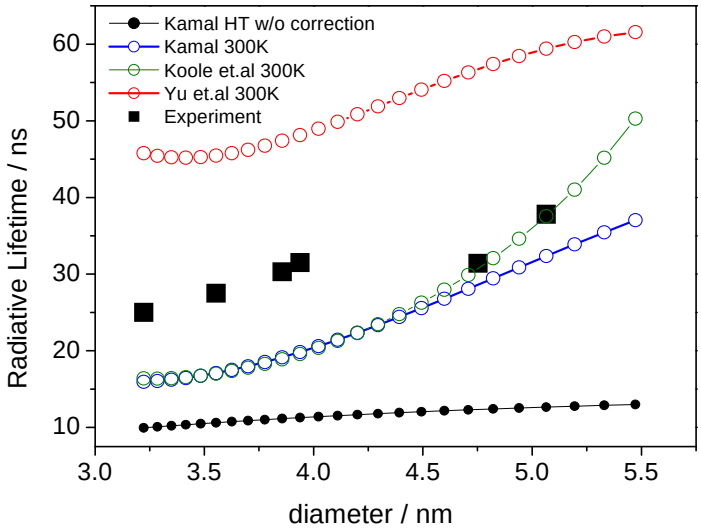

Figure 2.5. (Measured and calculated radiative lifetimes of different sizes of CdTe QDs. The calculated values correspond to using extinction coefficients from different literature sources and the fine structure levels populated equally (high temperature limit, HT), or populated at 300 K. The absorption intensities are corrected for the overlap of the lowest two exciton transitions.

2.3.3 CdTe/CdSe nanocrystal spectroscopy

CdTe has valence and conduction bands that are at higher energy (closer to the vacuum level) than CdSe. As such, CdTe/CdSe core/shell nanoparticles have type-II band offsets.[23] Following photoexcitation, the hole localizes in the core and the electron localizes in the shell. The small electron-hole overlap results in the lowest exciton having a small integrated extinction coefficient and a long radiative lifetime. CdTe-CdSe lattice mismatch causes strain that raises the CdTe conduction band energy, further decreasing the extent of electron-hole overlap.[7, 24] Thus, the lowest exciton shifts to the red and loses oscillator strength with increasing shell thickness. The extent of this decrease depends on the shell morphology, specifically, core/shell particles show greater electron-hole separation than core/tetrapods for a given exciton energy.[7] Similarly, Groeneveld et al[22] and de Mello Donega[25] report core/tetrapod particles with a decreasing amount of oscillator strength in the lowest transition as the tetrapod arms get longer. Absorption and luminescence spectra of 3.4 nm CdTe cores with 0 – 1.35 nm thick CdSe shells are shown in figure 2.6. In agreement with previously reported results, these spectra show that the $1S_{3/2}$-$1S_e$ transition shifts to the red and loses intensity with increasing shell thickness.[7, 22, 25-26]

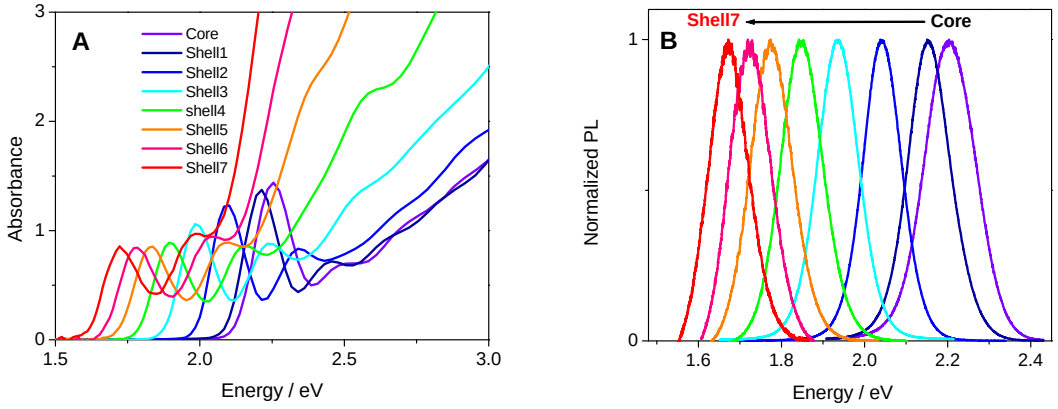

Figure 2.6. (A) UV-Vis spectra of CdTe/CdSe core-shell nanoparticles at constant concentration. (B) Corresponding luminescence spectra of the particles in panel A.

The absorption intensity at the higher energies has contributions from the core/shell particles and from homogeneously nucleated CdSe particles that are formed during shell growth. The contribution from the latter can be minimized by varying the synthetic procedures, but is extremely difficult to completely eliminate. Its relative contribution typically increases as shell growth proceeds. This can be seen in the comparison of the photons absorbed and excitation spectra, see figure 2.7. The CdSe particles do not give luminescence at the same wavelength as the core/shell particles, so excitation spectra with wavelength-selective detection gives only the contribution of the core/shell particles. Figure 2.7 shows that the CdTe core and the first core/shell particles have essentially identical photons absorbed and excitation spectra. The additional CdSe absorption appears at the third shell injection and its contribution to the blue absorbance progressively increases.

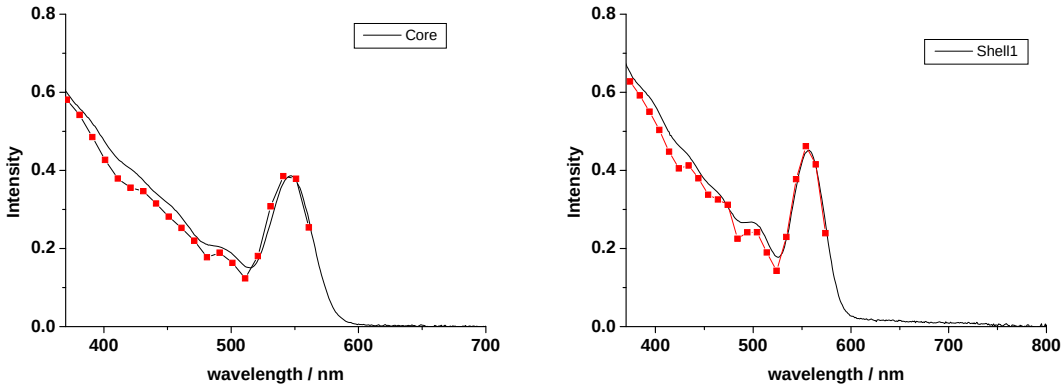

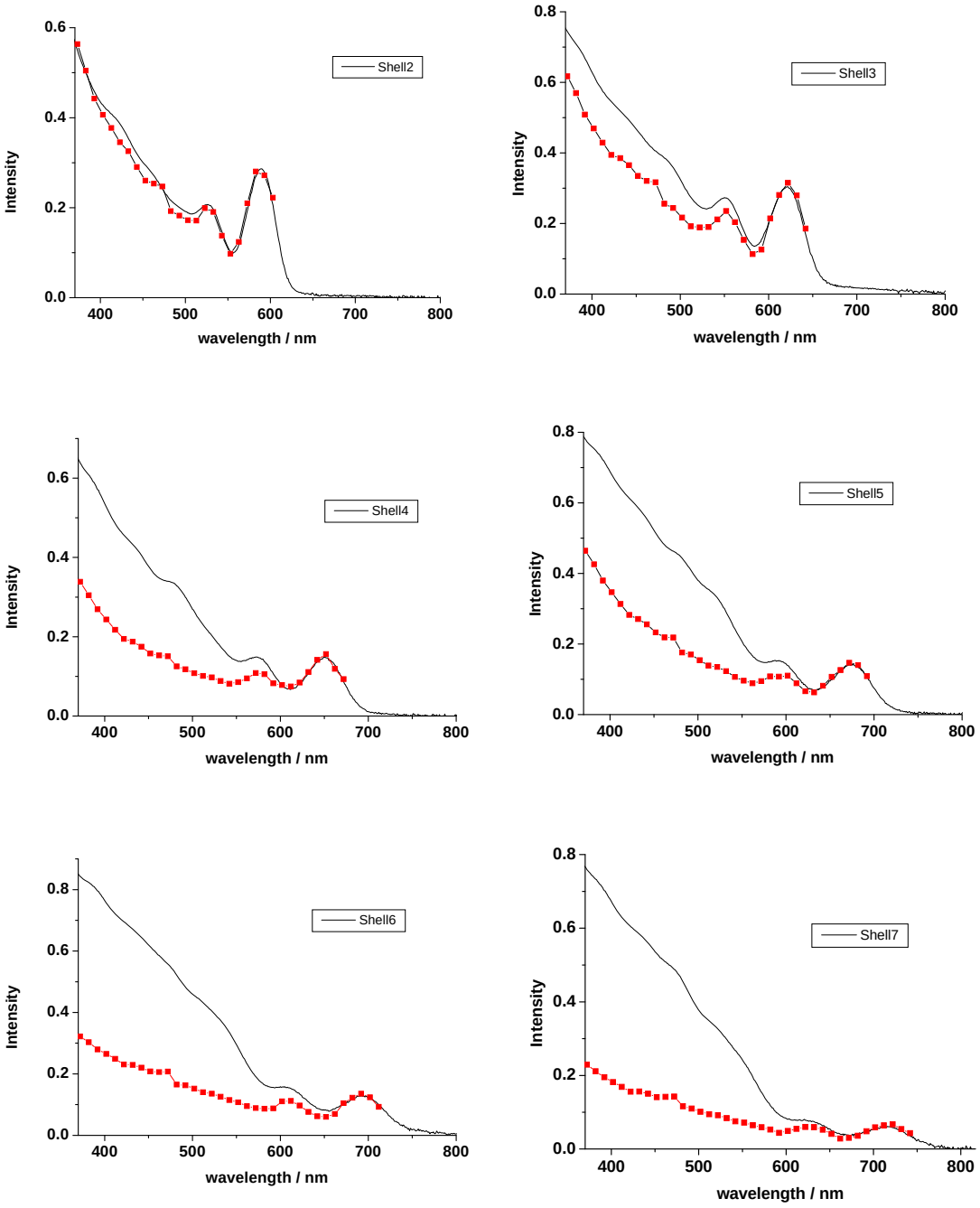

Figure 2.7. Comparison of photons absorbed ($1-10^{-absorbance}$) (black lines) and luminescence excitation (red points) spectra of CdTe core and CdTe/CdSe core/shell particles. Excitation spectra are normalized to the photons absorbed spectra at the lowest energy exciton transition.

The absorption and excitation spectra also show a partially resolved transition at an energy about 0.25 eV above the lowest $1S_e$-$1S_{3/2}$ transition, independent of shell thickness. The relative intensity of this peak increases with increasing shell thickness and it is assigned to the $1S_e$-$2S_{3/2}$ transition. The observation that the 0.25 eV energy difference between the lowest two transitions is essentially independent of shell thickness is crucial to this assignment. The $1S_e$-$1S_{3/2}$ and $1S_e$-$2S_{3/2}$ transitions correspond to two different hole levels and the same final electron level. Thus, in these type-II core/shell particles, the extent of hole quantum confinement is essentially constant with increasing shell thickness. This assignment is further confirmed from the relative intensities of these transitions. The relative intensities are easily deconvoluted from the experimental spectra and can be compared to calculated values of the wavefunction overlap, $\left|\langle 1S_e|1S_{3/2}\rangle\right|^2$ and $\left|\langle 1S_e|2S_{3/2}\rangle\right|^2$. These calculations are described in detail in reference7, and the comparison is shown in figure 2.8. As the shell gets thicker, the electron becomes more delocalized throughout the core and the shell, while the hole remains essentially localized in the core. Thus, the orthogonality of the electron and hole wavefunctions is lost as the particle becomes type-II, and there is considerable overlap between the electron wavefunction and both of the two lowest energy hole functions. The calculations reflect this aspect of the wavefunctions and we find that semiquantitative agreement over the entire range of shell thicknesses. We also note that the calculations quantitatively reproduce the observed relative intensities only for thicknesses over about 1.0 nm. This model includes the effects of a realistic amount of selenium-tellurium interdiffusion upon shell deposition, the effects of lattice strain and band-bowing in the alloyed interface. It assumes a perfectly uniform spherical continuum shell and uses bulk semiconductor parameters. However, the assumption of a uniform shell cannot be valid for very thin or sub-monolayer shell coverage and this may explain why better agreement is obtained for the thicker shells. We note that the $1S_e$-$2S_{3/2}$transition in CdTe/CdSe type-II particles has been previously observed and is often assigned to a "CdSe transition".[27] However, the above considerations establish the correct assignment.

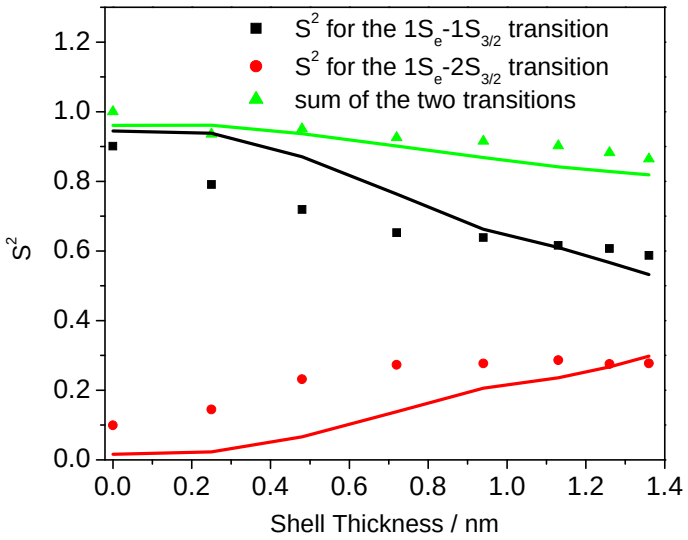

Figure 2.8. Comparison of calculated overlap integrals, S^2, (lines) with experimental values of energy-integrated absorption of first ($1S_e$-$1S_{3/2}$) and second ($1S_e$-$2S_{3/2}$) exciton transitions divided by their transition energy (equivalent of oscillator strength) as a function of shell thickness.

The CdTe and CdSe extinction coefficients at higher energies are typically taken to be proportional to the particle volume,[11, 13] and our results on CdSe and CdTe nanocrystals are also consistent with this. To the extent that the electron-hole pair formed by high energy excitation is highly localized and much smaller than the particle, this should be a good approximation. However, this may not be a good approximation in the case of a CdTe core having a very thin CdSe shell for excitation in the 375 - 450 nm region.[7] The reason for this can be understood in terms of the comparison of the valence and conduction band energetics to the photon energy. In the simplest approximation, the relative amounts of energy that photoexcitation puts in the electron and hole scale like the inverse of each particle's effective mass.[28] The CdTe electron and hole effective masses are 0.10 and 0.40 in units of the electron mass, respectively.[29] CdTe has a 1.5 eV bandgap and 3.3 eV (375 nm) excitation puts about 1.44 and 0.36 eV in the electron and hole, respectively. However, the CdSe valence band is at a potential 0.54 eV further positive than that of CdTe, which is greater than the 0.36 eV hole energy following 3.3 eV excitation. As a result, the hole is energetically excluded from the CdSe region of the particle. Further red excitation produces a hole that is less energetically able to be in the CdSe shell. We conclude that the initially produced hole is largely confined to the CdTe core. Furthermore, if the shell is sufficiently thin, then excitons localized entirely in the CdSe region also cannot be formed. The conclusion is that 3.3 eV photons are not absorbed throughout the entire particle. Thus, deposition of a thin CdSe shell results in essentially no increase in the high energy extinction coefficient. Figure 2.9 shows the ratio of the core/shell and core extinction coefficients at different wavelengths, as a function of the total particle volume. The volumes of core/shell nanoparticles are calculated from spectral calculations described in earlier studies,[7] and because of the problem of CdSe homogeneous nucleation contaminating the shorter wavelength region of the absorption spectra, the absorbance ratios are based on the excitation spectra.

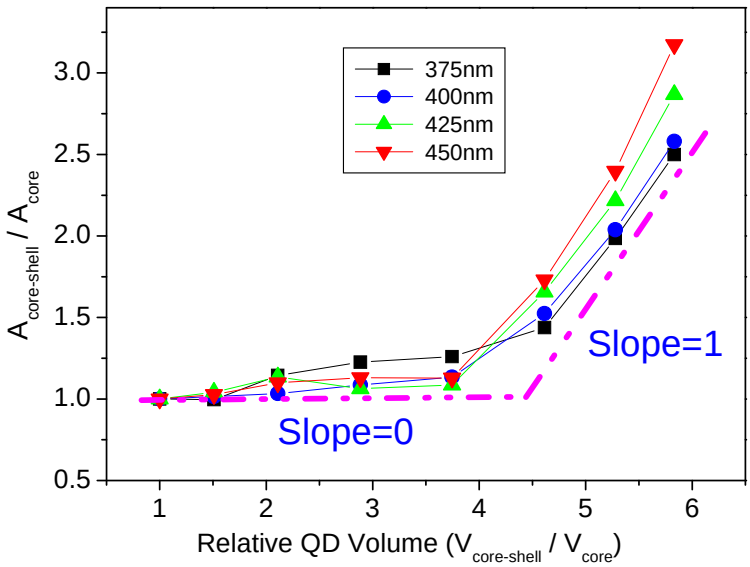

Figure 2.9. Short wavelength absorbances as determined from the excitation spectra for core to 7th injection of CdSe. The relative volume is the ratio of core/shell nanoparticle volume to CdTe core volume (d = 3.42 nm).

Deposition of the first approximately 1.0 nm of CdSe shell (volume ratio of about 4.0) has little effect on the shorter wavelength extinction coefficients. After having reached this thickness, further shell deposition causes the extinction coefficients to increase linearly with total shell volume. This behavior is in qualitative agreement with the energetics described above.

The lowest exciton extinction coefficients and radiative lifetimes of these type-II particles can be analyzed in much the same way as the single component CdSe and CdTe particles, above. The main difference is that the electron-hole overlap and hence the integrated extinction coefficient decrease with increasing shell thickness, as shown in figures 2.6 and 2.8. This factor and the shift of the luminescence to longer wavelengths cause the radiative lifetime to increase with increasing shell thickness. As in the single component QDs, the radiative lifetimes may be obtained from the PL decays, shown in figure 2.10.

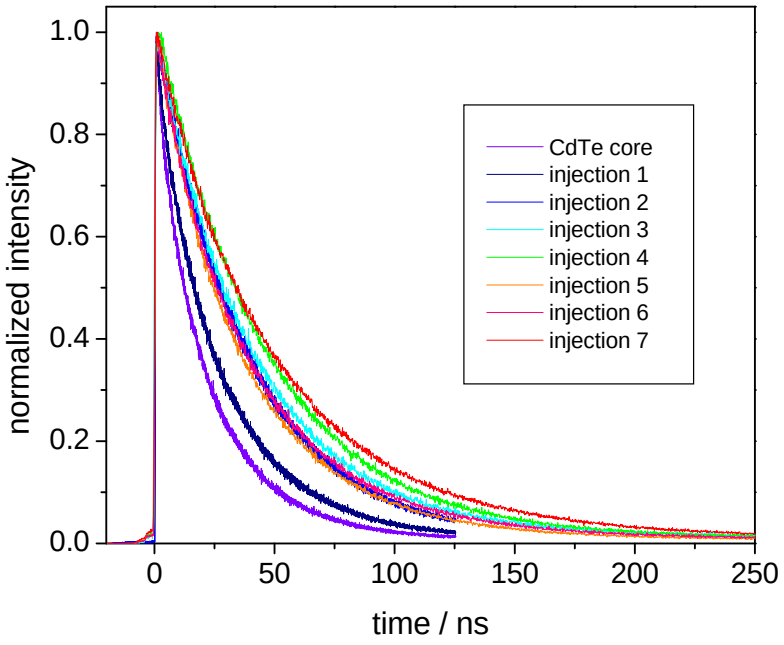

Figure 2.10. Normalized PL decay curves of CdTe/CdSe core/shell nanoparticles. The different decay curves correspond to the spectra shown in figure 2.6.

The luminescence characteristics of the particles and therefore the analysis of the PL decay kinetics is a function of shell thickness. Tri-exponential fitting results and quantum yield data are collected in table 2.1. Analysis of the CdTe core PL kinetics is straightforward; the decays are nonexponential and the quantum yield is considerably below unity, indicating the presence of particles having defects that result in nonradiative decay pathways. In this case, the longest lived component dominates the PL decay and is assigned to the radiative lifetime. An apparent quantum yield of the "bright" particles (those that are observed in a time-resolved PL experiment) can be calculated from the measured PL decay kinetics using the fact that the static luminescence intensity is proportional to the area under the corresponding decay curve. Specifically, Φ_{bright} is given by the ratio of the area under the decay curve to that of a purely radiative, single exponential decay having the same initial (t = 0) amplitude.

$$\Phi_{bright} = \int_0^\infty I(t)\,dt \Big/ \int_0^\infty I_0 \exp(-t/\tau_{rad})\,dt \qquad \text{equation. 2.8}$$

where I_0 is the initial amplitude of the decay curve and matches *I(t=0)* of the observed PL decay. The PL decay can be expressed in terms of the triexponential fitting parameters, $I(t) = \sum_{i=1,3} A_i \exp(-t/\tau_i)$, where A_i and τ_i are the decay time and fractional amplitude of the *i'th* component, respectively. Integration of equation 2.8 gives an equivalent expression for this quantum yield in terms of these fitting parameters, $\Phi_{bright} = \sum_{i=1,3} A_i\,\tau_i / \tau_{rad}$. For the CdTe core particles, this gives Φ_{bright} = 69%, which is considerably greater than the observed quantum yield of 41%. This difference indicates that only 59% (= 0.41/0.69) of the particles

are bright, and the other 41% are not observed in the PL decay experiment; they are "dark". The mechanisms that result in dark II-VI QDs have recently been studied and discussed.[30] A similar analysis can be applied to the particles with the thinnest CdSe shell (thickness of 0.25 nm, less than a complete unit cell monolayer). The shell injection 2 – 4 particles exhibit QYs of greater than 90%, and decays that are very close to single exponentials. In this case the interpretation is unambiguous: nearly all of the particles are bright and the measured decay times are close to the radiative lifetimes.

Table 2.1. PL decay analysis of CdTe/CdSe core/shell particles.

PL decay curves are fit to a tri-exponential decay where τ_i and A_i, i = 1 – 3 are component time and amplitude. Fast components that are too small to accurately measure (<1.5% of the total) are ignored. Φ is the sample quantum yield, and τ_{rad} is taken to be τ_3/Φ. (τ_{rad} for core and shell 1 is taken to be τ_3.)

Samples	τ_1	A_1	τ_2	A_2	τ_3	A_3	Φ	τ_{rad}	τ_{nr}
Core	1.5	8.9%	10.5	26.8%	26.5	64.3%	0.41	26.5	
Shell 1	1.2	4.4%	6.9	10.6%	28.1	85%	0.66	28.1	
Shell 2	-	-	38.4	98.0%	152	2.0%	0.97	39.6	1280
Shell 3	-	-	39.7	96.9%	124	3.1%	0.96	41.3	990
Shell 4	-	-	44.8	99.0%	240	1.0%	0.91	49.2	497
Shell 5	12.0	9.1%	37.7	88.0%	114	2.3%	0.77	49.0	164
Shell 6	12.7	9.2%	40.4	84.8%	155	2.1%	0.73	52.3	141
Shell 7	15.3	6.5%	50.3	88.3%	136	5.0%	0.74	66.3	188

Subsequent thicker shells show an interesting phenomenon. The QYs of the shell 5 – 7 particles (shell thicknesses of greater than about 0.9 nm) drop to 70 – 80% and the PL decay kinetics are more complicated. The dominant kinetic component has a decay time that is comparable to, or somewhat shorter than the longest decay times of the 2 – 4 shell particles. This is quite remarkable; although the electron-hole overlap continues to decrease and the spectrum shifts further to the red, the dominant decay component gets slightly shorter. The PL kinetics of these thick-shell particles also exhibit small amplitude shorter and much longer lived components. The amplitude of the long-lived component is too small for it to be assigned the radiative lifetime with the measured QYs. This is easily seen from the following simple QY calculation, taking the shell 7 as an example (see table 2.1). From equation 2.5, if the radiative lifetime is taken to be 136 ns and the measured decay for most of the particles (89%) is 50.3 ns, then the corresponding quantum yield for that subset of particles is about 37%. Following this (incorrect) logic, from table 2.1 we get 5% of the ensemble has a QY of 100% and 6.5% has a QY of 11%. The overall sample QY is then about 39%, which is inconsistent with a measured quantum yield of 74%. We conclude that such an assignment cannot be correct.

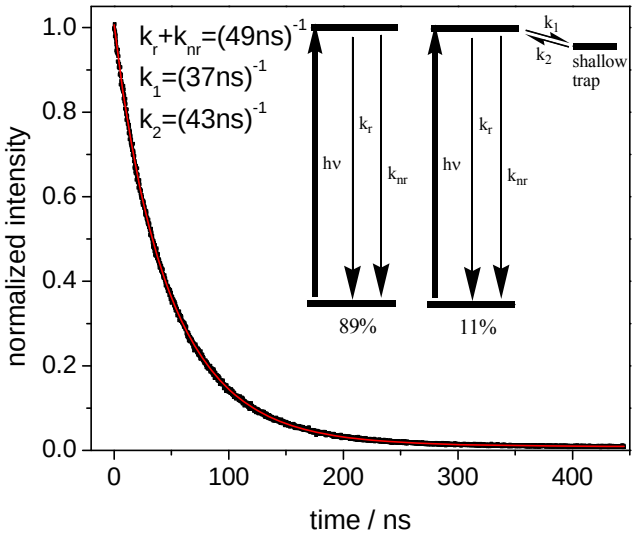

Figure 2.11. Experimental PL decay of the Shell 7 particles and a decay curve calculated on the basis of the proposed mechanism for the relaxation of CdTe particles with thicker CdSe shells, equation 2.7. Also shown is the kinetic scheme of the proposed relaxation mechanism.

We suggest that the QY and PL decay results can be understood in terms of a mechanism involving a small fraction (11%) of the particles having low lying trap states that can be reversibly populated, as depicted in figure 2.11. This mechanism leads to PL kinetics that are described by equation 9.

$$I(t)=\frac{A_t}{(k_+-k_-)}\left[(k_+-k_2)\exp(-k_+t)+(k_2-k_-)\exp(-k_-t)\right]+A_{nt}\exp\left(-(k_r+k_{nr})t\right)$$ equation. 2.9

where $k_\pm = \tfrac{1}{2}(k_1+k_2+k_{rad}+k_{nr}) \pm \tfrac{1}{2}\left((k_1+k_2+k_{rad}+k_{nr})^2-4(k_{rad}+k_{nr})k_2\right)^{1/2}$, and A_t and A_{nt} are the fractions of particles with and without shallow traps, respectively. For the S7 particles we have A_t= 0.11 and A_{nt} = 0.87. The quantum yield, Φ, and measured decay time, $\tau_d=(k_{rad}+k_{nr})^{-1}$, define the radiative and nonradiative rates through equation 2.6, specifically, $k_{rad}=\Phi/\tau_d$ and $k_{nr}=(1-\Phi)/\tau_d$. We note that this mechanism assumes that none of the particles are dark. Figure 2.11 shows that this mechanism gives an excellent fit to the experimental kinetics with k_1 and k_2 values of 0.027 and 0.023 ns^{-1}, respectively and a radiative lifetime of 67 ns. Table 2.1 also shows that the nonradiative rates increase dramatically with deposition of the fourth and fifth shells. There is a significant lattice mismatch between CdTe and CdSe and we suspect that this increase in radiative rates is due defects caused by lattice strain. We have recently shown that the lattice strain energy increases dramatically with shell thickness and it seems that in this case it is causing defect formation at this shell thickness.[31] Another possible interpretation of these results is that the radiative lifetime is given by the dominant decay component and k_{nr} is essentially zero. In this case the quantum yield being less than unity can be understood only in terms of a

significant fraction of the particles (1- Φ) being dark. The existing data cannot eliminate this possibility. However, recent results on the mechanisms which render particles nonluminescent suggest that a relatively small fraction of CdTe/CdSe particles are dark at room temperature, and makes this possibility seem unlikely.[30] Independent of these considerations, the radiative lifetime is bracketed by $\tau_d < \tau_{rad} < \tau_d / \Phi$, as shown in figure 2.12.

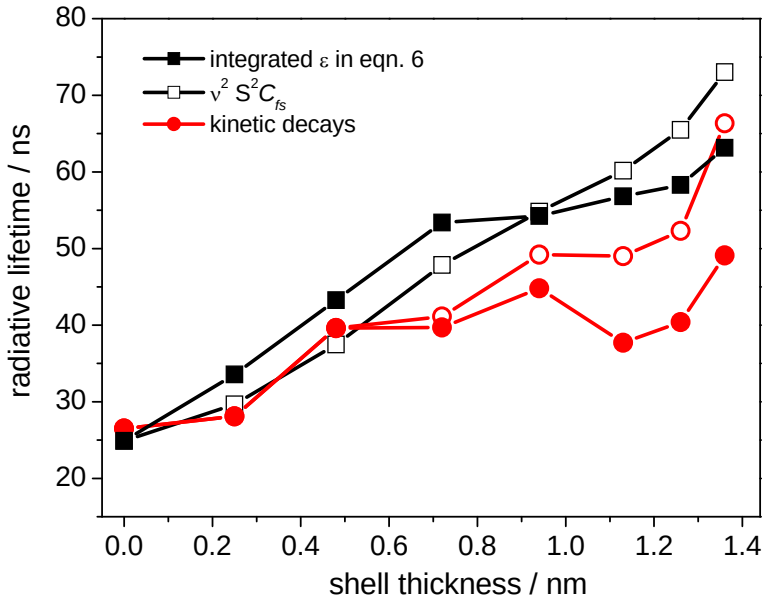

Figure 2.12. Radiative lifetimes determined from the PL decays using equation 2.8 are plotted with the open red symbols and the dominant decay times are plotted with solid red symbols. Radiative lifetimes calculated from equation 2.7, using measured integrated extinction coefficients and calculated Boltzmann populations in the fine structure levels are shown in solid black symbols and those calculated from the core radiative rate and scaled by calculated electron-hole overlaps, a ν^2 factor and Boltzmann populations in the fine structure levels are shown in open black symbols.

Radiative lifetimes determined from equation 2.7 gives a monotonic increase with shell thickness, as expected. In contrast, the taking the radiative lifetimes to be the dominant PL decay components result in values that are significantly lower than those determined for thinner shells. As shell thickness increases, the spectrum shifts to the red and the electron-hole overlap decreases. Both factors give longer radiative lifetimes. These considerations therefore strongly support the above assignment that the PL decays are accurately described by equation2.9.

These radiative lifetimes can be compared with those calculated from the integrated extinction coefficients. In addition to the relative integrated extinction coefficients and bandgap energies, the value of C_{fs} also varies with shell thickness. This is because as the electron and hole become further separated, the exchange splitting in the fine structure

become smaller and the Boltzmann population factors approach the high temperature limit. The fine structure energy splittings can be calculated for the CdTe core particles (above) and are taken to scale with the calculated spherical particle electron-hole coulombic energy. This interaction energy is calculated using the effective mass electron and hole wave functions, as detailed in reference7. With these energetics, C_{fs} values and subsequent radiative lifetimes can then be calculated. Alternatively, relative values of the core and core/shell radiative lifetimes can be taken to simply scale as the product of the electron-hole overlaps, the ν^2 factor and relative C_{fs} values. The two approaches give very similar results, as shown in figure 2.12. Figure 2.12 also shows that these results are in good agreement with the measured radiative lifetimes.

2.3.4 CdSe/CdS nanocrystals pectroscopy

To minimize the lattice strain effect and keep high QY, small ZB CdSe core particles are chosen to grow consequent CdS shells. Normalized absorption and PL spectra of the ZB CdSe core and CdSe/CdS core/shell QDs are shown in figures 2.13 and 2.14.

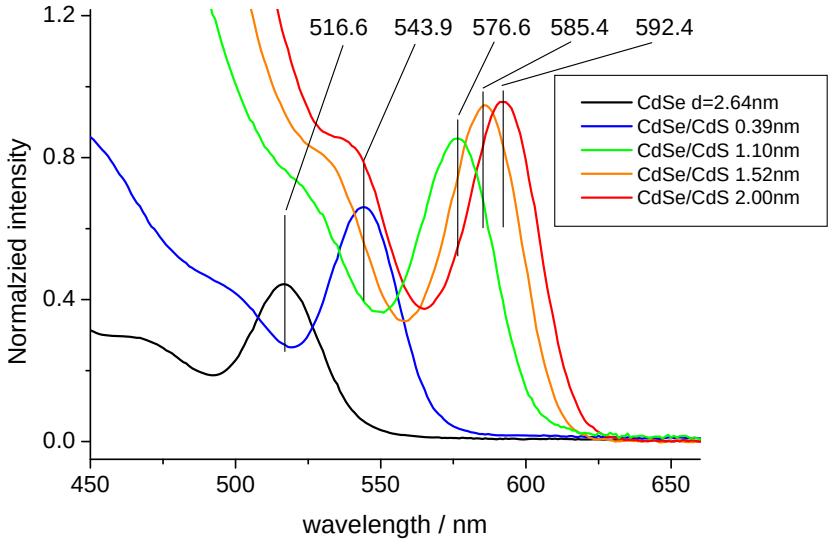

Figure 2.13. Normalized absorption spectra of 2.64 nm zincblende CdSe QDs and corresponding core/shell particles having shell thicknesses of 0.39, 1.10, 1.52, and 2.00 nm. The normalization is to the same particle concentration.

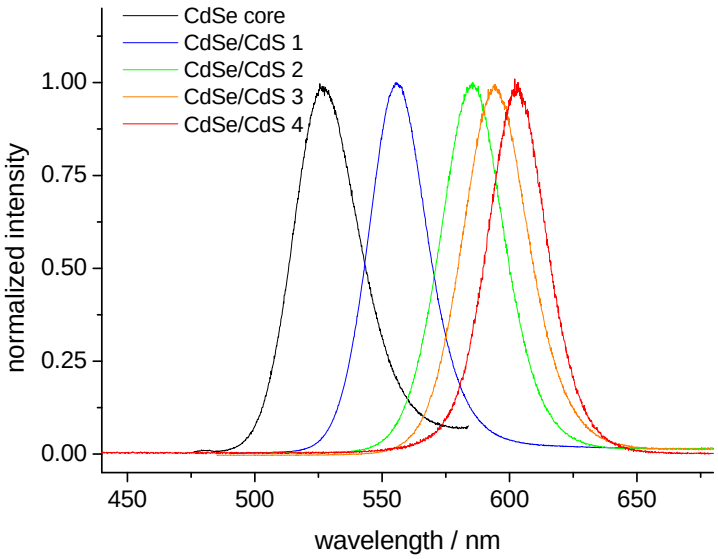

Figure 2.14. Photoluminescence spectra of the same QDs as in figure 2.13.

The size-dependent spectroscopy of wurtzite versus zincblende CdSe particles has not been extensively studied, but indications are that the crystal structure makes little difference in the effects of quantum confinement. This is not surprising, the energetic difference between the two forms is very small, 1.4 meV per CdSe. We shall therefore assume that size calibration curves obtained for wurtzite may also be applied to ZB particles. The cores have an absorption maximum at 516.6 nm, corresponding to 2.64 nm diameter particles, see figure 2.13. A TEM image of the core/shell particles having an absorption maximum at 592.4 nm (indicated as CdSe/CdS 4 in figures 2.13 and 2.14) is shown in figure 2.15.

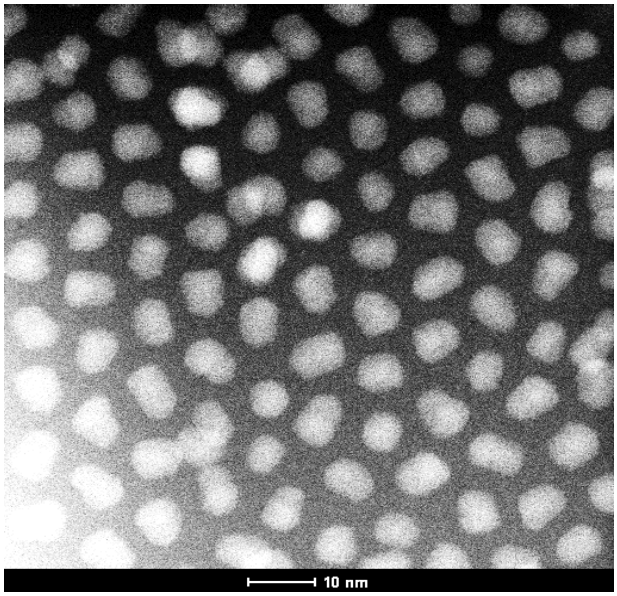

Figure 2.15. TEM image of the core/shell particles having an absorption maximum at 592.4 nm.

The particles are somewhat non-spherical, having dimensions varying from about 6.2 to 9.0 nm. The ensemble average dimension is obtained from the measurement of many particles and is found to be 6.6 nm. With the known core diameter of 2.64 nm, these images indicate that for these particles, the average shell thickness is 2.0 nm. The radiative lifetimes of these and several other core/shell particles having the same CdSe cores and different CdS shell thicknesses have been obtained from time-resolved PL measurements. The PL quantum yields of the core/shell particles are very high (> 80%, and usually about 95%) and the PL decays are dominated by a slow component that is taken to be the radiative lifetime. These lifetimes decrease with increasing shell thickness and exciton wavelength, as shown in figure 2.16. The longest decay component for the core particles is also shown. However, the quantum yield of the core particles is low and the radiationless decay may shorten this decay, compared to the actual radiative lifetime. As such, the measured value of 44.5 ns must be viewed as a lower limit on the actual radiative lifetime. We note that the radiative lifetime decreases with shell thickness and exciton wavelength. This is the same trend that is observed in bare CdSe core particles, and the opposite of what is observed in type-II QDs, such as CdTe/CdSe.[5]

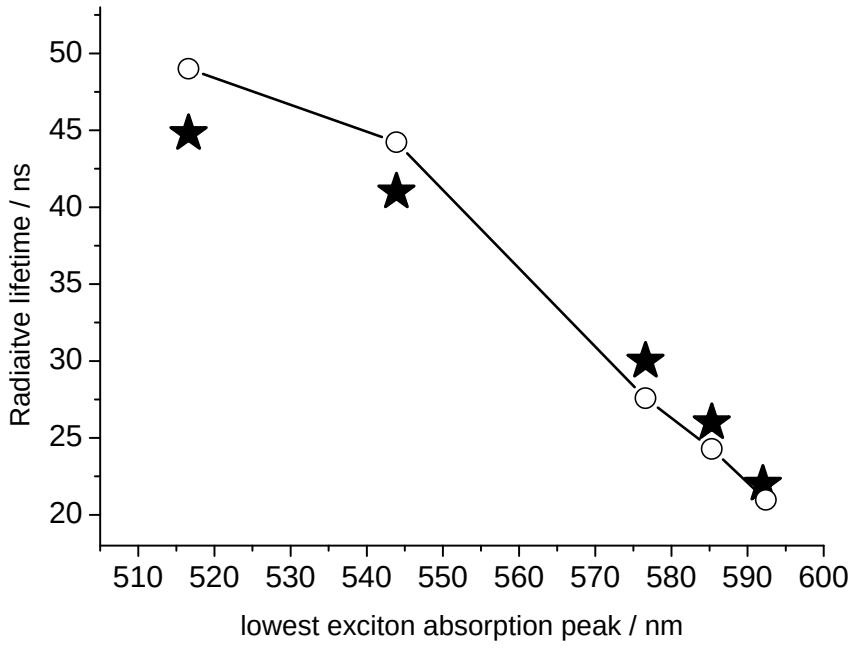

Figure 2.16. Radiative lifetime as a function of the wavelength of the lowest energy exciton in CdSe/CdS particles. The open circles correspond to radiative lifetimes calculated as described in the text. The 2.64 nm zincblende cores (the 516.6 nm point) have a low QY and the measured lifetime is unreliable.

It is of interest to compare the measured radiative lifetimes to values calculated from the adsorption spectra, using equation 2.7. Although the PL energies are trivially obtained from the static spectra, obtaining oscillator strengths and C_{fs} values is more complicated, and is discussed below. The approach taken here is the following: First, we determine exciton energy as a function of core size and shell thickness. This is a "map" of exciton wavelength for CdSe/CdS core/shell particles and allows spectroscopic determination of shell thickness. Second, these result are used to normalize the absorption spectra at 350 nm to the particle concentration. This normalization uses the known CdSe and CdS absorption coefficients and refractive indices, the appropriate local field factors and core and core/shell particle sizes (volumes). Normalized this way, the spectra give absolute absorption oscillator strengths for the lowest energy exciton. Finally, following evaluation of the C_{fs} factors, radiative lifetimes are calculated using equation 2.7. These values are then compared to those obtained from the time-resolved measurements. This set of calculations is discussed below.

In this set of calculations, the programs based on elastic continuum model and effective mass approximation coded in FORTRAN were written and modified for CdSe/CdS QDs by Professor Dave F Kelley.

1. Exciton energy as a function of core size and shell thickness.

Plots of spectral position for wurtzite CdSe/ CdS particles have been reported.[32] In these studies, the CdS shells were grown at relatively high temperature and subsequently annealed at 200 °C. This annealing can results in radial interdiffusion, broadening the core-shell interface. In contrast, the particles used here are zincblende and with the shells grown at much lower temperatures, <160 °C. Previous studies have shown that in addition to affecting in the radial composition profile, the shell growth temperature is crucial in determining the shell morphology when there is significant core-shell lattice mismatch. The core-shell lattice strain energy becomes large in the case of large cores and thick shells and can be relaxed by the shell taking on a very inhomogeneous local thicknesses – lattice strain causes the shells to become irregular. Core/shell particles grown at very low temperature do not as easily undergo surface reconstruction. They have uniform shell thicknesses and are metastable with respect to release of the lattice strains and shell roughening. The present zincblende core/shell particles may therefore be expected to have somewhat different spectroscopic properties than the particles studied in reference 32. We conclude that reliable, accurate plots of lowest exciton energy versus shell thickness for the present case of thick shells on zincblende CdSe/CdS particles have not been reported. Below we develop an accurate empirical method to determine the shell thickness for any combination of core and core/shell absorption maxima. We also modify these calculations to model other types of shell growth conditions.

The approach used here is based on the known CdSe sizing curve and calculation of the exciton energies using effective mass approximation (EMA) wavefunctions. Wurtzite and zincblende CdSe have very similar spectroscopic energetic and properties and we make the assumption that the wurtzite CdSe sizing curve can also be used for zincblende particles. EMA calculations are known to predict larger quantum confinement effects than what is observed. These errors are minimized by considering the electron and hole moving in potentials having finite barriers at the particle surface. However, even with these considerations, EMA calculations typically over-predict the extent of quantum confinement,

and the extent of these errors increase with increasing quantum confinement energy. The fundamental problem is that the effective mass is defined as $m^* = \hbar^2 \left(\frac{\partial^2 E}{\partial k^2} \right)^{-1}$, and the plot of E versus k is not quadratic at the larger quantum confinement energies of the smaller particles.[33] The obvious solution to this problem is, in addition to including finite surface barriers, to empirically correct the effective masses as a function of quantum confinement energy, and that is the approach taken here. Since most of the quantum confinement is in the conduction band electron, this empirical correction is applied only to the electron effective mass. Applying a correction to the electron effective mass means that the total quantum confinement energy depends on the electron effective mass and vice-versa. It follows that the correction factor to the electron effective mass must be calculated in a way that is self-consistent with the calculated quantum confinement energies. Throughout these calculations, the electron-hole coulombic interaction is treated as a perturbation. We find that the corrected electron effective mass may be given by, $m_e^*(corrected) = m_e^*(bulk)\left(0.36773 + 2.75634x10^{-4} E_{QC} - 8.3105x10^{-9} E_{QC}^2\right)$ where E_{QC} is the electron plus hole quantum confinement energy. The way this is implemented is to start out assuming the low energy (bulk) electron effective mass, calculate electron and hole quantum confinement energies, use these quantum confinement energies to get a corrected electron effective mass, and so on. This procedure converges to self-consistent values in a few iterations. With this correction, the EMA calculations very accurately reproduce the known CdSe sizing curve for particles having exciton wavelengths of 500 – 650 nm.[13]

These calculations are also applied to CdSe/CdS core/shell particles. This extension is non-trivial for two reasons. First, the presence of core/shell lattice mismatch, and second, the possibility of selenium and sulfur interdiffusion. Diffusion is a strongly activated process and appropriate to the low-temperature shell deposition conditions used here, we will initially ignore radial diffusion. The lattice parameter of CdSe is about 4% larger than for CdS, and the core-shell lattice mismatch results in the core being under isotropic pressure and the shell being under radial pressure and tangential tension.[34] These strains affect the respective conduction band energies, which is taken into account through an elastic continuum calculation using the known elastic parameters of each material.[35] The calculation gives the volumetric strain as a function of radial position. This result along with the volume dependent conduction band energy shifts allows calculation of an accurate conduction band radial potential, as was done in reference 7. The valence band potential is much less affected by strain, and is taken to be bulk values. Electron and hole wavefunctions are calculated using these potentials. A crucial parameter in the electron wavefunction calculation is the zero-strain CdSe-CdS conduction band offset, which is estimated to be between 0 and 0.3 eV.[36] If this is taken to be 0.047eV and the same electron effective mass correction factor is applied to the CdS conduction band electron, then this EMA calculation also accurately gives the exciton energy of the 6.6 nm core/shell particles, see figures 2.13 and 2.15. This approach has been used to calculate the exciton energies of a wide range of cores sizes and shell thicknesses. A map of the exciton energy as a function of core size and shell thickness is given in the appendix. The elastic continuum model is not a good approximation for very thin shells, (less than a full monolayer) and calculations for those particles are omitted.

The above map assumes a coherent core-shell interface, and a uniform shell thickness, which are good approximations for the zincblende particles. However, much of

the lattice strain energy is released upon forming a rough shell, and this occurs when thick wurtzite shells are grown at high temperatures and/or subsequently annealed. Furthermore, high-temperature shell deposition and subsequent annealing results in significant radial diffusion of the selenium and sulfur. This has the effect of changing both the conduction and especially valence band radial potentials. The conduction band potential is altered by the graded composition and the loss of volumetric strain. The valence band potential is not greatly affected by volumetric strain, but is affected by the change in composition profile. Valence band energies change nonlinearly with composition, a phenomenon referred to as "optical band-bowing" and this effect is included in the calculation of the valence band radial potential.[37] Having these potentials, we have also calculated core/shell exciton wavelengths maps for the case of no core compression, with and without radial interdiffusion. These diffusion dependent conduction and valence band potentials are obtained by solving the radial diffusion equation, as explained in reference 7. The resulting maps are significantly different that the low temperature zincblende map and are also given in the figure SI-2 and figure SI-3 of appendix. The map which includes the effects of radial diffusion is most appropriate to high temperature synthesized wurtzite core/shell particles. We find that if the product of the diffusion coefficient and time is set to 0.03, then the resulting map is very similar to that in reference 32, differing in exciton wavelength by at most a few nanometers. Assuming a 1 hour annealing time,[32] this corresponds to a Se-S interdiffusion coefficient of 5 x 10^{-4} nm^2 min^{-1}, which is the same order magnitude as reported for Te-Se interdiffusion reported in reference 7.

2. Exciton oscillator strengths.

Size-dependent extinction coefficients of the lowest energy exciton may be determined by normalizing the absorption spectra by the particle concentration. This is done by normalizing the absorbance to the particle volume at a wavelength sufficiently blue that quantum confinement effects are unimportant. In the present case, the 350 nm absorbances are normalized to the particle volumes, using the known 350 nm absorption coefficients for CdSe and CdS. (In the case of core/shell particles, the absorption at 350 nm may have a contribution from small, homogeneously nucleated CdS particles. Using the present synthesis, this is typically a small contribution (< 10%) and is corrected for by the comparison of the absorption and luminescence excitation spectra.) The 350 nm complex refractive index for CdSe[11, 38] and CdS[38] are n_{CdSe}= 2.772, k_{CdSe}= 0.7726, and n_{CdS}= 2.58, k_{CdS}= 0.70. The absorption spectra are normalized at 350 nm by the products of the absorption coefficients and particle volumes. The extinction coefficients at λ = 350 nm are taken as[13]

$$\varepsilon_{QD}(\lambda) = \frac{2\pi N_A}{0.2303\lambda}\frac{2n_{CdSe}k_{CdSe}}{n_s}\left|f_{LF}\right|^2\left(\tfrac{4}{3}\pi r_c^3 + \frac{n_{CdS}k_{CdS}}{n_{CdSe}k_{CdSe}}\tfrac{4}{3}\pi\left((r_c+h)^3 - r_c^3\right)\right) \qquad \text{equation 2.10.}$$

where r_c is the core radius, h is the shell thickness, λ = 350 nm and f_{LF} is the local field factor. (Equation 2.10 uses SI units.) The local field factor is given by[13, 39]

$\left|f_{LF}\right|^2 = \dfrac{9n_s^4}{\left(n_p^2 - k_p^2 + 2n_s^2\right) + 4n_p^2k_p^2}$, where the subscripts p and s refer to the particle and solvent, respectively. Evaluation with the CdSe refractive index and chloroform solvent gives a value of $|f_{LF}|^2$ = 0.285 at 350 nm. Equation 2.10 gives a 350 nm extinction coefficient of 3.57 x 10^5 $M^{-1}cm^{-1}$ for the 2.62 nm CdSe core particles. If the 1S exciton extinction coefficient is taken

to be 1.63 x 10^5 $M^{-1}cm^{-1}$(reference 32), then the ratio of these extinction coefficients is in quantitative agreement with the core spectrum in figure 2.13. Using the literature ratio of 350 nm absorbance coefficients, $n_{CdS}k_{CdS} / n_{CdSe}k_{CdSe} = 0.84$, equation 2.10 can also be applied to the core/shell spectra. Integrated extinction coefficients are then obtained from fitting the low energy part of these spectra to a series of Gaussians and taking the area of the one corresponding to the $1S_{3/2}$-$1S_e$ transition. This normalization has been applied to the spectra in figure 2.13.

3. Radiative lifetime calculation.

Radiative lifetimes are given by equation 2.7, with C_{fs} given by equation 2.4. Calculation of C_{fs} amounts to calculating the dark-bright splittings and thermal populations as a function of shell thickness.[4a] This calculation also considers population in the $1P_{3/2}$ hole level, which has only a slight effect.[5-6] We take the dark-bright splitting to be dominated by the electron-hole exchange interaction, which scales as the reciprocal of the electron-hole separation. The electron and hole wavefunctions are calculated to obtain the exciton energy map described above and can be used to calculate expectation values of 1/r. These are used to obtain relative values of E_i compared to those in the core, which are taken from Efros et al.[4a] Using values of C_{fs} obtained from equation 2.4, the integrated extinctions coefficients and the exciton energies, equation 2.7 is readily evaluated. A plot of these radiative lifetimes is also shown in figure 2.16. Very good agreement with the measured decays is obtained for all but the bare CdSe core particles. This may be understood in term of the fact that the core particles exhibit a low QY and the long decay component therefore does not reliably give the radiative lifetime. We note that core radiative lifetime is calculated to be 49 ns, in quantitative agreement with the previously reported value for wurtzite QDs.[5]

It should be noted that this calculational approach uses only the observed spectra and literature data; the calculation of the radiative lifetime has no adjustable parameters. The integrated extinction coefficients of the core/shell particles are obtained directly from the static absorption spectra and the known 350 nm absorption coefficients. The values of C_{fs} for the appropriate sized core particles are from results reported by Efros et al.,[4a] and values for the core/shell particles are calculated using calculated expectation values of 1/r. All of the calculated results are in good agreement with radiative lifetimes obtained from time-correlated photon-counting measurements. The Einstein relations (of course) very accurately predict radiative lifetimes. One of the conclusions of this study is very simple: these equations are useful only when careful measurements are made and all of the appropriate quantities are accurately evaluated.

These results also show that the radiative lifetimes decrease with shell thickness, similar to the size dependence of one-component CdSe quantum dots.[5] This is in sharp contrast to what is reported in type-II core/shell QDs, such as CdTe/CdSe.[7] The difference is primarily a result of how the electron-hole overlap varies with shell thickness. In the present case of CdSe/CdS, the band offsets are referred to as type-1½, where the hole is localized in the core and the electron is delocalized throughout the core and shell. In type-II QDs such as CdTe/CdSe, the band offsets are such that the hole is localized in the core and the electron is localized in the shell. The result is that increasing shell thickness causes the electron-hole overlap decreases much more rapidly in the type-II, compared to type-1½ QDs. This puts less of the oscillator strength in the $1S_h$-$1S_e$ transition for the type-II QDs, resulting in longer radiative lifetimes.

2.4 Conclusions

The conclusions drawn from the results and analyses on the four types of QDs studied here can be summarized as follows.

CdSe. PL decay measurements on very high quantum yield CdSe QDs indicate that the radiative lifetimes decrease from about 40 to 25 ns as the core diameter increases from 2.5 to 5.0 nm with a constant shell thickness. Three factors control the size dependent radiative lifetimes: the integrated extinction coefficient, the bandedge energy and the Boltzmann fraction of the population in the bright versus dark fine structure levels. The observed values for the high quality CdSe and CdSe/ZnSe QDs can be quantitatively understood through calculation of these parameters and application of elementary theory. Lower quality CdSe QDs give slightly shorter decay times, particularly for the smaller particles. This difference is assigned to nonradiative process that are absent in the high quality and core/shell particles.

CdTe. PL decay measurements on CdTe QDs indicate that the radiative lifetimes increase from about 25 to 35 ns as the particle diameter increases from 3.0 to 5.0 nm. The radiative lifetime size dependence in CdTe and CdSe QDs are determined by the same factors: integrated extinction coefficient, bandedge energy and fine structure populations. However, the radiative lifetimes of CdTe and CdSe QDs show opposite size dependencies. This is primarily because the CdTe extinction coefficients are almost size independent and the CdSe extinction coefficients increase with increasing size.

CdTe/CdSe. These are type-II QDs, and as such, the electron and hole are localized in the shell and core, respectively. Calculated electron wavefunction overlaps with the $1S_{3/2}$ and $2S_{3/2}$ hole functions decrease and increase, respectively, with increasing shell thickness. This factor, along with the decrease of the exciton energy are the primary reasons that the radiative lifetime gets longer with increasing shell thickness. As the electron becomes more delocalized, the magnitude of the electron-hole exchange interaction decreases, changing the energies of the fine structure levels. Quantitative agreement between measured radiative lifetimes and values calculated from integrated extinction coefficients requires assessment of the Boltzmann populations of the fine structure levels.

CdSe/CdS. Recent synthetic advances made available very monodisperse zincblende CdSe/CdS quantum dots having near-unity photoluminescence quantum yields. Because of the absence of nonradiative decay pathways, accurate values of the radiative lifetimes can be obtained from time resolved PL measurements. Radiative lifetimes are also obtained from the Einstein relations, using the static absorption spectra and the relative thermal populations in the angular momentum sublevels. One of the inputs into these calculations is the shell thickness, and it is useful to be able to determine shell thickness from spectroscopic measurements. we use an empirically corrected effective mass model to produce a “map” of exciton wavelength as a function of core size and shell thickness. These calculations use an elastic continuum model and the known lattice and elastic constants to include the effect of lattice strain on the band gap energy. The map is in agreement with the known CdSe sizing

curve and with the shell thicknesses of zincblende core/shell particles obtained from TEM images. If selenium-sulfur diffusion is included and lattice strain is omitted then the resulting map is appropriate wurtzite CdSe/CdS quantum dots synthesized at high temperatures, and this map is very similar to a previously reported one. Radiative lifetimes determined from time resolved measurements are compared to values obtained from the Einstein relations, and found to be in excellent agreement. Radiative lifetimes are found to decrease with shell thickness, similar to the size dependence of one-component CdSe quantum dots and in contrast to the size dependence in type-II quantum dots.

CHAPTER 3. THERMAL QUENCHING MECHANISMS IN II-VI SEMICONDUCTOR NANOCRYSTALS.

3.1 introduction

The temperature dependence of the photoluminescence (PL) of II-VI semiconductor quantum dots (QDs) has been extensively studied. Most of these studies involve very low temperatures. Temperatures well above ambient are of interest to lighting applications and in this regime both the reversible and irreversible loss of quantum yield are serious impediments to the implementation of QDs in commercial devices.

At the lowest temperatures the change in QY is due to a thermal equilibrium between excited states that have significantly different probabilities for radiative decay. These excited states are due to the angular momentum fine structure of the lowest exciton transition and have different oscillator strengths for luminescent decay to the ground state. These states are characterized by their total angular momentum, and at the lowest temperatures most of the population is in the lowest energy, F = 2, state. Because PL from this state is forbidden, it is called the "dark exciton".[4a] The allowed states are at slightly higher energies, so elevating the temperature increases the relative population of these states and thus increases the overall radiative rate.[40] At room temperature the relative populations of these closely spaced angular momentum states is very insensitive to temperature, so this mechanisms is of minimal importance for photoluminescence intensity changes in this regime.

Above room temperature it is generally found that there are reversible and irreversible losses in the PL intensity.[41] Chemical processes such as ligand loss and oxidative degradation can lead to an irreversible loss of PL intensity, and although these processes can be of great importance for many different applications, they are not the focus of this paper. Instead, we seek to understand the mechanisms of the reversible loss of luminescence intensity, thermal quenching. Thermal quenching is often sufficiently large that it has been exploited[41a] as an optical method for thermometry that is compatible with remote sensing platforms. Walker *et al*. report[41a] thermal quenching of about 1.3% per °C for CdSe/ZnS nanoparticles from below room temperature up to 315 K. Such thermal quenching has been reported for both CdSe and for CdSe/ZnS core/shell particles, with the extent of thermal quenching decreasing with increasing ZnS shell thickness.[41b] The quenching mechanism has been generally assigned to thermally-activated carrier trapping and subsequent nonradiative recombination.[23b, 41b, 42]

"Static" and "dynamic" thermal quenching are mechanisms that have distinct phenomenologies. Dynamic thermal quenching is characterized by a temperature-dependent exciton lifetime that gives rise to a temperature-dependent PL decay. In this case the extent of quenching can be simply related to the change in luminescence lifetime. In static quenching the reduction in quantum yield does not affect the PL decay. These two types of processes can occur simultaneously: A QY decrease that is larger than the lifetime decrease indicates both static and dynamic quenching.

Dynamic thermal quenching is the result of a thermally-activated nonradiative recombination of conduction band electrons with valence band holes. In general, nonradiative decay channels occur in parallel with radiative decay. As the temperature increases, the nonradiative recombination rate becomes larger, which causes the PL decay rate to increase and the luminescence quantum yield to decrease. Temperature-dependent quenching processes could involve thermally-activated trapping of either electrons or holes, followed by nonradiative recombination. For dynamic thermal quenching to be significant, the thermally-activated process must occur on the same timescale as radiative decay, which is

about 20–30 ns for typical CdSe QDs. A recent paper concludes that dynamic quenching is due to thermally activated carrier trapping and/or thermally activated trap creation.[43]

The work in chapter 3 focuses on static thermal quenching, where some fraction of the particles are "dark" and therefore contribute to light absorption but not emission.[44] Static thermal quenching occurs because the fraction of dark particles increases with temperature. The dark particles undergo nonradiative decay on a timescale which is short compared to that of the time resolution of a time-correlated photon-counting experiment, typically 50 ps, and so do not affect the observed luminescence decay kinetics. Static quenching nonradiative processes are therefore orders of magnitude faster than the thermally-activated processes that cause dynamic quenching. Processes on intermediate timescales are typically not observed, so PL decay dynamics clearly distinguish between these mechanisms.

In this study, we investigate static thermal quenching in both CdSe and CdSe/ZnSe core/shell QDs as a function of surface composition and surface ligands. We also report results for CdTe and CdTe/CdSe QDs and find significantly less static thermal quenching than in most types of CdSe-based particles. Several possible mechanisms are considered and we conclude that the dominant mechanism is thermally-induced particle charging.

3.2 Experimental Section

Optical measurements.

In time resolved photoluminescence kinetics measurement, samples were excited with very low intensity 410 nm pulses at 1 MHz from a cavity-dumped frequency-doubled Coherent MIRA laser. The luminescence was imaged through a ¼ m monochromator with a 150 groove/mm grating onto a Micro Photon Devices PDM 50CT SPAD detector. The overall temporal response function of the system is about 400 ps. A small portion of the excitation beam was split off and imaged onto a UDT PIN 13DI photodiode. The voltage from the diode is measured across 1 kΩ, and varies linearly with the incident light intensity. When temperature-dependent results are collected, this voltage was used to normalize for laser intensity fluctuations. Samples were held in sealed 2 mm path-length silica cuvettes. The sample temperature was maintained by a home-made heated cell holder with a thermocouple and a digital temperature controller. Details of QY measurements are seen in Experimental Section of chapter 2.

Chemicals, particles synthesis, purification and ligand exchange.

Details are seen in Experimental Section of chapter 2.

Surface modification (Cd or Zn rich).

Usually all core and core/shell particles are made with excess of chalcogenide (e.g. Te/Se/S) and this is the general method to make surface with more cations (e.g. Cd/Zn). The following procedures is illustrating the modification of CdSe surface: The extracted CdSe sampleis put under vacuum at 100 °C for half a hour and dissolved in 4 ml of ODE. The vessel is heated to about 200 °C under nitrogen flow and an equal amount of cadmium oleate ($Cd(OA)_2$)/ODE precursor solution is added dropwise, while keeping stirring continually for several minutes, then cooled to room temperature. The aliquots of surface modified particles are extracted by chloroform:methanol (1:1 v/v) two times. Phase separation occurs and the nonpolar phase is kept. ODA/TBP ligand exchange is then accomplished as described above.

3.3 Results and Discussion

In this part, the initial thermal quenching was firstly done by Xichen Cai and the following major part was done by the strong collaboration with Professor Dave F Kelley, James E. Martin and Lauren E. Shea-Rohwer.

3.3.1 THERMAL QUENCHING IN II-VI NANOPARTICLES

CdSe cores and CdSe/ZnSe core/shell particles were synthesized using variations on standard methods.[45] The synthetic procedure used here yields CdSe/ZnSe particles having 3.2 nm diameter cores and a 1.08 nm thick shell. The synthesis reaction mixture contains excess octadecylamine (ODA), tributylphosphine (TBP) and TBPSe. Due to the excess TBPSe, the as-synthesized particle surfaces are known to be selenium rich.[46] The type of surface (selenium or cadmium rich) and the surface ligands are critical factors that determines the quantum yield and extent of thermal quenching. The original selenium rich surfaces can be made cadmium rich by further reaction of the purified particles with the cadmium precursor.[46] The ligands are exchanged by precipitation, followed by resuspended in an octadecene (ODE) solution containing a high concentration of TBP, ODA or TBP/ODA ligands at 110 °C for 1~2 hours. In all cases the particles are then precipitated, washed with methanol, and resuspended in toluene or chloroform and place in sealed cuvettes for spectroscopic measurements. CdTe and CdTe/CdSe particles were also synthesized using standard methods[7]. These particles are approximately 3.5 – 4.9 nm diameters and are ligated primarily with ligands present in the reaction mixture, octadecylphosphonic acid (ODPA) and oleic acid (OA) or its anhydride. In some cases, the ligands were exchanged for TBP and ODA. The details of all of the other experimental procedures are well described in the Experimental Section of chapter 2and chapter 3.

Typical temperature-dependent PL decay curves of CdSe/ZnSe particles (3.5 nm diameter cores with 1.0 nm thick shells) ligated with TBP/ODA ligands are shown in figure 3.1.

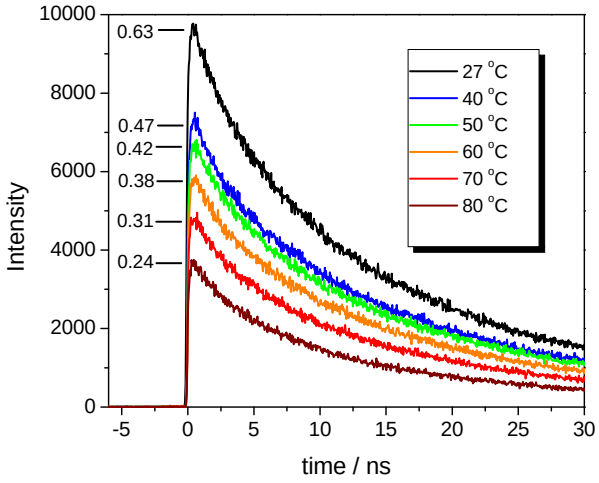

Figure 3.1. Decay curves obtained at different temperatures for CdSe/ZnSe nanoparticles having TBP/ODA ligands. Also shown are the fractions of bright particles at each temperature. The decay data extends past 120 ns (see figure SI-4 of appendix), but only the first 30 ns of data are shown here to clearly show the initial amplitudes.

These decay curves were collected under identical conditions and the intensities were normalized for variations in laser intensity so their relative intensities can be meaningfully compared. Increasing the temperature causes a significant decrease in the initial amplitudes, which are proportional to the fraction of bright (luminescent) particles. This decrease with increasing temperature therefore indicates static thermal quenching. Fitting of the decay curves shows that there is also a slight increase in the decay rates with increasing temperature, corresponding to dynamic quenching. Thus, both static and dynamic quenching with less extent, are occurring. The following work will focus on the differences in initial amplitudes, the static quenching.

The absolute fraction of bright particles at any temperature can be determined from a combination of the temperature-dependent decay curves and room temperature decay kinetics and QY measurements. This determination is first done at room temperature, where the overall QY is easily measured. The total QY is determined from the absorption and emission integrated intensity, relative to a standard dye (Rhodamine6G). The fraction of bright particles is given by the ratio of the total quantum yield to the quantum yield of the bright particles, $f_b = QY / QY_{bright}$. The QY of the bright particles is measured using the fact that the static luminescence intensity is proportional to the area under the corresponding decay curve. Specifically, QY_{bright} is given by the ratio of the area under the decay curve to that of a purely radiative, single exponential decay having the same initial (t = 0) amplitude with this expression

$QY_{bright} = \int_0^\infty I(t)\,dt \Big/ \int_0^\infty I_0 \exp(-t/\tau_{rad})\,dt$, where I_0 is the initial amplitude of the decay curve. The experimental decay results extend past 120 ns, by which the PL has decayed more than 99% of the way to zero. As a result, these areas can be determined very accurately. We find

that if the decay curves are fit to a triexponential, the dominant component is the slowest decaying component, and is about 26.9 ns. This is taken to be the radiative lifetime. This is the main reason we initially focus on CdSe/ZnSe core/shell particles – these particles have much higher quantum yields and the PL decay is closer to single exponential than in the case of bare CdSe particles. Having close to a single exponential decay reduces the uncertainty in the determination of the radiative lifetime. In conjunction with the bright fraction determined at room temperature, these amplitudes are used to calculate the temperature-dependent absolute bright fractions, also shown in figure 3.1.

Several of the assumptions in the above analysis require justification. We take the radiative lifetime to be equal to the longest decay time (26.9 ns at room temperature for the particles in figure 3.1). The PL decays rates are due to the sum of radiative and nonradiative processes, so the room temperature radiative lifetime can be longer, but cannot be shorter than the longest decay component. We note that this component is slightly longer than the reported room temperature radiative lifetime(22.7 ns[14] or 21.4 ns[15]) for CdSe particles having the same size as the cores in these CdSe/ZnSe core/shell particles, and shorter than the radiative lifetime (~ 33.0 ns) reported in figure 3.3 with optimized synthesis. Nevertheless, there is always some uncertainty in the radiative lifetimes that go into these calculations. Consideration of these relatively small uncertainties indicates that they have little or no effect on the final results. For example, if the radiative lifetime is actually longer than that obtained from the decay curve, then all of the bright fractions are proportionately larger, and nothing about the thermal quenching is affected. This analysis also assumes that the oscillator strength is temperature independent; the fractions of bright particles at elevated temperatures are determined from the relative initial amplitudes of the decay curves. The oscillator strength varies with temperature only through the changes in the Boltzmann population of the angular momentum fine structure levels. Using the known energy and oscillator strength differences of the fine structure levels, the extent to which the oscillator strength varies over this temperature range can be calculated.[4a, 47]

The angular momentum fine structure of spherical CdSe quantum dots has been calculated by Efros et al.[48] Relative energies and oscillator strengths of the eight transitions involved in the lowest exciton are calculated. The overall thermally weighted PL oscillator strength is given by $A_{fs} = \frac{\sum_i f_i \exp(-E_i/kT)}{\sum_i \exp(-E_i/kT)}$

where $f_i$are the oscillator strengths of the angular momentum sublevels. In the high temperature limit, $A_{fs} = \frac{\sum_i f_i}{8} = 0.375 f_i$, which is independent of particle size or crystal structure. In the simplest calculation with an assumed zincblende structure, the bright states are degenerate and at energies above the dark states. (Recent experimental studies have shown that the optical properties of zincblende and wurtzite CdSe nanocrystals are close to identical.[4b]) We get that at 300 K, the energy separation E_i = 7 meV, kT = 26 meV and A_{fs} = 0.314 f_i. The important thing to note is the effective oscillator strength is *greater* at higher temperatures. If non-radiative rates are constant, this would result in an *increased* PL intensity at high temperature, the opposite of the observed thermal quenching phenomena. We conclude that thermal changes in the angular momentum sublevels is a very small effect, corresponding to less than a 8% change in the effective PL oscillator strength, and can

therefore be ignored. As a result, the relative initial amplitudes of the temperature-dependent decay curves directly give the relative fractions of bright particles.

Plots of the ratio of dark to bright fractions of 4.0 nm CdSe cores with a 1.0 nm thick ZnSe shell are shown for particles with ODA, TBP and ODA+TBP ligands in figure 3.2. The TBP- and ODA-ligated particles give roughly similar fractions of bright particles at room temperature, but the latter give considerably more static thermal quenching. Particles ligated with both TBP and ODA give a considerably larger bright fraction. We can define the extent of static thermal quenching in terms of the fraction of bright particles, f_b, as 1-f_b(80°C)/f_b(24°C). Values of 35% and 40% are obtained for TBP and TBP/ODA ligated particles, respectively. ODA ligated particles give a larger value of 48%.

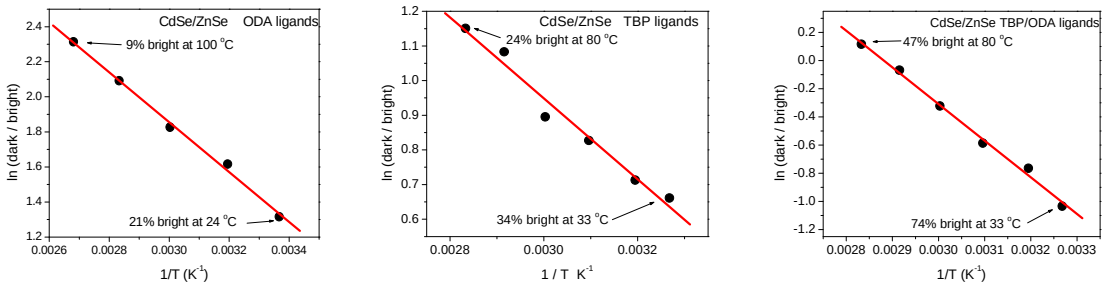

Figure 3.2. Plots of the fraction of dark versus bright CdSe/ZnSe particles with different surface ligands. Also shown are linear fits (red lines). The enthalpy change of the transition from bright to dark fractions corresponding to the straight lines are 122 meV (ODA), 100 meV (TBP) and 224 meV (TBP/ODA).

Qualitatively similar results are obtained with as-synthesized (selenium rich) 3.5 nm CdSe particles (no ZnSe shell), ligated with these combinations of ligands, as shown in figure 3.3. Smaller fractions of bright particles are generally observed in the particles lacking the ZnSe shell, but the same trends are observed with different ligands. Particles with TBP/ODA ligands have a higher fraction of bright particles and less static thermal quenching than those with just ODA ligands. The CdSe particles ligated with only TBP give very low PL QYs (<5%) and thermal quenching results for these particles were not obtained. We find that for both the CdSe/ZnSe and selenium rich CdSe particles, the extent of thermal quenching is almost independent of particle sizes. (see figure SI-5 of appendix)

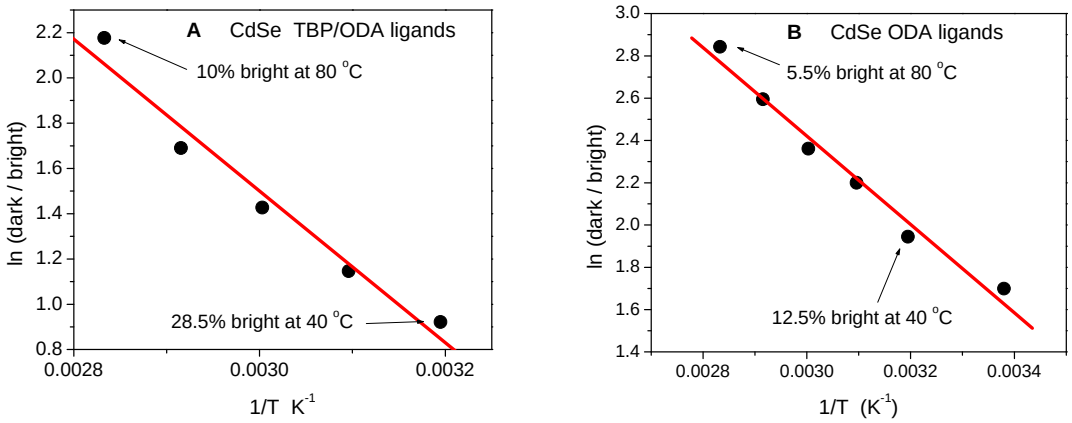

Figure 3.3. Plots of the fraction of dark versus bright 3.5 nm CdSe particles with different surface ligands. Also shown are linear fits (red lines) with the enthalpy change of the transition from bright to dark fractions corresponding 290 meV (TBP/ODA) and 180 meV (ODA).

A big change in the thermal quenching dynamics comes from surface modification. The selenium rich surface can be made cadmium rich by reacting these particles with a solution of the cadmium precursor.[46] This is followed by ligand exchange with TBP/ODA to give well-passivated, dominantly cadmium surfaces. Temperature dependent PL decays for particles having both selenium- and cadmium-rich surfaces are shown in figure 3.4. The initial intensities in figure3.4A correspond to the data in figure 3.3A.

The selenium-rich particles exhibit decays with rates that change little with temperature, but undergo extensive static thermal quenching. In contrast, qualitatively opposite behavior is observed with the cadmium-rich particles. Particles having cadmium-rich surfaces exhibit very little static thermal quenching, less than 10% from room temperature to 80 °C. However, figure 3.4 also shows that the cadmium-rich particles exhibit much faster PL decays than the selenium-rich particles, and that the decay times decrease with increasing temperature. Thus, the cadmium-rich particles undergo considerable dynamic thermal quenching over the same 25 – 80 ºC temperature range.

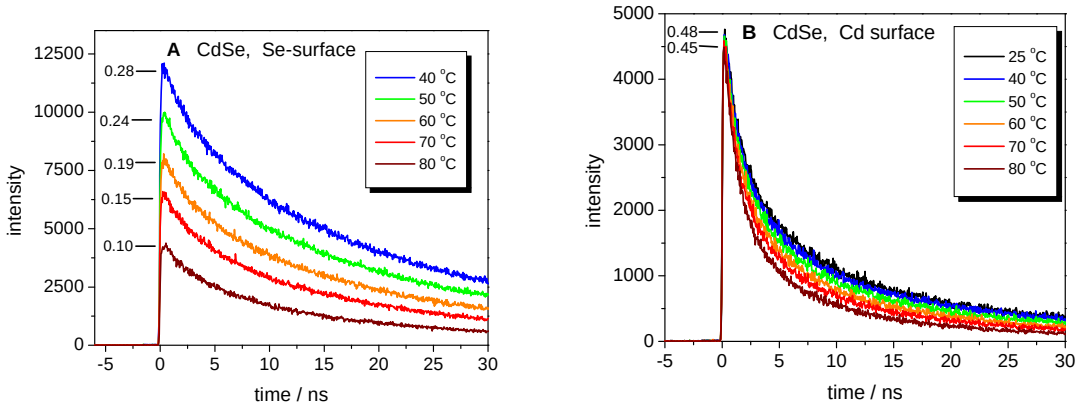

Figure 3.4. Decay curves obtained at different temperatures for A) selenium rich and B) cadmium-rich CdSe nanoparticles having TBP/ODA ligands. Also shown are the fractions of bright particles at (A) each temperature and (B) at 25 and 80 °C.

Somewhat different thermal quenching dynamics are observed for CdTe nanoparticles, as shown in figure 3.5.In contrast with the CdSe particles, the amount of static thermal quenching decreases with increasing nanocrystal size. The smaller (3.5 nm) particles exhibit about 30% static thermal quenching from 40 to 80 ºC. The larger (4.8 nm) particles exhibit about 12% quenching over the same temperature range. The corresponding plots of the fraction of dark versus bright fractions are shown in figure 3.5C.

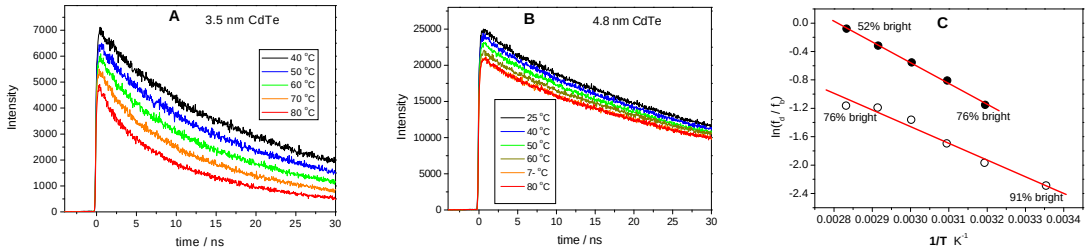

Figure3.5. Decay curves obtained at 40 °C to 80 °C for CdTe nanoparticles having sizes of A) 3.5 nm and B) 4.8 nm, and luminescence maxima at 595 and 670 nm, respectively. The surface ligands are primarily oleic acid and its anhydride and TOP from the reaction mixture. The temperature dependent initial amplitudes indicate about 31% and 12% static thermal quenching between 40 °C and 80 °C for the different sizes of nanocrystals. C) The corresponding plots of dark versus bright fractions for the 3.5 nm (solid circles) and 4.8 nm (open circles) particles. The enthalpy change of the transition from bright to dark fractions is 205 meV (4.8 nm particles) and 250 meV (3.5 nm particles) respectively.

The above results show that the fraction of bright CdTe particles changes only about 0.32% – 0.89 % per Kelvin, depending on the particle size. This can be compared to 2.5% or 0.96% per Kelvin obtained for the selenium-rich CdSe or CdSe/ZnSe particles (with TBP/ODA ligands)in figures 3.2 – 3.4. The extent of thermal quenching reported for CdSe/ZnS particles

is 1.3% per Kelvin,[41a] which is intermediate between these values. The data for CdTe/CdSe core/shell particles are given in the figure SI-6 of appendix. These particles show high room temperature QYs and somewhat less thermal quenching than the CdSe or CdSe/ZnSe particles. These results are also consistent with literature reports that CdTe/CdSe core/shell nanoparticles show very high room temperature quantum yields (> 80%) and very little thermal quenching up to 100 °C.[23b] More recent reports on CdTe/CdSe particles show a slight increase in PL lifetime and about 25% thermal quenching between room temperature and 100 °C.[43] The important points are that the extent of thermal quenching in CdTe nanocrystals is less than in CdSe or CdSe/ZnSe particles and decreases with increasing particle size.

Understanding the mechanism or mechanisms of static thermal quenching should explain why the extent of static quenching changes dramatically with surface composition, why it varies with the type of ligands, and why the quenching is less in the CdTe compared to the selenium-rich CdSe particles. Several different mechanisms for static thermal quenching are considered below. They can be broken down into three categories: structural, activated excited state, and electronic. The structural and electronic mechanisms involve an *inhomogeneous* distribution of ground state particles, with some fraction of the ground state particles being dark, i.e., some fraction of the unexcited particles are in a state that makes them non-luminescent following photoexcitation. This inhomogeneity is due to an equilibrium in the population of ground state particles and the observed static thermal quenching is thus due to the dark fraction being temperature dependent. In contrast, thermally activated excited state mechanisms that give rise to static quenching must involve processes that take place in competition with electron and hole relaxation to the band edge state. (Quenching processes that follow electron and hole relaxation affect the observed decay dynamics and thus give dynamic quenching.) In the following we argue that the structural and activated excited state mechanisms are not tenable, leading to the conclusion that static thermal quenching is largely due to an electronic mechanism in which valence band electrons are thermally promoted to unoccupied surface states. This leaves the core of the particle positively charged and hence dark.

3.3.2 POSSIBLE QUENCHING MECHANISMS

Structural mechanisms.

The most obvious structural mechanism is reversible ligation. This would involve an equilibrium, $P{\bullet}L(bright) \leftrightarrow P(dark) + L$ where P is an unligated particle and $P{\bullet}L$ is the particle with the bound ligand. The unligated particle is taken to have a dangling surface bond that acts as a recombination center, making the particle dark. Incomplete ligand coverage is known to occur, and affect the particle QY, in ambient dilute solutions.[49] The extent to which this type of mechanism is operative can be assessed by measuring the temperature-dependent timescale needed for the ligands to equilibrate and comparing this timescale to the tens of minutes timescale of the experiment.

We have compared the initial amplitudes of the temperature-dependent luminescence decays for the same CdSe/ZnSe particles in a solution of concentrated ODA/TBP ligands andin a solution having no excess ligands. We find that the particles in both types of solutions undergo almost entirely reversible quenching up to about 80 ºC, independent of the length of time that they are held at that temperature. The same is true for particles in a

solution of relatively concentrated ligands up to about 100 °C. However, when the particles in the pure solvent are held at 80 – 100 °C for more than a few minutes, they undergo extensive irreversible quenching. These results are summarized in figure 3.6.

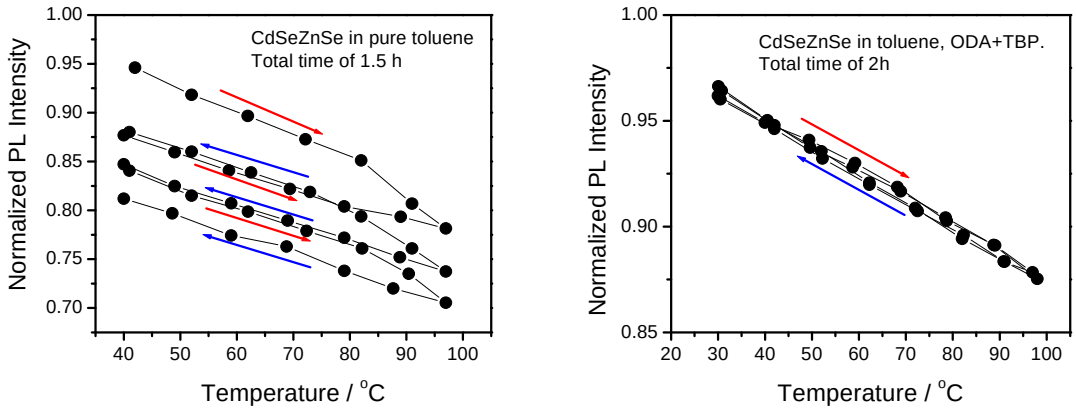

Figure 3.6. PL intensity as a function of temperature cycling for CdSe/ZnSe particles in pure toluene (left panel) and in a toluene solution of ODA and TBP ligands (right panel). Particles in toluene undergo irreversible ligand loss over about 80 ºC, resulting in an irreversible loss of PL intensity. These ligands are replaced and no irreversible loss is observed in the ODA/TBP solution.

The interpretation of this experiment is simple: the ligands exchange with the solution occurs on a timescale of tens of minutes at 80 – 100 ºC and much more slowly at lower temperatures. Thus, reversible ligation cannot account for the observed static or dynamic thermal quenching at the lower temperatures, as seen in figures 3.2 – 3.5. This type of mechanism also cannot account for the observed thermal quenching when the temperature is raised and the measurements are made very quickly, or when the QDs are in a medium with a high concentration of ligands. A reversible ligation mechanism also has difficulty explaining why CdTe and CdTe/CdSe particles show less thermal quenching than CdSe/ZnSe particles and the size dependence observed in the CdTe particles.

Other structural mechanisms can be considered, but seem very unlikely. For example, formation of structural defects in the particle itself would require the reversible scission of CdSe bonds. Formation of structural defects is somewhat analogous to solid state diffusion which also involves the scission of bonds within the crystal, and is known to have a high activation energy.[50] As such, structural changes are expected to be extremely slow at temperatures below 100 ºC. We conclude that most of the observed thermal quenching cannot therefore be explained by structural mechanisms.

Activated excited state mechanisms

Photoexcitation with light to the blue of the bandgap transition produces a state with the photogenerated electrons and holes having energies above the respective conduction and valence band edges. Relaxation from the initially excited state to the band edge state occurs relatively quickly, in time scale of several ps.[51] Quenching processes that take place in

competition with this relaxation are potential mechanisms for the observed static thermal quenching. Specifically, one can consider possible static quenching mechanisms involving trap states that are energetically inaccessible from the band edge, but can be rapidly populated from an unrelaxed state. In such a mechanism, electron (probably) or hole (possibly) trapping processes would compete with carrier relaxation to the band edge. These charge transfer processes are known to be quite fast.[27b, 51a] While both mechanisms can be considered, the electron would be the more likely carrier to be trapped because it has a much smaller effective mass with larger quantum confinement energy and therefore photoexcitation above the band edge results in the electron having most of the excess energy. Since carrier relaxation is very fast, the competition between trapping and relaxation would not be seen in either time-resolved PL or low temporal resolution transient absorption (TA) (> a few to tens of ps) experiments. This mechanism would be consistent with some fraction of absorbed photons giving essentially no PL, without any change in PL lifetime, and is thus a form of static thermal quenching. However, several types of evidence indicate that this is not significant part of the observed static thermal quenching. If this mechanism is operative, the extent of thermal quenching should depend on the excitation wavelength. Excitation near the band edge would result in little excess electron or hole energy and hence no static quenching. In contrast, we find that the extent of thermal quenching is almost completely independent of excitation wavelength (see figure SI-7 of appendix). The small excitation wavelength effects can be understood in terms of thermal shifts in the absorption spectrum.[52]

This fast trapping mechanism also seems to be inconsistent with the CdTe/CdSe results if the electron is the carrier being trapped. The CdTe conduction band is at considerably higher energy than that of CdSe. As a result, photoexcitation produces electrons that are much higher energy than in the CdSe case. According to this mechanism, CdTe or CdTe/CdSe particles should show a greater extent of thermal quenching than CdSe particles, contrary to what is observed. Other contradictions arise if the hole is considered to be the trapped particle. The hole is produced with very little excess energy and hole relaxation is very fast. CdSe/ZnSe core/shell particles are type-I with the electron and hole isolated in the particle core. Thus, surface hole trapping occurs only by tunneling through the shell. This tunneling would be expected to be comparatively slow and one would not expect to see extensive thermal quenching in these particles, contrary to observations. For the above reasons, we conclude that the fast trapping mechanism is at most a minor contributor to the static thermal quenching.

Electronic (charging) mechanisms.

Two types of thermal charging processes can potentially occur: the promotion of surface state electrons to the conduction band (negative core charging) and the promotion of valence band electrons to surface states (positive core charging). Each of these would result in the core of the particle being charged, with the counter charge remaining on the particle surface. Thus, the core of the particle has a delocalized charge, even though the entire particle remains neutral. Subsequent photoexcitation results in either two conduction band electrons and one valence band hole (an exciton in a negatively charged core, or a negative "trion") or two valence band holes and one conduction band electron (a positive trion). In either case, the trion could rapidly relax by an Auger process, so the charged particle would be dark.

Thermal production of negatively or positively charged particles have different spectroscopic manifestations because the spin states of the conduction and valence bands are two- and four-fold degenerate, respectively.[48] Negative charging results in significant conduction band state filling, but because of the valence band degeneracy, positive charging does not result in significant valence band state filling. Negative charging would therefore result in a significant reduction in the absorbance of the lowest exciton ($1S_e$-$1S_h$)transition and no change in the intensities of transitions involving higher conduction band levels (e.g. the $1P_e - 1P_h$ transition). A negative charging mechanism therefore predicts that increased temperature will diminish the intensity of the lowest energy transition, with little effect on the absorbance at shorter wavelengths. In contrast, positive charging has little effect on any part of the absorption spectrum. Absorption spectra of particles prior to ligand exchange taken at 10 °C and 100 °C are shown in figure 3.7. Higher temperature results in the well-known redshift of the spectrum[52] and a slight broadening, but the overall intensities of the different transitions remains close to constant. Specifically, these spectra show that the intensity of the lowest exciton transition ($1S_e$-$1S_h$) drops only very slightly, compared to the higher lying $1P_e - 1P_h$ transition. The temperature independence of the absorption intensities rules out negative charging as a significant thermal quenching mechanism. Figure 3.7 also shows that the particle absorbance changes very little (< 5%) at the 410 nm excitation wavelength. This rules out the possibility that a significant part of the observed static thermal quenching is an artifact of changes in the number of excited particles.

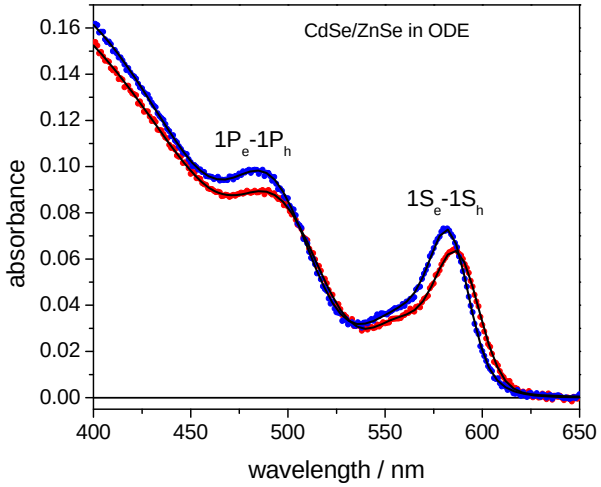

Figure 3.7. Absorption spectra of CdSe/ZnSe nanocrystals in ODE taken at 10 °C (blue dots) and 100 °C (red dots). Also shown are four-Gaussian fits to the experimental spectra (black curves). The relative areas of the $1S_e$-$1S_h$ to $1P_e$-$1P_h$ peaks are taken from the Gaussian fits and are 0.810 (10 °C) and 0.804 (100 °C).

Studies of thermal quenching as a function of particle size also rule out negative charging as a significant quenching mechanism. Quantum confinement results in a large, size-dependent shift in the conduction band energy. Because of the higher conduction band energy, smaller particles are predicted to be brighter and have a larger energy for becoming

dark than larger particles. Thus, a negative charging mechanism predicts a strong dependence of the bright/dark fraction on particle size, with smaller particles having less thermal quenching. However, figure 3.5 shows that the smaller CdTe particles exhibit more thermal quenching, contrary to what is predicted by a negative charging mechanism.

The above experimental evidence suggests that positive particle charging is responsible for most of the observed static thermal quenching and this mechanism is depicted in scheme 3.1. Such a mechanism is not unprecedented; it is essentially a thermal version of the photolytic mechanism that is commonly believed to be responsible for blinking.[53] This mechanism correctly predicts the lack of significant changes in the absorption spectrum with temperature. It is also consistent with the observed size dependence observed in the CdTe particles. Small particles have more quantum confinement and hence higher energy hole states. The higher energy holes states are above more of the Te 5P surface states and therefore exhibit more thermal quenching. This model effectively explains why the extent of thermal quenching depends on the nature of the surface (selenium or cadmium rich) and the surface ligands, as discussed below.

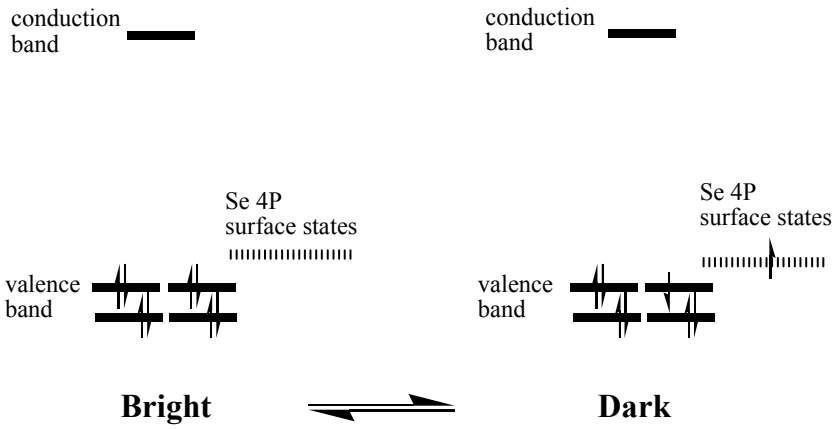

Scheme 3.1. The static thermal equilibrium involved in the positive charging mechanism in CdSe particles.

3.3.3 POSITIVE CHARGING MECHANISM: SURFACE EFFECTS

The selenium-terminated facets of a CdSe nanocrystal can have dangling (or weakly ligated) selenium 4P (or SP^3) orbitals. The top of the valence band is almost entirely composed of selenium P orbitals and the energies of these orbitals are expected to be comparable to the top of the valence band. We suggest that some of these surface states are just above the valence band and can act as electron acceptors. The energies of these surface states and the extent to which they are filled depend on the electron donation properties of the ligands and the Fermi level of the system.

This model predicts that the extent of thermal quenching should vary with the density of unoccupied surface selenium orbitals, and hence the fraction of the particle surface that is selenium (rather than cadmium) terminated. Changing a selenium-rich to a cadmium-rich surface eliminates most of the unoccupied (Se 4P) surface orbitals. Comparison of figures

3.4A and 3.4B provides compelling evidence for the involvement of the surface selenium atoms in the static thermal quenching mechanism. As predicted by this model, removal of the surface Se-4P orbitals drastically reduces extent of static thermal quenching. We note that making the surface cadmium rich also reduces the PL lifetime and overall quantum yield, due to the increased density of electron traps associated with surface cadmium atoms.

Ligand effects on the luminescence properties of CdSe nanoparticles have been extensively discussed by Kim et al.[54] and by Jasieniak and Mulvaney.[46] Kim *et al*. have synthesized particles in octadecene (ODE) and oleic acid (OA) without the usual amine and phosphine ligands. (The particles are synthesized from the reaction of $Cd(OA)_2$ and elemental selenium in ODE.) These core particles are initially ligated with only the weakly binding oleic acid or its anhydride. These ligands were then exchanged with propylamine, TBP or a combination of both. The addition of either TBP or propylamine resulted in a slight blue shift of the absorption spectrum, indicating that both types of ligands slightly etch the particles. Ligand exchange with propylamine resulted in a slight increase in the PL lifetime and an increase in the fraction of bright particles from 14% to 29%. Ligand exchange with TBP similarly lengthened the lifetime, but the fraction of bright particles decreased by a factor of three to 4.5%. The effects of a combination of TBP and propylamine ligands were very striking: The lifetime increased by a factor of 3 and the QY increased by more than an order of magnitude, with the bright fraction increasing to about 70%. Clearly, only the combination of propylamine and TBP passivates the particle surfaces, which implies that there are different surface binding sites with differing affinities for these ligands.

In the present studies, we exchanged the ligands on both the selenium-rich CdSe QDs and CdSe/ZnSe core/shell QDs with ODA, TBP or TBP/ODA and observe results that are qualitatively similar to those reported by Kim.[54](see figure SI-8 of appendix) These results can be understood in terms of how each of the ligands interacts with the particle surface: trialkyl phosphines bind very strongly with selenium and alkyl amines bind very strongly to cadmium or zinc. Through this binding, TBP removes the more weakly bound surface seleniums and passivates the more strongly bound ones. Removal of some of the surface seleniums leaves pendant cadmium or zinc atoms which can act as electron traps or electron donors if they are not removed or ligated. Similarly, ODA removes the pendant cadmium or zinc atoms and passivates the more strongly bound ones. How these interactions affect the surface orbital energies in particles with cadmium and selenium terminated surfaces is summarized in figure 3.8.

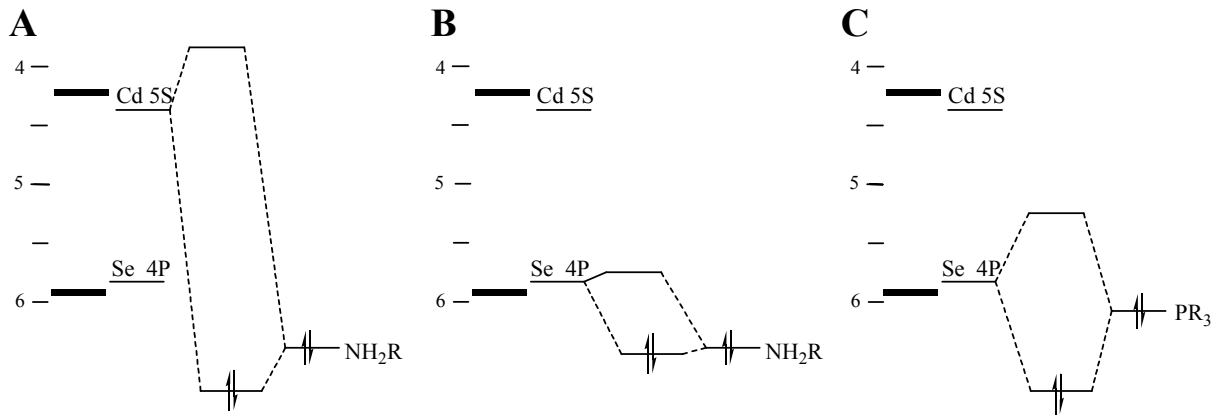

Figure 3.8. Schematic of the surface/ligand energetics. The vertical scale is approximate energies (in eV) with respect to vacuum. The CdSe valence and conduction band energies are indicated with thick lines and the surface Se 4P and Cd 5S energies are indicated with thin lines. Bonds are formed with a trialkyl phosphine (TBP) or a primary amine (ODA) with surface selenium 4P or cadmium 5S orbitals. The amine effectively passivates the electrons traps due to empty cadmium 5S orbitals (A), but has little interaction with the selenium 4P orbitals (B). The trialkyl phosphine is considerably higher in energy than the amine, (based on ionization energies and electronegativities) and therefore interacts more strongly with the selenium 4P orbitals (C).

The observed trends for how the presence of different ligands affects the exciton dynamics can be understood in terms of the energies of different orbitals and the Fermi level. The trapping and charging dynamics depend on the energies of the surface states and whether these orbitals are full or empty. An important general consideration is that the conduction band is primarily comprised of cadmium 5S orbitals and the valence band of selenium 4P orbitals.[18, 55] Thus, the surface cadmium 5P orbitals are at energies comparable to the conduction band and the surface selenium 4P orbitals are at energies comparable to the valence band. Charge neutrality requires that a stoichiometric, uncharged and unligated particle will have the selenium orbitals filled and the surface cadmium orbitals empty. Deviations from stoichiometry and ligation results in surface selenium orbitals that are empty or full depending on the redox potential (Fermi level) of the solution. The redox potential is determined by the redox equilibrium established in the synthesis reaction,[56]

$$R_3PSe + \left(R'COO\right)_2 Cd \;\rightarrow\; CdSe + R_3PO + anhydride$$

Because of the complexity of this reaction, it is difficult to calculate the exact value of the Fermi level. However, one expects that there could be both filled and empty 4P orbitals on the surface seleniums and we conclude that the extent to which the selenium 4P orbitals are filled depends on the specific ligands and their concentrations.

The ODA and TBP ligands interact with the cadmium 5S and selenium 4P orbitals differently. ODA ligates and interacts strongly with only the cadmium 5S orbitals. This interaction raises these orbitals above the conduction band, thereby removing the electron traps (figure 3.8A). The presence of ODA ligands therefore effectively passivates the cadmium- or zinc-rich nanocrystal facets, and ODA is commonly included as a ligand when

high QYs are desired. When ODA is the only ligand present, the selenium 4P orbitals are only weakly ligated (figure 3.8B). To the extent that these orbitals are filled, they can act as hole traps, resulting in a short PL lifetime and a low QY. The presence of unfilled orbitals above the valence band can result in thermal charging, and hence a large fraction of dark particles. We suggest that this is why the ODA ligated particles also show a small fraction of bright particles (see figure 3.2).

Due to the closer energetic proximity and greater polarizability, TBP more strongly ligates the selenium 4P orbitals, moving the empty orbitals to higher energy, as depicted in figure 3.8C. The 4P/TBP bonding orbitals are below the valence band and most of the 4P antibonding orbitals are too high to be thermally accessible. This interaction therefore removes most of these orbitals from being thermally accessible for valence band electrons, resulting in fewer charged particles and hence minimizes the extent of static thermal quenching. However, particles ligated with only TBP have a high density of electron traps. Some of these traps cause very rapid quenching, and a relative small fraction of these particles are bright. Ligation with TBP/ODA removes both the cadmium 5S and selenium 4P orbitals from the band gap. The conclusion from the above discussion of energetics is that a high QY is obtained only when both the surface cadmiums and the surface seleniums are passivated, which is consistent with the results in figures 3.2 and 3.3.

This model also explains the relatively small extents of thermal quenching in CdTe and CdTe/CdSe particles reported here and elsewhere.[23b] There are two important considerations regarding the differences between the CdTe and selenium-rich CdSe (and CdSe/ZnSe) particles. One is the extent of ligation to the trialkyl phosphines, TOP or TBP. There is certain equilibrium between the surface chalcogenide binding to the trialkyl phosphine and more weakly interacting species (amines or carboxylic acids). Only ligation with the trialkyl phosphine effectively removes the empty orbitals from being thermally accessible. Based upon relative bond strengths, this equilibrium should favor the trialkyl phosphine more in the case of a tellurium-, rather than selenium-terminated, surface. (This is easy to understand in terms of hard and soft Lewis acid-base arguments: tellurium is a softer Lewis acid than selenium, and R_3P is a very soft Lewis base.) The CdTe particles are therefore more likely to have surface chalcogenide atoms ligated to a phosphine, as opposed to a weakly interacting species. The other important consideration is the energy of the valence band electrons. The CdTe valence band is about 0.3 eV above that of CdSe. As a result, electrons in the CdTe valence band are at an energy above most of the surface chalcogenide orbitals, effectively filling those orbitals and removing them from the charging thermal equilibrium. The combination of these considerations is the reason that CdTe and CdTe/CdSe particles exhibit less thermal quenching than CdSe or CdSe/ZnSe core/shell particles. These considerations explain a very general observation: synthesizing CdSe particles (bare or core/shell) with quantum yields approaching unity requires precise control of the synthesis conditions and the ligand environment. However, synthesis of highly luminescent CdTe or CdTe/CdSe particles is extremely easy and much more forgiving of the exact synthetic conditions.

The effects of particle size can also be understood in terms of this mechanism. Particle size affects the surface area and the valence band energetics, which affect the extent of thermal quenching in opposite ways. All other things being equal, an increase in surface area will increase the number of unligated surface atoms and therefore the number of electron accepting surface states. However, larger particles have less quantum confinement and hence

the valence band electrons are at higher energy. In the case of CdTe particles, most of the surface tellurium orbitals are ligated and the surface area effect is minimized. The result is that energetic effect dominates and thermal quenching decreases with increasing size. Little effect of particle size is observed in 3.5 – 4.8 nm selenium-rich CdSe particles (see figure SI-5 of appendix). This suggests that in this case, both energetic and surface area effects are operative.

Changing the nature of the chalcogenide at the surface also results in competing effects. The selenium 4P orbital is at a lower energy than the tellurium 5P orbital. Thus, comparing CdTe and CdTe/CdSe core/shell particles, this factor would favor fewer thermally accessible surface states in the core/shell particles. However, selenium atoms are less effectively ligated by phosphines, favoring more surface states. The net effect is that with the smaller CdTe cores, the presence of the CdSe shells results in a slight increase in the extent of thermal quenching. We note that when smaller core CdTe/CdSe particles are have their ligands exchanged with just ODA (no TBP), then there is a very high density of unligated surface states and these particle give almost as much thermal quenching as do CdSe/ZnSe particles following similar ligand exchange. In the case of the larger CdTe cores,the valence band is at such high energy that very little thermal quenching is observed with or without a CdSe shell.

This thermal charging mechanism permits a simple interpretation of the apparent energies to make the particles from bright to dark states. The slope of the plot from figure 3.2 and 3.3 gives the average energy barrier of the empty surface orbitals that are thermally populated. There are two caveats from these approximations that must be kept in mind. First, there are many different environments for the surface chalcogenides due different crystal facets, step edges and so on, and correspondingly many different types of chalcogenide to ligand bonding. This results in a distribution of orbital energies that can be involved in charging. Thus, in the absence of other particle darkening mechanisms that are not thermally activated, the enthalpy obtained from the plot of the dark to bright ratio represent an average of the energies barrier of the orbitals that are thermally populated. Second, there are usually other mechanisms that can result in a particle being dark. The most common example is the occurrence of rapid trapping of conduction band electrons at surface states, followed by radiationless decay. This gives particles that are dark, independent of the temperature. The presence of other darkening mechanisms complicates this simple analysis. The conclusion is that the apparent energy is easily interpreted only when there is little electron trapping. As indicated in figure 3.8, ODA ligates the surface cadmium or zinc atoms and thereby effectively passivates the electron traps. In the case of CdSe particles ligated with only TBP (no ODA), there is such extensive electron trapping that these particles are essentially nonluminescent. In all cases where ODA ligates the surface cadmium atoms and the electron traps are effective passivated, similar enthalpy in the 180 to 290 meV range are obtained. The differing extents of thermal quenching reflect different densities of thermally accessible unpassivated orbitals.

3.4 Conclusions

The central conclusion from these results is that static thermal quenching results primarily from valence band electrons being thermally promoted to empty surface orbitals.

This results in a positively charged particle core, which upon photoexcitation gives a trion. The trions undergo relatively rapid Auger decay, rendering the particle dark. Since the charging occurs by electron transfer from the valence band to surface states, this mechanism depends on the nature of the surface, the surface ligands and the energy of the valence band. These considerations explain the diminished thermal quenching observed in CdTe, compared to CdSe particles and the effects of ligands that effectively bind the surface chalcogenide orbitals.

CHAPTER 4. SURFACE CHARGING AND TRION DYNAMICS IN CDSE-BASED CORE/SHELL QUANTUM DOTS

4.1 introduction

The usual picture of the ground state electronic structure of CdSe quantum dots (QDs) is that the valence band has a somewhat complicated structure but under normal circumstances is completely filled and the conduction band is empty. The valence band is formed primarily from the selenium 4p orbitals and the conduction band from the cadmium 5s orbitals. The degeneracy of the selenium 4p orbitals results in the more complicated valence band fine structure, but does not affect the overall picture in which the valence band is completely filled.[4a] This simple picture does not consider the role of surface states. A particle having nanometer dimensions has a significant fraction of the atoms on the surface and in the absence of complete passivation by the surface bound ligands, these surface states can play a major role in the overall particle electronic structure. In the case of CdSe nanoparticles, surface orbitals can be associated with either cadmium or selenium atoms. As such, surface orbitals in the energetic vicinity of the valence band are predominantly of selenium 4p character. CdSe and related II-VI semiconductor quantum dots are typically synthesized in the presence of trialkyl phosphines and primary alkyl amines and these molecules are typically the dominant surface ligands. Trialkylphosphine ligands are known to passivate the surface chalcogenides.[46] Most of the evidence indicates that the phosphine bonds directly to the chalcogenide,[46, 54, 57]although there is some debate about passivation mechanism.[58] The presence of phosphine-selenium bonds is consistent with simple ideas of hard/soft interactions and is why trioctylphosphine selenium is used as a selenium precursor in particle synthesis precursor.

In considering thermal processes, we are most concerned with the bonding of orbitals that are energetically close to the top of the valence band. In the case where the surfaces are perfectly passivated, all of the surface seleniums are bonded to phosphines and the resulting molecular orbitals are below the energy of the top of the valence band. Ligation of the selenium atoms results in these orbitals being filled by the lone pair electrons of the phosphorous; the selenium-ligand interaction is a ‘dative’ or Lewis acid-base bond. In the absence of a phosphine ligand, a surface selenium is coordinately unsaturated. The selenium orbital corresponding to the ‘dangling bond’ has an energy that depends on its location on the crystal surface and may be slightly above the valence band edge. If this orbital is filled or partially filled, then it can donate an electron to a photoinduced vacancy in the valence band. In this case, the hole of the photogenerated exciton can be filled by transfer of the surface electron and luminescence from the exciton is quenched – the surface orbital is a hole trap.[59] The phenomenon of carrier trapping in surface states is well known and trapped carrier radiative recombination often results in broad, red shifted luminescence.[60] However, unpassivated surface selenium orbitals may also be partially or completely empty and accept charge from the delocalized valence band – a situation that has been far less studied. The presence of unfilled selenium surface orbitals is easy to understand. QD synthesis using a source of neutral selenium atoms such as trioctylphosphine selenium results in roughly stoichiometric particles having surface selenium atoms lacking a full 4p shell and thus being able to accept electrons. If the energies of the unligated orbitals are sufficiently close to the valence band edge, then valence band electrons may be thermally promoted to these surface states. The charging and discharging of the surface orbitals results in a ground electronic state equilibrium between the electron being in the valence band and in the surface state, as depicted in Scheme 3.1.

It is important to note that it is the presence of unligated surface seleniums that gives rise to the surface charging. If an electron is in the surface state, then although the particle as a whole is neutral, the particle core is positively charged. It follows that the density of empty orbitals just above the valence band controls the extent of surface charging. This can be varied by controlling the presence of selenium binding ligands, such as trioctylphosphine (TOP) or tributylphosphine (TBP). These considerations apply not only to surface seleniums in CdSe and CdSe/ZnSe particles, but also to surface sulfur atoms in CdSe/CdS core/shell particles.

The presence of a surface charging equilibrium has profound implications for the photophysics of the quantum dot.[30] If a particle in the charge separated state absorbs a photon, then the particle core has two valence band holes and one conduction band electron. The surface electron is a spectator to the interior charges, commonly referred to as a positive "trion".[61] The trion may undergo a relatively rapid Auger process in which the conduction band electron recombines with one of the valence band holes, giving the energy to the other hole. This results in radiationless recombination of the exciton, making the particle dark. We recently invoked this mechanism to understand static thermal quenching in CdSe and CdSe/ZnSe QDs in chapter 2 and 3.[30] In those studies we found a reversible decrease of the photoluminescence (PL) quantum yield with increasing temperature, with essentially no change in the PL decay kinetics. This was assigned to a temperature dependent shift in the surface charging equilibrium, and hence the fraction of the particles that are dark.

Although there have been some studies trion lifetimes, most of the reported measurements have been on negative trions, and far less has been done on positive trions. Negative trions are often reported to be fairly long lived. For example, in a CdSe/CdS dot in rod, a negative trion lifetime of 11.6 ns is obtained, compared to the exciton lifetime of 65 ns.[62] The CdTe/CdSe negative trion has a shell thickness dependent lifetime of several nanoseconds.[63] Another report puts the CdSe negative trion lifetime at about 1 ns, about a factor of 7.5 longer than the biexciton.[64] Other studies give much shorter negative trion lifetimes. Electrochemically produced negative trions give a lifetime of 150 ps.[65] The rates for negative trions are reported to be very strongly size dependent[66] and part of the variability of reported Auger rates may be due to particle size and shape variations. The other variable which may not be well controlled is the density of surface electron traps, which could affect the extent to which the electron is in the conduction band versus a surface state. Because of the two conduction band electrons, the negative trion radiative rate is twice that of the neutral exciton (ignoring fine structure effects). Thus, significant radiative recombination can occur within the longer reported lifetimes. The negative trion states are thus not completely dark and are often referred to as "gray" states. These negative trion states can give a third, intermediate state in addition to the usual on-off dynamics seen in blinking studies.[47, 67] The positive trion shows considerably shorter lifetimes,[61] and is assigned to the off state in blinking studies. Because of the Auger processes involved in determining their lifetimes, the lifetimes of the negative and positive trions are related to the biexciton lifetimes,[61]

$$\frac{1}{\tau_{xx}} = 2\left(\frac{1}{\tau_{x+}} + \frac{1}{\tau_{x-}}\right) \qquad \text{equation 4.1.}$$

where $\tau_{xx,}$ τ_{x-}, and τ_{x+} are the biexciton, negative trion and positive trion Auger times, respectively. This relation follows from the fact that the biexciton can undergo Auger recombination by excitation of an electron (like a negative trion) or by excitation of a hole (like a positive trion). The factor of 2 results from the Auger pathway degeneracy. If the

negative trion recombination is much slower than that of the positive trion, then to a first approximation, the positive trion time is simply twice that of the biexciton.

In this chapter we measure ligand dependent positive trion and biexciton Auger rates for zincblende (ZB) CdSe/CdS and CdSe/ZnSe QDs. The results show that positive particle cores, and hence positive trions are readily formed through a room temperature equilibrium between electrons in the valence band and in normally empty surface states. We show that the solution chemistry controls the extent of unligated surface chalcogenides and therefore the extent of surface charging with keeping all other conditions same. This is done through the analysis of ligand dependent PL quantum yield and decay kinetics, along with the comparison of biexciton and trion Auger dynamics. These results show that the trion and biexciton Auger dynamics are in accord with equation 4.1, and with trion and biexciton dynamics in literature reports.[68]

4.2 Experimental Section

Chemicals.

Details are seen in Experimental Section of chapter 2.

Particle synthesis and sample preparation.

The zincblende CdSe core and following CdSe/CdS nanocrystals were synthesized and purified using slightly modified procedures reported by Nan et al.[8] The details can be seen in Experimental Section of chapter 2. In all cases, the core diameters and shell thicknesses were determined from the absorption spectra and published sizing curves[13, 69] and figure SI-2 of appendix.

CdSe/ZnSe core/shell particles were synthesized following slightly modified procedures reported by Pu et al.[70] A selenium suspension was prepared by dispersing Se powder (0.0237 g, 0.3 mmol) in ODE (3 mL). The zinc acetate-octylamine suspension was prepared by sonication of zinc acetate dihydrate (0.0465 g, 0.3 mmol) and octylamine (0.5 mL) in ODE (2.5 mL). In a typical ZnSe shell growth reaction, a mixture of ODE (2.0 mL), ODA (10 mg), and oleylamine (1.0 mL) was heated to 60 °C in a three-neck flask under argon flow, and then about 1.0 mL of purified CdSe core solution (containing about 1×10^{-7}mol of nanocrystals estimated by their extinction coefficients) was added to this flask. The amount of precursor solution for each injection was estimated using standard SILAR procedure. The Zn and Se precursors were added dropwise into the reaction mixture at 130 °C and 180 °C respectively. The reaction mixture was kept at 180 °C for 15 to 20 minutes then cooled to 130 °C. Another cycle of ZnSe shell precursors were added and those procedures were continued to reach the desired number of ZnSe monolayers.

The final reaction solution was extracted by hexane/methanol (volume ratio of ~1:1) twice. The non-polar phase containing the particles was separated and heated under vacuum to remove the residual hexane and methanol. The dried sample was then dissolved in octadecene and ligand exchanged with excess TBP or TBP/ODA at 100 °C for about half an hour. It is well established that ligand exchange often occurs at room temperature and is complete within a few minutes under these conditions.[30, 58, 71]After ligand exchange, the sample was centrifuged and liquid layer is kept. The particles were precipitated by the addition of anhydrous methanol, dried under vacuum, and then dispersed in chloroform for the spectroscopic measurements.

Optical measurements.

Transient absorption spectroscopy experiments were carried out using an apparatus that has been previously described.[72] Briefly, the instrument is based on a Clark CPA 2001 light source and a Princeton Instruments LN2 cooled CCD. The light source produces 150 fs, 600 μJ, 775 nm at a repetition rate of 1 kHz, which are attenuated and frequency doubled for sample excitation (387.5 nm at an excitation power of 0.4 – 15 mW and a spot size of 15.8 mm^2). CdSe/CdS samples were held in rapidly stirring 1 cm cuvettes having an absorbance at the excitation wavelength of about 1.2 to 1.5 which, for CdSe/CdS is about a factor of 5 or 6 larger than at the lowest exciton. This gives an average photon absorbed per pulse <N> about 0.06 and 0.65 at low and high power densities. CdSe/ZnSe samples have absorption at the excitation wavelength of about 0.6 to 0.8 and a correspondingly smaller excitation spot size of about 5.1 nm^2 was used.

Time resolved photoluminescence studies and quantum yield measurements were performed by the same procedures described in Experimental Section of chapter 2.

4.3 Results and Discussion

4.3.1 Luminescence spectroscopy of CdSe/CdS core/shell particles.

Figures 4.1 and 4.2 show the absorption and photoluminescence (PL) spectra of zincblende CdSe/CdS core/shell particles having the nearly identical cores and two different thicknesses of shells. The core diameters are 2.64 and 2.61 nm and the shell thicknesses are 1.0 (figure 4.1) and 1.48 nm (figure 4.2). The lowest energy exciton peak shifts from 516 nm to 573 nm(figure 4.1) or 584 nm(figure 4.2) upon shell deposition, indicating that the electron delocalized into the shell, forming "type-1½" or "quasi-type-II" heterostructures. The figures show that particles with both shell thicknesses have PL quantum yields that depend on the nature of the surface ligands. In this study, we focus on two types of ligands, octadecylamine (ODA) and tributylphosphine (TBP). The surface densities of each type of ligand are controlled by subjecting newly synthesized particles to different ligand exchange environments, either excess ODA or excess TBP and ODA at 100 °C. Figures 4.1 and figure 4.2 show that higher quantum yields are obtained with particles that are exchanged with TBP/ODA compared to ODA. The TBP/ODA and ODA quantum yields are78% and63%, respectively, for the 1.0 nm thick shells (figure 4.1) and 76% and 62%, respectively, for the 1.48 nm thick shells (figure 4.2). We also note that we consistently find that particles having 1.2 – 2.0 nm thick shells are more photostable than the ones with thinner shells, ≤ 1.0 nm, and will come back to this point later.

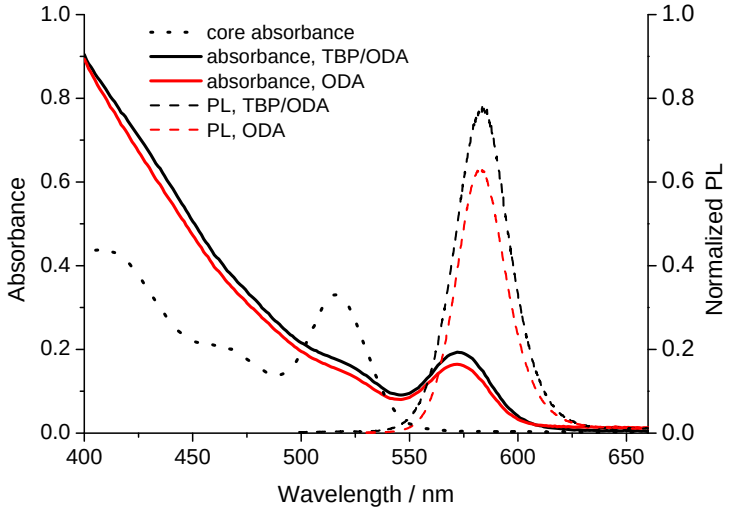

Figure 4.1. Absorption spectra of the 2.64 nm diameter zincblende CdSe core and CdSe/CdS core/shell particles having a shell thickness of 1.0 nm, with ODA and TBP/ODA ligands. Also shown are the corresponding PL spectra of the core/shell particles. The PL intensities are normalized such that the maximum intensity corresponds to the quantum yield.

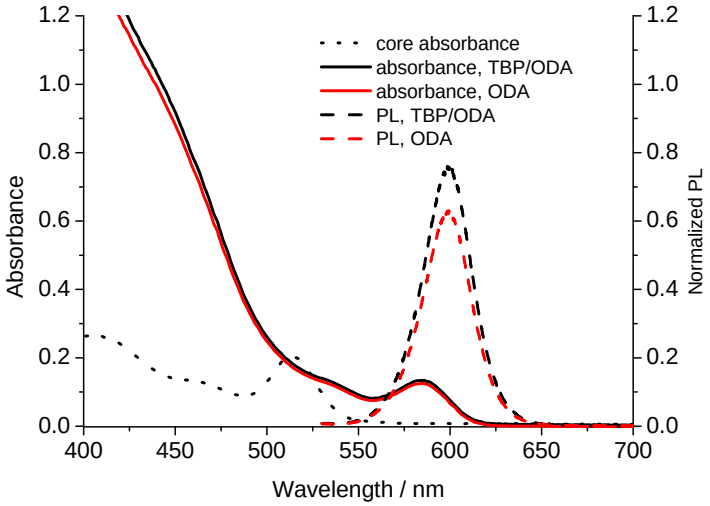

Figure 4.2.Same as figure 4.1, except the core diameter was 2.61 nm and the shell thickness is 1.48 nm.

The particles with ODA and TBP/ODA ligands exhibit very similar normalized PL decay curves, as shown in figure 4.3. The TBP/ODA kinetics are accurately fit to a biexponential decay having a 24.3 ns(66%) and 7.7 ns (34%) decay components. The long component is the same as the previously reported radiative lifetime for particles having the

same core size and shell thickness in chapter 2.[69]The presence of the shorter decay component implies that the quantum yield of the particles observed in the time-resolved PL experiment is about 77%, in approximate agreement with the overall static measured quantum yield of 76%. The conclusion is that the time-resolved PL experiment sees essentially all of the particles. This is not the case for the ODA ligated particles, for which a similar analysis gives a 72% PL QY for the particles observed in the time-resolved experiment and an overall static measured quantum yield of62%. The conclusion is simple: some of the particles ligated with only ODA are "dark"; they have lifetimes that are sufficiently short that they are not detected in a time-correlated photon-counting experiment having a time resolution on the order of 100 ps. In this case the fraction of dark particles is about 14%.

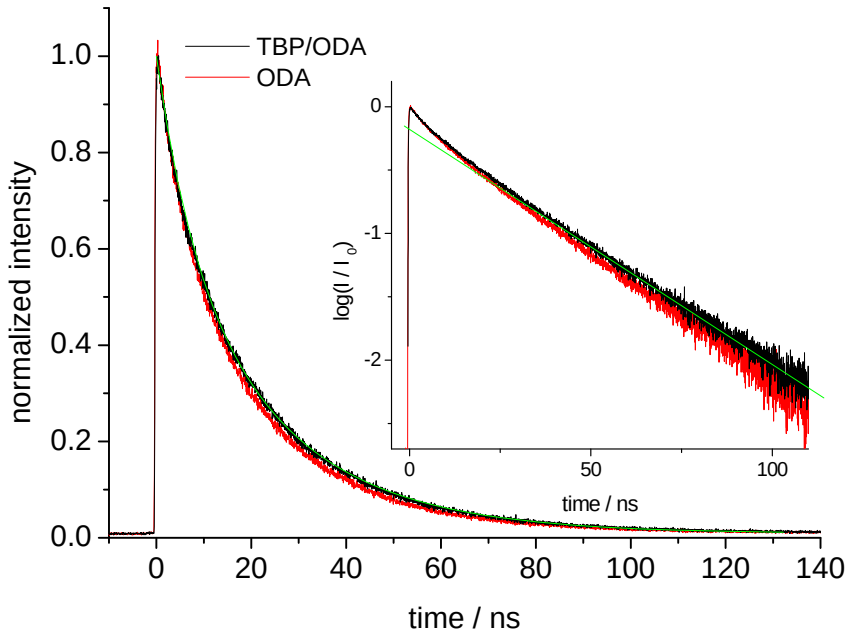

Figure 4.3. PL decay kinetics of the 1.48 nm shell CdSe/CdS core/shell particles having ODA (red) and TBP/ODA (black) ligands. Also shown is a fit curve corresponding to a 24.3 ns(66%) and 7.7 ns (34%) decay (green curve). Insert: log-scale plot of the TBP/ODA and ODA kinetics and a straight line corresponding to a 24.3 ns decay.

We have done ligand exchange, followed by this analysis on several different batches of CdSe/CdS particles, and obtained consistent results. We find that for particles ligated with TBP/ODA, the fraction of bright particles is typically over 80% and often over 90%. In contrast, for particles ligated with only ODA, typically 15% to40% of the particles are dark. This comparison shows that the fraction of dark particles depends on the surface ligands and is larger for particles lacking trialkylphosphine ligands. Trialkylphosphine ligands are known to passivate the surface chalcogenides, and the increased dark fraction being associated with the lack of TBP indicates that the fast quenching process is due to a process that involves states that are near the top of valence band. There are two possibilities: hole

trapping to surface states or thermal promotion of a valence band electron to a chalcogenide surface state.

We suggest that the dominant mechanism by which particles are dark involves surface charging, rather than a fast hole trapping process. We note that if the ligand dependent fraction of dark particles were due to either electron or hole trapping, one would expect there to be many different types of traps resulting in a broad distribution of trapping times. Figure 4.3 shows an approximately 7 ns component in the PL decay kinetics which may reasonably be assigned to electron or hole trapping. However, figure 4.3 shows that no evidence of decay components on the300 ps to 5 ns timescale in the PL kinetics. The lack of intermediate decay components suggests that trapping in this type of QD is relatively slow and cannot explain the presence of dark particles. This consideration is suggestive, but not definitive. In addition, there are two compelling reasons for this assignment. First, as explained in chapter 3, only this assignment can explain the previously reported thermal quenching results. The second, and most compelling reason is the comparison of the trion and biexciton lifetimes presented in the following sections.

4.3.2 TRANSIENT ABSORPTION SPECTROSCOPY OF CDSE/CDS CORE/SHELL PARTICLES.

Figure 4.4 shows the low power, lowest exciton bleach recovery kinetics for 1.0 nm shell particles with ODA and TBP/ODA ligands following 387 nm. Under these conditions, the number of photons absorbed per particle per pulse can be calculated from the 387 nm extinction coefficient, pulse energy and beam spot size. This value can also be estimated from the static lowest exciton absorbance and the magnitude of the observed bleach. Both estimates give about 0.06 photons/pulse and we observe that further reduction of the power has no effect on the decays. The figure shows that in the low power regime, the ODA ligated particles have a 136 ± 13 ps decay component, which is 30% of the initial bleach. The TBP/ODA capped particles have a similar, smaller amplitude decay component, which is 10% of the initial bleach. The amplitudes of these fast decay components are consistent with the dark fractions assessed from the PL quantum yields and decays, discussed above. The 136 ps decay is assigned to the lifetime of the trion, τ_{X+}.

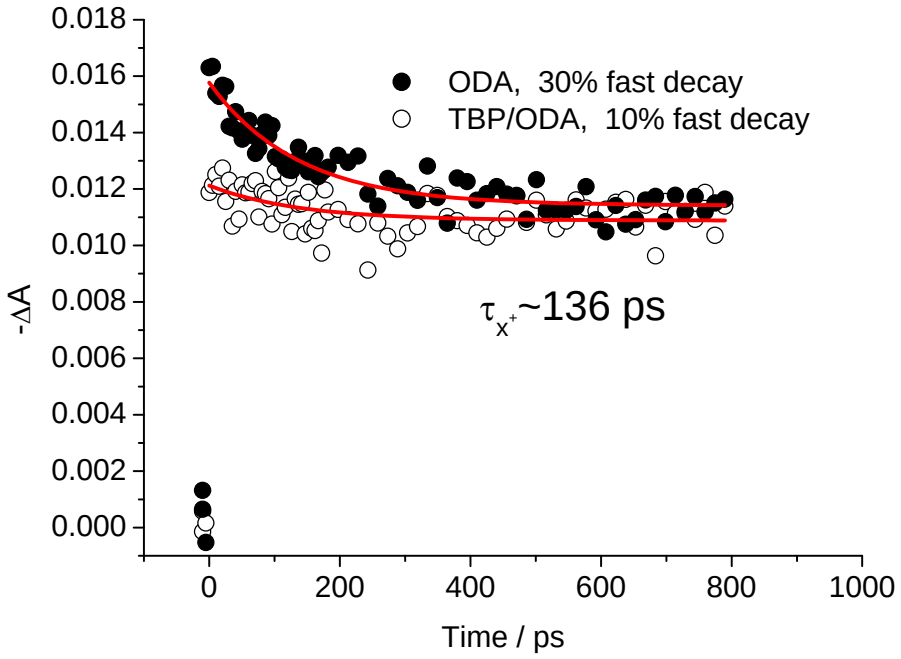

Figure 4.4. Low power transient absorption kinetics of lowest exciton from the thin shell (1.0 nm) CdSe/CdS core/shell particles. The 136 ps components are 30% and 10% of total bleach for ODA and TBP/ODA, respectively.

Higher power kinetics for the1.0 nm thick shell TBP/ODA ligated particles are shown in figure 4.5. In this case, the power is sufficiently high that there is a significant probability of two photon processes. From the magnitude of the bleach signal, the average number of absorbed photons per pulse is calculated to be about 0.65, which is somewhat lower than the value calculated from the 387 nm extinction coefficient, pulse energy and beam spot size. The difference is presumably because of some saturation of the 387 nm absorption during the 120 fs excitation pulse. This power level is sufficient to observe two-photon processes, but minimizes the effects of three and greater photon absorption. At this power the ratio of probability of three-photon absorption is down by a factor of 2.8 from that of two-photon absorption. (This ratio deviates from simple Poisson statistics, because the excitation beam is attenuated as it passes through the sample.) In the high power regime, the decay kinetics become multiexponential. To extract the biexciton decay time, the fit to the low power kinetics is scaled to match the high power data at long times(>700 ps) and the difference between the two is plotted. This difference is also shown in figure 4.5 and is a measure of the absorption changes brought about by absorption of two or more photons. The difference kinetics show two components: a larger amplitude fast component which is fit to 60 ± 8 ps and a smaller amplitude 350 ps component. The 60 ps component is assigned to the lifetime of the biexciton, τ_{xx}. The magnitude of the slow component depends on the total number of photons per pulse that the entire sample absorbs. Specifically, if the excitation beam spot size and power are decreased to keep the power density constant, the magnitude of the 60 ps component is unchanged, but the magnitude of the 350 ps component decreases. Thus, the

amplitude of this component can be minimized by decreasing the excitation volume in the rapidly stirred sample. From this observation, the slow component is assigned to a photoproduct that builds up as the experiment proceeds.

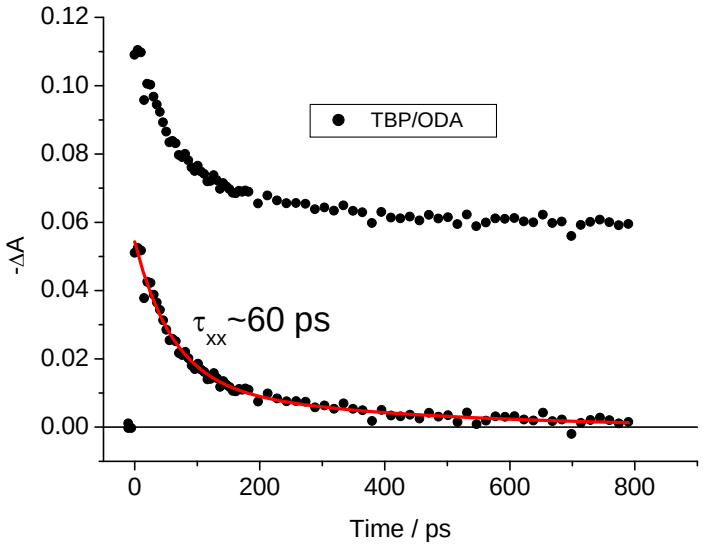

Figure 4.5. Higher power transient absorption kinetics of the lowest exciton from the thin shell (1.0 nm) CdSe/CdS core/shell particles. Also shown are kinetics that are corrected by subtracting the scaled fit to the low power kinetics. The red curve is the corresponding fit to 60 ps and smaller amplitude 350 ps components.

Similar experiments have been performed on the thicker (1.48 and 1.60 nm) shell CdSe/CdS particles, and the results are summarized in figure 4.6. Figure 4.6A shows in the low power regime for the particles having 1.48 nm thick shells. The TBP/ODA ligated particles have 16% decay of initial bleach compared to the ODA ligated particles with 21% decay. The amplitude of initial decay is less in TBP/ODA ligated particles, consistent with the higher quantum yield and smaller fraction dark fraction obtained from the PL measurements. The lifetime of this component is 218 ± 30 ps, and this is assigned to the Auger recombination time of the positive trion. Figure 4.6B shows a faster decay at higher power. The corresponding subtracted kinetics is well fit by a single exponential, giving a biexciton decay timeof83±4 ps. No longer lived components are seen in these higher power kinetics, consistent with the general observation that the thicker shell particles are more stable than thinner shell ones. Analogous plots for the 1.60 nm thick shell particles are shown in figures 4.6C and 4.6D. The thicker shell particles show somewhat longer Auger time for both trion and biexciton, 117 ps and 263 ps, respectively.

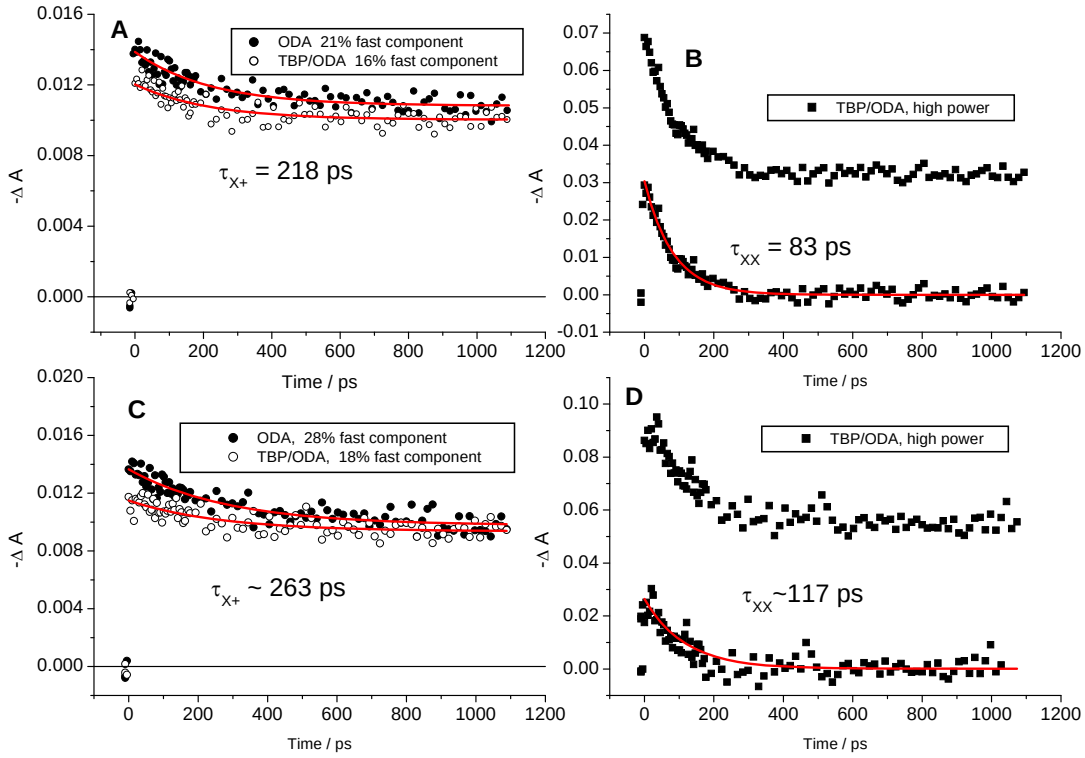

Figure 4.6. Transient absorption kinetics of lowest exciton for CdSe/CdS particles having a 1.48 nm (A and B) and 1.60 nm (C and D) thick shells. Low power kinetics with TBP/ODA and ODA ligands are shown as indicated in A and C. High power kinetics with TBP/ODA ligands and the kinetics which are corrected by subtracting the scaled fit to the low power kinetics are shown in B and D. The red curves are corresponding fits, which directly give the time constants.

4.3.3 CdSe/ZnSe core/shell particles

In addition to CdSe/CdS heterostructures, we also performed transient absorption measurements on type-I CdSe/ZnSe core/shell particles. These particles are synthesized using zincblende 2.64 nm diameter cores and are overcoated with three layers of ZnSe, for a shell thickness of about 1.0 nm. Figure 4.7 shows absorption spectra of the core and core/shell particles. Type-I heterostructures localize both electron and hole in the core, and in the case of CdSe/ZnSe, the hole confining potential is far less than that of the electron, so the extents to which the electron and hole wavefunctions spill out into the shell turn out to be about the same. This causes the electron-hole overlap to be close to unity, independent of the shell thickness. Shell deposition shifts the lowest energy exciton peak from 518 nm to 558 nm, which is considerably less than their CdSe/CdS, counterparts. The type of ligands, TBP/ODA or ODA, has little effect on the absorption spectra, or the wavelength maximum

of the PL spectrum. Just as with the CdSe/CdS particles, the PL intensities shown in figure 4.7 are sensitive to the type of ligands, with the particles having TBP exhibiting a higher quantum yield than the particle ligated with only ODA.

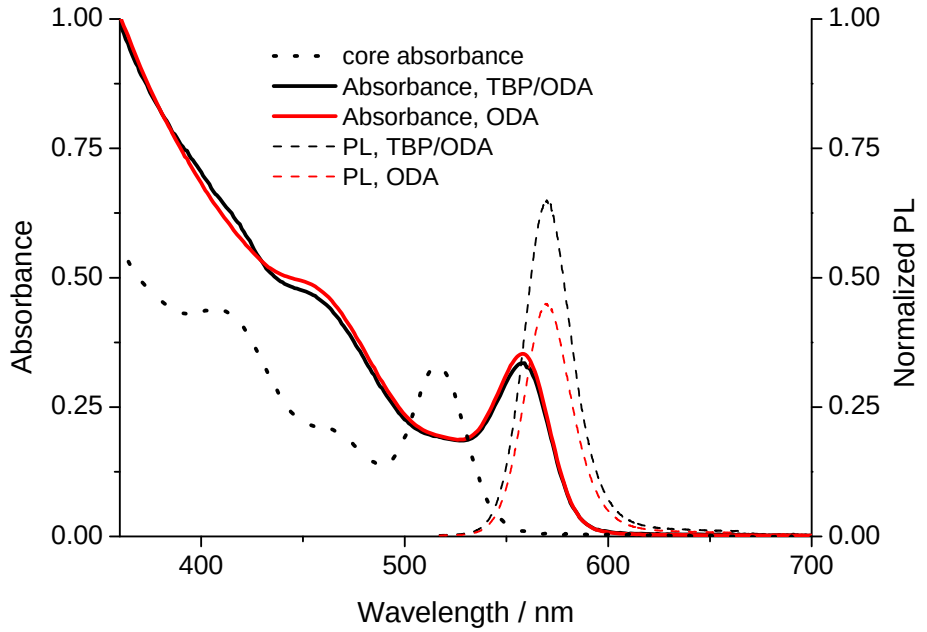

Figure 4.7. Normalized absorption spectrum of ZB CdSe core and absorption and PL spectra of CdSe/ZnSe core/shell particles. The core diameter is 2.64 nm and the shell thickness is 1.0 nm. The PL intensities are normalized such that the maximum intensity corresponds to the quantum yield.

Transient absorption kinetics of these particles are summarized in figure 4.8, and are qualitatively similar to those obtained with the CdSe/CdS particles. Figure 4.8A shows in the low power regime, particles having both types of ligands show a fast decay component, with the amplitude of this component is about twice as large in the case of the particles lacking the TBP ligands. This component is assigned to be the surface charged trion lifetime and is fit to a 48 ± 3 ps time constant. Figure 4.8B shows in the higher power kinetics, and as above, these kinetics are most accurately analyzed by subtracting off the scaled fit to the low power (one photon) decay component. The difference kinetics is fit to a biphasic decay having 22.5 ps and approximately 250 ps components. The longer component has a comparatively small amplitude, and when measured on this time scale the time constant has a large uncertainty.

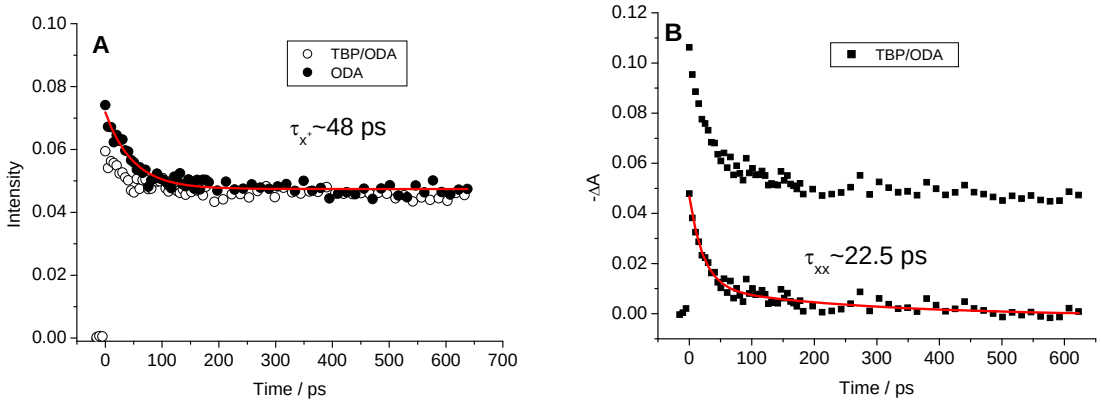

Figure 4.8. Transient absorption kinetics of lowest exciton in zincblende CdSe/ZnSe core/shell particles. (A) Low power kinetics with particles having TBP/ODA and ODA ligands. The red curve corresponds to a fit with a 48 ps single exponential decay. (B) High power kinetics obtained with particles having TBP/ODA ligands. Also shown are kinetics corrected by subtracting the scaled fit to the low power kinetics. The red curve corresponds to a biphasic decay with 22.5 and 250 ps components.

The 22.5 ps decay is assigned to the Auger recombination of the biexciton. We note that this relaxation time is slightly less than half the value obtained for the positive trion, 48 ps. As in the case of the thinner shell CdSe/CdS particles, we suspect that the slower decay component is due to buildup of negatively charged particles, consistent with equation 4.1. However, these kinetics do not allow accurate estimate of its Auger recombination time.

4.3.4 COMPARISON OF TRION AND BIEXCITON TIMES.

It is of interest to compare the trion and biexciton decay times for the particles having different CdS shell thicknesses, and to compare these values to those obtained for the CdSe/ZnSe particles. These comparisons are summarized in figure 4.9.

The figure plots the Auger times as a function of the particle "effective volume", defined as the volume of a CdSe core particle having the same lowest exciton energy as the core/shell particle. The effective volumes are derived from the absorption spectra and the same sizing curves used to determine the core sizes.[13] Garcia-Santamaria et al. have reported that the Auger recombination times scale as the product of effective volume and the inverse of electron-hole overlap, V_{eff}/S^2, where S is the electron-hole overlap integral.[68] Values of S^2 can be calculated for these particles using the methods described in chapter 2 and reference69, and range from 1.0 for the CdSe/ZnSe particles to 0.42for the CdSe/CdS particles with the thickest shells. Plots using this scaling, relations are also shown in figure 4.9. These plots assume a constant ratio of biexciton to trion Auger times, with τ_{X+}/τ_{XX} = 2.26, independent of shell thickness or composition (CdS versus ZnSe).

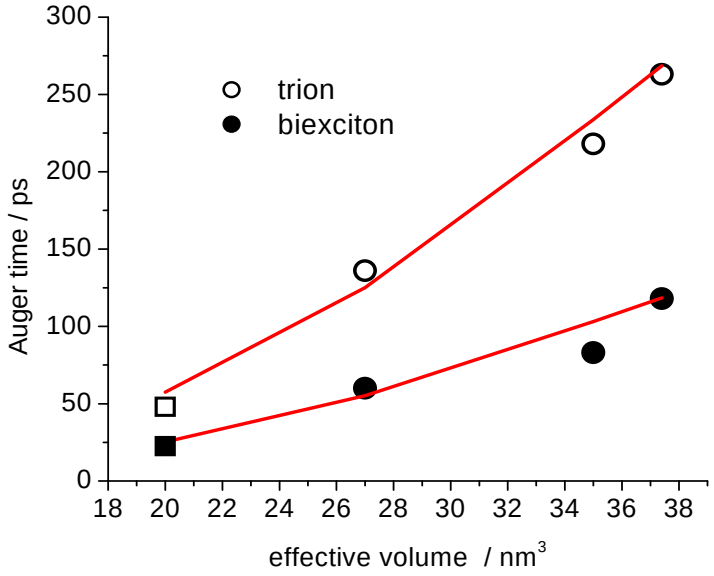

Figure 4.9. Plots of biexciton and trion Auger times as indicated for CdSe/CdS QDs (open and filled circles) and CdSe/ZnSe (open and filled squares). Also shown (red curves) are values corresponding to the V_{eff}/S^2 scaling relation, with a constant ratio of biexciton to trion Auger times, $\tau_{X+}/\tau_{XX} = 2.26$.

Two aspects of this plot are remarkable. First, the ratio of trion to biexciton Auger times is nearly constant, fit to a value of 2.26. It is well established that the fast relaxing bleach recovery component obtained at high power is due to biexciton Auger processes. We assign the fast decay component in the low power bleach recovery kinetics to a positive trion Auger process. If the later assignment were not correct (if the one-photon fast component were due to carrier trapping), then there would be no reason for this ratio to remain constant. Indeed, as the surface to volume ratio changes with shell thickness, one would expect this ratio to change, contrary to what is observed. Second, the values of both the trion and biexciton Auger times closely follow the predicted V_{eff}/S^2 scaling. It is important to note that this scaling is followed even in the comparison of particles having different shell compositions (CdS and ZnSe). It is particularly true for the ZnSe versus CdS shell comparison that if the assignment were not correct, there would be no reason for this to occur. Furthermore, since carrier trapping at the surface requires charge tunneling through the shell, one would expect these rates to vary exponentially with shell thickness, contrary to what is observed.

It is also of interest to compare these biexciton recombination times to previously reported values obtained on roughly comparable CdSe/CdS particles. Reference 68 reports experimental and calculated scaling biexciton Auger times for a series of particles having 3.0 nm wurtzite CdSe cores and several different CdS shell thicknesses. The experimentally observed biexciton times are generally greater than those calculated from the scaling relation, and this difference is assigned to effects caused by a finite alloy region at the core-shell interface. In the particles used in the present study, the shells were deposited at very low

temperature, so the core-shell interface should be very sharp. The comparison of the biexciton time for the present 1.6 nm thick shell particles (117ps) with the scaling relation curve in reference 68 for particles having the same total diameter gives an Auger time of 300 ps, in approximate agreement. The difference is partially due to the difference in core diameters; 2.64 nm for the results reported here versus 3.0 nm in reference 68. This results in slightly different electron-hole overlaps and effective volumes. When these effects are take into account through the V_{eff}/S^2 scaling relation, the 300 ps time from reference68 becomes 210 ps. Although this agreement is not quantitative, it does indicate that the same assignments to the biexciton Auger recombination can be made.

Using the above-determined ratio of Auger lifetimes for the positive trion and the biexciton (= 2.26),equation 4.1 gives a negative trion Auger time that is a factor of about 7.7 greater than that of the positive trion. There are considerable uncertainties in these Auger times, especially the trion times, so a realistic statement is the negative trion should have an Auger time that is approximately a factor of 5 – 10 greater than that of the positive trion. In the case of the 1.0 nm shell particles, this corresponds to a negative trion time that is on the order of a nanosecond. This calculation allows us to speculate that the 350 ps component observed in the high power transient absorption kinetics is due to Auger decay following photoexcitation of negatively charged particles. The slowly decaying component is seen only in the high power results because photoionization is a two-photon process.

Finally, we mention one caveat with respect o the use of equation 4.1. The equation is based solely on the relative pathway degeneracies of trion and biexciton Auger processes. It tacitly assumes that the photophysics of the trion and biexciton Auger processes are identical. However, the presence of the surface charge put the particle in a large electric field, and the presence of this field can affect the Auger dynamics. In the present case, 3.1 appears to work reasonably well, and effects of the surface charge seem to be minimal. But the present studies are performed in chloroform, which has a fairly high dielectric constant, $\varepsilon = 4.8$. This minimizes the effects of a surface charge.

4.4 CONCLUSIONS

The results presented here that show surface charging and therefore Auger dynamics play a large role in the one-photon photophysics of CdSe/CdS and CdSe/ZnSe core/shell quantum dots. Surface charging occurs when a valence band electron is thermally promoted to an unoccupied surface orbital. This occurs in the absence of photoexcitation and results in a room temperature equilibrium between surface charged and uncharged states. When an electron is in a surface orbital, the particle core is left with a positive charge – there is a hole in the valence band. Photoexcitation then produces a positive trion, which can undergo a rapid radiationless Auger recombination process. These surface charged particles are therefore dark. The extent of surface charging depends on the nature of the surface ligands. Specifically, trialkyl phosphines passivate the surface chalcogenides and thereby reduce the density of unoccupied surface orbitals. It is therefore possible to shift the equilibrium between the valence band and the surface states by controlling the surface chemistry. To study the validity of this mechanism, we have measured the positive trion and biexciton Auger times as functions of particle shell thickness and composition and of surface ligation. The measured rates can be analyzed in terms of simple scaling considerations and this analysis is consistent with the surface charging mechanism. We find the following:

- The ratio of trion to biexciton Auger rates is independent of shell thickness for CdSe/CdS, and is close to what is expected based on the degeneracies of the Auger pathways.
- The variation of trion Auger rates as a function of shell thickness for CdSe/CdS particles is accurately predicted by simple scaling relationship, V_{eff}/S^2. The same applies to the ratio of biexciton Auger rates.
- The comparison of the trion Auger rates for CdSe/ZnSe versus CdSe/CdS is also in accord with the scaling relationship, V_{eff}/S^2.

We also find that the measured biexciton Auger rates are in approximate agreement with reported values.

Overall, these results are compelling evidence that surface charging equilibrium plays a major role in QD photophysics. This has obvious implications for understanding one of the mechanisms for quantum dot fluorescence intermittency (blinking). Any given particle will, in general, have many different thermally accessible surface states and these surface states will have different energies and couplings to the valence band. Thus, we expect a wide range of equilibrium constants and charge transfer times for an isolated particle. It follows that any given particle may have a broad distribution of bright-dark transition times and this may be responsible for some of the off-on kinetics seen in single particle blinking studies. Furthermore, particles with very well passivated surfaces may exhibit suppressed blinking.[73] The same is true for core/shell particles having very uniform or thick shells, where surface charging is very slow and/or energetically uphill.[74]

CHAPTER 5.SHELL MORPHOLOGY AND LATTICE STRAIN IN CDSE/CDS CORE/SHELL QUANTUM DOT

5.1 introduction

Core/shell semiconductor quantum dots (QDs) often exhibit much higher luminescence quantum yields (QYs) and better stability than their bare-core particles. This is due the presence of the shell which effectively confines the electron and/or hole wavefunctions to the core of the particle and thereby minimizes interactions with surface defects. Electron and hole wavefunctions decay exponentially through an energetically inaccessible shell, with the result being that the wavefunction amplitude at the surface depends critically on the shell thickness. Core/shell nanocrystals are typically depicted as having a nearly spherical core and a shell of very nearly uniform thickness, which results in a very simple picture of surface passivation. However, TEM images show that this ideal situation is typically not the case. TEM images often show that the overall core/shell particles are non-spherical and have highly irregular surfaces. If the individual crystal facets are relatively large and the shell deposits uniformly on these facets, then the overall particle appears irregular in a TEM image. Alternatively, one could imagine that the core particle is very close to spherical, having many crystal facets, each of which has very small area. Following deposition of a shell having a highly non-uniform thickness would produce a core/shell particle that also appears non-spherical and irregular in a TEM image. These two situations can give similar images, but are very different in terms of the effectiveness of the shell in separating the core-confined electron or hole from the particle surface. Although this is a critical issue in determining the luminescence properties and photostability, it is very difficult to determine from TEM images how much of the apparent deviation from spherical is due to shell thickness inhomogeneity and how much is due to faceting of the core.

The extent to which the shell thickness is constant can be determined by time-resolved photoluminescence studies that measure the dynamics of hole tunneling to acceptors that are adsorbed on the shell surface.[31] Careful analysis of these hole transfer kinetics reveals the extent of shell thickness inhomogeneity. Although the analysis is complicated by the distribution of numbers of adsorbed acceptors, this can be incorporated into a model for the distribution of measured hole tunneling rates. From this analysis the distribution of shell thicknesses can be extracted from the luminescence kinetic results. Such an analysis has recently been reported for ZnTe/CdSe QDs.[31]

The shell thickness inhomogeneity in core/shell nanocrystals is quite analogous to film thickness inhomogeneity in epitaxially grown thin films. If the growth is coherent (a continuous lattice from the substrate into the film) then the nature of the film growth depends on the thermodynamic and lattice properties of the substrate and the film materials. Several growth modes can occur.[75] The usual growth modes are smooth layer-by-layer (Frank-van der Merwe, F-M), layer-by-layer up to a critical thickness and islands thereafter (Stranski-Krastanov, S-K)and island growth (Volmer-Weber, V-W). Which growth mode is observed depends on the lattice mismatch, the elastic properties of the substrate and film materials and the film surface energy. Following high temperature growth, epitaxial thin films are in a metastable thermodynamic equilibrium, with the actual equilibrium state corresponding to alloy formation. There are three relevant thermodynamic considerations in this metastable regime. First, surface roughness or island growth increases the total surface area, and therefore increases the enthalpy associated with dangling surface bonds. Second, increased surface roughness decreases the strain energy associated with the substrate/film lattice mismatch. Third, a very uniform surface has a low entropy, and may therefore be

thermodynamically unfavorable at high temperatures. The relative magnitudes of these quantities determine the film morphology that will be observed.[76] Coherent epitaxial film growth requires the coating material to adopt the in-plane lattice parameters of the immediately underlying substrate, which results in stress and strain of the film. The strain energy is the product of the forces (the stress) and the deformations (the strain). These energies can be very large, and the equilibrium film roughness depends on the relative magnitudes of the surface energy and strain energy terms. Entropy terms are smaller and involved in determining the temperature dependence of size and structure of the surface features.[75b, 76a] The magnitude of the strain energy increases with the number of film layers that grow coherently on the substrate. At the critical thickness, the increasing strain cannot be maintained and will be released through the formation of crystal defects or by island growth upon further film deposition. The critical thickness depends on the lattice mismatch, surface energy and the elastic parameters the two materials, and characterizes the difference between F-M, S-K and V-W growth.[75] Materials with a low lattice mismatch favor the two-dimensional FM growth, in which the deposited material forms a relatively smooth wetting film. Materials with a large lattice mismatch have a critical thickness of zero monolayers and adopt the three-dimensional V-W growth. In this case, formation of isolated islands directly on the substrate is followed by their growth and eventual coalescence, leading to an extremely rough surface. In the very common case that there is an intermediate lattice mismatch, epitaxial growth proceeds via the S-K model, in which formation of a uniformly strained film (the wetting layer) up to the critical thickness of monolayers is followed by the growth of three-dimensional islands on the top of the uniform film. Consequently, the surface of films that grow in S-K mode are rougher than those that grow in F-M mode, but smoother than those that grow in V-W mode.

Based on the models of epitaxial thin films, the shells of core/shell QDs can grow as either relatively uniform, smooth shells, or as shell islands. Similarly, the growth mode depends on thermodynamic and elastic parameters of the core and shell materials, specifically, the core-shell lattice mismatch and surface energy. In cases where the deposition is at sufficiently high temperature that the shell morphology corresponds to the metastable (non-alloyed) thermodynamic equilibrium, the particles will minimize the total (lattice strain plus surface) energy. When the lattice strain energy becomes too large, the shell will undergo reconstruction and/or grow as islands. There is, however, one very important difference between the substrate/film and core/shell cases: because of the semi-infinite nature of the substrate, the epitaxial film causes no change in the substrate lattice constant. In contrast, spherical core/shell particles have the strain energy distributed over the entire core/shell nanoparticle, rather than just in the film of an epitaxial substrate/film system. In the usual case where the shell has a smaller lattice parameter than the core, the lattice mismatch causes the core to be under isotropic compression and the shell to be under radial compression and tangential tension.[24, 34b77] One of the consequences of core compression is that the strain energy also depends on the core size as well as the shell thickness. The extents of the core and shell stresses and strains also depend on the shell morphology. If the shell is present as islands, then it is less coupled to the core and will remain closer to its normal lattice parameters. An incomplete or rough shell is also less capable of maintaining tangential tension and therefore less capable of compressing the core. Both of these factors cause a rough shell to have a lower lattice strain energy. Although island growth reduces the lattice strain energy, it increases the total surface area and hence

the surface energy. At thermodynamic equilibrium the particle will have a shell morphology that minimizes the sum of these energies. Uniform, coherent shell growth occurs most readily when there is little core-shell strain and hence little driving force for the shell to grow in an island morphology. Thus, uniform shells are obtained when the core is relatively small, the shell is relatively thin and the core and shell materials have close to the same lattice parameters. These trends have been previously observed, specifically, it is known that deposition of one or two ZnS monolayers on a CdSe core results in a smooth shell,[78] but further deposition results in a rough shell,[79] and a diminution of the QY.[80] Despite the smaller lattice mismatch, the same phenomena are observed for CdSe/CdS nanoparticles.[77a, 80b, 81]

In previous studies the role of lattice strain in determining the shell morphologies in ZnTe/CdSe core/shell QDs were investigated. These studies showed that the amount of lattice strain controls the shell morphology. This is an unusual core/shell system in that ZnTe and CdSe have very similar lattice constants, and one would therefore predict very little lattice strain.[82] However, annealing causes cadmium and zinc diffusion, resulting in a core/shell interface that is best described in terms of the alloys, (Zn,Cd)Te / (Cd,Zn)Se. The tellurium and selenium alloys have quite different lattice constants and the amount of lattice strain depends on the extent of metal interdiffusion. The results and analysis showed that at low levels of metal atom interdiffusion, there is little lattice strain and the shells are quite smooth. More extensive metal atom diffusion results in more lattice strain and therefore rougher shell surfaces.

In this chapter we examine the shell morphologies in CdSe/CdS core/shell QDs. The extent of shell thickness inhomogeneity is measured using the same method as our previous studies: hole acceptors are adsorbed on the particle surfaces and the inhomogeneity of luminescence quenching rates is measured. Luminescence quenching occurs as a result of charge tunneling from the particle core through the shell and the quenching kinetics give a direct measure of the tunneling rates. The hole tunneling rates are very sensitive to shell thickness and the kinetics are therefore sensitive to shell roughness. We find that deposition of CdS gives smooth shells for the smallest cores and thinnest shells. Conversely, shells with inhomogeneous thicknesses are obtained with large cores and thick shells. Specifically, we find that for any given core size, upon increasing the shell thickness, there is a specific thickness at which the extent of shell roughness undergoes a sudden increase. We also present the results of elastic continuum calculations that are used to determine the lattice strain energy as a function of core size, shell thickness and the properties of the core and shell materials. These calculations indicate that the lattice strain energy increases with core size and shell thickness. The idea that there is a critical thickness beyond which the shell becomes rough and has a high defect density is consistent with previous literature reports.[77a, 80b, 81] These calculations also facilitate the analysis of literature core/shell synthesis protocols. Finally, we find that this model breaks down if the shell is deposited at a sufficiently low temperature that it is not in thermodynamic equilibrium. To illuminate the strain limit of low temperature shell deposition, zincblende CdSe/CdSe QDs are chosen as the study system, and we demonstrate that there is an upper limit for these "metastable" particles, of which annealing process causes partial loss of core pressure as well as a red shift of the spectrum.

5.2 Experimental Section

Chemicals and optical measurements.

Details are seen in Experimental Section ofchapter2.

Synthesis of CdSe cores, CdSe/CdS core/shell nanocrystals(NCs)

The 0.1 M cadmium stock precursor solution used for the CdSe shell growth was prepared by dissolving 0.2568 g of CdO in a mixture of 2.55 ml oleic acid and 17.5 ml ODE at 250 °C. The 0.1 M selenium stock solution was prepared by dissolving 0.1580 g of Se in 5 ml TOP and 15 ml ODE. The 0.1 M sulfur stock solution was prepared by dissolving 0.032g of S in 10 ml ODE.

The syntheses of the wurtzite(WZ) CdSe core NCs are performed using a procedure previously reported and details are seen in Experimental Section in chapter 2.[5]The CdS shell deposition on CdSe core NCs is performed following the procedure reported by Embden et al.[32] The growth temperature for all sets of core/shell NCs are kept constant at 210 ~ 215 °C. The sizes of CdSe core particles are determined from the size calibration curve reported by Jasieniak et al.[13] The shell thickness of CdS is determined from the calibration curves reported by Embden et al.[32] Zincblende (ZB) CdSe core and CdSe/CdS core/shell NCs are synthesized and purified following the similar procedures reported by Nan et al. and details are seen in Experimental Section in chapter 2.[8]

Sample preparation for spectroscopy analysis

The final reaction solution is extracted by hexane/methanol (v:v~1:1) twice. The organic layer is separated and heated under vacuum to remove the residual hexane and methanol. Then, the dried sample is dissolved in ODE and ligand exchanged with excess TBP and ODA. After the ligand exchange is done, the sample is centrifuged and liquid layer is kept. The particles are precipitated by the addition of methanol, dried under vacuum, then dispersed in toluene for the spectroscopic measurements and hole quenching experiments.

Size dispersion of the core QDs may be inferred from the width of the lowest exciton absorption peak. Typical widths are 25 – 30 nm FWHM and comparable widths are obtained for the core/shell QDs. The maximum dispersion of particle sizes can be estimated from these widths and the sizing curve.[13] In this size range, this spectral width corresponds to diameters varying by about ± 10%. There are other broadening mechanisms and this represents an upper limit on the size dispersion of the particles. Other studies with comparable spectral widths have particle size dispersions of typically ± 5% to ±10%.[12-13]

Hole quenching

Samples used for the PTZ quenching studies are prepared by mixing excess PTZ dissolved in toluene with a toluene solution of the NCs. Prior to spectroscopic measurements, the samples are allowed to stirring at 60~65 °C for 10~20 minutes then cooled and allowed to sit for more than 3 hours, to ensure that the PTZ is adsorbed to the particle surfaces.

5.3 Calculation Description

In this set of calculations, the programs based on elastic continuum model and effective mass approximation coded in FORTRAN were written and modified for CdSe/CdS QDs by Professor Dave F Kelley.

Interdiffusion at the core/shell interface

Interdiffusion changes the composition of the core and shell materials and softens sharpness of the core/shell interface. In general, diffusion across a radially symmetric concentration gradient is described by a diffusion equation, $\frac{dC(r,t)}{dt} = D\nabla^2 C(r,t) = D\frac{1}{r^2}\frac{d}{dr}\left(r^2\frac{dC(r,t)}{dr}\right)$.

For the specific case that the ions isotropically interdiffuse across an initially sharp interface with a spherical particle of a radius (R), the composition function of the materials can be expressed as:[83]

$$C(r,t) = \sum_i \left[\int_0^R \rho^2 d\rho\, j_0(z_i\rho/R)\, C(\rho,0)\right] \exp\left(\frac{-D z_i^2}{R^2} t\right) j_0(z_i r/R) \qquad \text{equation. 5.1}$$

where r and ρ are radial distances, j_0 is a spherical Bessel function and z_i is the i'th zero of the j_0' and D is the radial diffusion constant. $C(\rho, 0)$ is the composition profile of the core/shell NCs before the interdiffusion. This approach amounts to expanding the initial radially dependent concentration in a Fourier-Bessel series, with each term having its own relaxation time. The sharpness of the core-shell interface is characterized by the product of the diffusion coefficient and time, D·t. With the relatively low shell deposition temperatures used here (210 °C) and no subsequent annealing, the core-shell interface is sharp and characterized by a D·t product of about 0.05.[7]

Radial and tangential stresses and strains

The radial dependent strain and stress caused by the core/shell lattice mismatch is calculated from elastic continuum theory.[34a] For the spherical core/shell NCs with a coherent interface, the interior pressures are dependent on the core size and the shell thickness, the extent of lattice mismatch, and the elastic properties of the materials. Due to the composition variation along the radial NC coordinate caused by the interdiffusion, the radially dependent pressures in the spherical NCs are calculated by a concentric method, in which the core/shell NCs are considered to be composed of n concentric shells with the shell radii given by evenly spaced values of r_i. The radially dependent displacements for the *i'th* and *i+1'th* shells in the NCs can be expressed by:[7]

$$u_i(r_i) = P_{i-1} A_{i,+} + P_i B_{i,+} \qquad \text{equation. 5.2.}$$

$$u_{i+1}(r_i) = P_i A_{i+1,-} + P_{i+1} B_{i+1,-} \qquad \text{equation. 5.3.}$$

$$A_{i,+} = \frac{r_i(1+\nu)}{E_i}\left(\frac{1-2\nu}{1+\nu} + \frac{1}{2}\right) \Bigg/ \left(\left(\frac{r_i}{r_{i-1}}\right)^3 - 1\right),$$

$$B_{i,+} = \frac{r_i(1+\nu)}{E_i}\left(\frac{1-2\nu}{1+\nu} + \frac{1}{2}\left(\frac{r_{i-1}}{r_i}\right)^3\right)\Bigg/\left(\left(\frac{r_{i-1}}{r_i}\right)^3 - 1\right),$$

$$A_{i+1,-} = \frac{r_i(1+\nu)}{E_{i+1}}\left(\frac{1-2\nu}{1+\nu} + \frac{1}{2}\left(\frac{r_{i+1}}{r_i}\right)^3\right)\Bigg/\left(\left(\frac{r_{i+1}}{r_i}\right)^3 - 1\right), \text{ and}$$

$$B_{i+1,-} = \frac{r_i(1+\nu)}{E_{i+1}}\left(\frac{1-2\nu}{1+\nu} + \frac{1}{2}\right)\Bigg/\left(\left(\frac{r_i}{r_{i+1}}\right)^3 - 1\right)$$

whereν is the Poisson' ratio, which is taken to be ~0.33.[84] This value of ν is a good approximation for the most II-VI semiconductors. In the above equations P_i is the pressure in the *i*'th shell and *E* is the Young's modulus, which is taken to scale linearly with the composition. That is, for an alloy with a composition of $CdSe_yS_{(1-y)}$, *E* is given as:

$$E = yE_{CdSe} + (1-y)E_{CdS} \qquad \text{equation.5.4}$$

The Young's modulus for the different semiconductors is given in table 5.1. In the interface region, the Young's modulus and lattice parameters are taken to vary linearly with composition, given by equation 5.1. With the boundary condition that $u_i(r_i) - u_{i+1}(r_i) = \varepsilon_{i,i+1} r_i$, where $\varepsilon_{i,i+1}$ is the difference in the lattice constants between the *i'th* and *i+1'th* shell, $\varepsilon_{i,i+1} = (x_i - x_{i+1})\varepsilon$, where ε is the total relative lattice mismatch, gives $P_{i-1} A_{i,+} + P_i (B_{i,+} - A_{i+1,-}) - P_{i+1} B_{i+1,-} = \varepsilon_{i,i+1} r_i$. Here, we may define vectors of the pressures, **P**, and lattice mismatches, **ε**. This equation may be written in terms of the matrix **D**, such that:

$$\mathbf{DP} = \boldsymbol{\varepsilon} \qquad \text{equation. 5.5}$$

where **D** is tri-diagonal: $D_{i,i-1} = A_{i,+}$, $D_{i,i} = B_{i,+} - A_{i+1,-}$, and $D_{i,i+1} = -B_{i+1,-}$. In combination with the boundary condition that the pressure at the surface of the NCs is zero, $P_n = 0$, the solution of this matrix equation gives the radially dependent pressures, P_i, for the NCs with any radial composition profile. The radial and tangential stresses are given in terms of the pressures, $\sigma_r = -P_i$, and

$$\sigma_\theta = \sigma_\varphi = \frac{P_i\left(\left(\frac{r_{i+1}}{r_i}\right)^3 + 2\right)}{2\left(\left(\frac{r_{i+1}}{r_i}\right)^3 - 1\right)} - \frac{3P_{i+1}}{2\left(1 - \left(\frac{r_i}{r_{i+1}}\right)^3\right)}$$

The radially dependent displacements, u_r, can be obtained from equation 5.2. Radial (ε_{rr}) and tangential ($\varepsilon_{\theta\theta}$ and $\varepsilon_{\varphi\varphi}$) strains are then obtained from the displacements, and are given by

$$\varepsilon_{\theta\theta} = \varepsilon_{\phi\phi} = u_r / r \quad \text{and} \quad \varepsilon_{rr} = \frac{du_r}{dr} - \frac{r}{a_0}\frac{da}{dr},$$

where *a* is the zero-pressure lattice parameter and a_0 is the lattice parameter in the core. The second term is the radial expression accounts for the change in displacement due to the radial dependence of the composition of the material and hence the zero-pressure lattice parameter. The strain energy density is then given by $E = (\sigma_r \varepsilon_r + \sigma_\theta \varepsilon_\theta + \sigma_\varphi \varepsilon_\varphi)/2$.

Table 5.1. Parameters of different bulk semiconductors used for the spectroscopic calculations in this work.

	CdS	CdSe
Lattice parameters[35a]	0.582 (ZB) 0.4135 0.6749 (W)	0.608 (ZB) 0.430 0.702 (WZ)
bulk modulus (GPa)	62.0[85]	53.0[85]
Young's modulus (GPa)	61.2[85]	67.9[85]
α (eV)	2.92[86]	2.3 [35b]
conduction band edge (V vs. NHE)	-0.4[35a, 87]	-0.30[35a]
valence band edge (V vs. NHE)	2.1[35a, 87]	1.44[35a]
electron effective mass (m_0)	0.21[88]	0.13[4a]
hole effective mass (m_0)	0.70[88]	0.45 [4a]

Conduction band potential

In semiconductor heterostructures, the strain induced pressure changes the unit cell volume, which leads to shifts in the conduction band potential. However, the calculation of the conduction band potential shift is complicated by the anisotropic nature of the strain. Specifically, one needs to consider the effects on conduction band potentials by the radial and tangential components of the strain tensor. In this case, the strain induced shifts of conduction band potentials should be given by $\Delta E = \alpha(\varepsilon_r + \varepsilon_\theta + \varepsilon_\phi)$, where ε_r, ε_θ and ε_φ are the radial, theta and phi components of the strain tensor, respectively. αis the volume dependence of the bandgap change, defined as $\alpha = -(dE_{cb} / d\ln V)$. For the NCs with a composition of $CdSe_yS_{(1-y)}$, the conduction band potential can be given by:

$$E_{cb}(r) = y(E_{cb}(CdSe) + (\varepsilon_r + \varepsilon_\theta + \varepsilon_\varphi)\alpha_{CdSe}) + (1-y)(E_{cb}(CdS) + (\varepsilon_r + \varepsilon_\theta + \varepsilon_\varphi)\alpha_{CdS}) \quad \text{equation. 5.6}$$

The α values for the CdS and CdSe are given in table 5.1. In the present case, α is taken to scale linearly with the composition, i.e, $\alpha = x\alpha_{CdSe} + (1-x)\alpha_{CdS}$, in which the lattice mismatch parameters for CdSe, CdS are given in table 5.1.

Valence band potential

The semiconductor alloys are known to have a valence band nonlinearly dependent upon their composition, a phenomenon termed "optical band bowing".[37c, 89] The band bowing greatly changes the energy gap of the semiconductor composites, and therefore has an effect on the spectroscopic properties of the NCs. The composition profile of the NCs markedly changes with the interdiffusion time and band bowing effects therefore need to be incorporated into the calculation.

The valence band potential, E_{vb}, for the NCs with the composition of $CdSe_yS_{(1-y)}$, is given by:

$$E_{vb} = yE_{vb}(\mathrm{CdSe}) + (1-y)E_{vb}(\mathrm{CdS}) + by(1-y) \quad \text{equation. 5.7}$$

where *b*is the band bowing parameter of $CdSe_yS_{(1-y)}$ and is taken to be 0.29 eV.[90] The E_{vb} values for the CdSe and CdS are given in table 5.1.

Electron and hole wave functions

The determination of the conduction and valence band profiles along the NC radial coordinate allows the calculation of the electron and hole wave functions and the spectroscopic properties of the CdSe/CdS NCs. The electron and hole wavefunctions and energetics are calculated using an effective mass approximation. However, the present case is complicated by the radially varying composition. In this case, the Schrödinger equation can be written as:[91]

$$-\frac{\hbar^2}{2}\left(\frac{1}{m^*(r)}\nabla^2\Psi+\nabla(\frac{1}{m^*(r)})\bullet\nabla\Psi\right)+V(r)\Psi=E_e\Psi \qquad \text{equation. 5.8}$$

where $m^*(r)$ is the location dependent effective mass. In the present case, the effective mass is taken to linearly change with the composition of the NCs. The electron and hole effective masses for CdS and CdSe are all given in table 5.1. Equation 5.8 is solved by expanding the wavefunctions in a series of spherical Bessel functions. The Hamiltonian is diagonalized using the conduction or valence band potential described above, giving the zero'th order electron and hole wave functions. The electron-hole coulombic interaction is then considered as a perturbation to calculate the final electron and hole wavefunctions and the exciton energies. There are several approximations and uncertainties involved in these calculations. The wavefunction and exciton energy calculations used the effective mass approximation, which has limitations that are well known. However, for these relatively large particles this is not a severe problem. Probably the biggest limitation in the accuracy of the exciton energy calculations is from the bulk material band offsets. One commonly sees literature values for the bulk material conduction and valence band energies that differ by as much as 100 mV, which is not completely insignificant compared to the band offsets. We have chosen what appear to be the most reasonable and accepted set of values (see table 5.1) and used them in a self-consistent way. By doing this, any errors enter into the calculations enter into all of them in the same way and therefore tend to offset.

Shell thickness inhomogeneity from hole transfer kinetics.

The hole transfer dynamics are inferred from the difference in the photoluminescence (PL) decay kinetics with and without an adsorbed hole acceptor, in this case phenothiazine (PTZ). The simplest case is where the shell thickness is homogeneous and all of the adsorbed acceptors have the same quenching rate. This simple situation is somewhat complicated by a Poisson distribution of adsorbed acceptors. To extract the charge transfer rate the PL decay in the absence of any PTZ is fit to a triexponential, $I(t)=\sum_{i=1}^{3}(A_i\exp(-t/\tau_i))$, where A_i and τ_i are the magnitude and the lifetime of the ith decay component in the absence of hole acceptors. Following the addition of a known concentration of PTZ, the PL decay curve is fit to equation 5.9.

$$I(t)=\sum_m P_{\langle m\rangle}(m)\,\exp(-mkt)\sum_{i=1}^{3}(A_i\exp(-t/\tau_i)) \qquad \text{equation. 5.9}$$

where k is the charge transfer rate to an individual adsorbed PTZ and there is a Poisson distribution of acceptors, having an average of $<m>$, $P_{\langle m\rangle}(m)=\frac{<m>^m}{m!}e^{-<m>}$. The assumption underlying this treatment is that the adsorbed PTZ causes charge transfer quenching, but has no other effect on the PL kinetics. Comparison of the normalized ($I_{t=0}$ = 1.0) PL decays with and without PTZ and the corresponding static PL spectra indicate that the quenching in the

integrated PL decay curve closely follows the quenching in the static PL intensity, consistent with this assumption. The concentration dependent average number of PTZs is proportional to the PTZ concentration, $\langle m \rangle = K_{ads}[PTZ]$. This "uniform thickness" model has two adjustable parameters, the tunneling rate constant, *k*, and the adsorption equilibrium constant, K_{ads}. In fitting the experimental results, these parameters are chosen to minimize the squared residuals, $R^2_{uni} = \sum \left(I_{uniform} - I_{experimental} \right)^2$, where the summation is over the experimental points in the first 100 ns of the decay curve.

Alternatively, if the shell is not uniform (i.e., the shell thickness is inhomogeneous), then each particle will have a distribution of adsorption sites corresponding to different hole transfer rates. Each of these sites may or may not be occupied by an absorbed PTZ, making the distribution of hole transfer rates more complicated. This distribution of hole transfer rates may be modeled by assuming (in addition to a Poisson distribution of numbers of adsorbed acceptors) that there a distribution of shell thicknesses. The present model assumes a very rough surface, in which there is a Poisson distribution of shell thicknesses. Such a distribution of shell thicknesses may be thought of as the opposite limiting case, compared to a completely uniform shell. Hole transfer occurs by tunneling through the shell, and the tunneling rates are a strong function of shell thickness. Wavefunction calculations indicate that this is an exponential dependence,[31b]

$$k_n = k_0 e^{-\beta n d} \qquad \text{equation. 5.10}$$

where *d* is the thickness of the monolayer (~0.35 nm for a single CdS), *n* is the number of monolayers and β is a constant. The value of β is a measure of the extent to which the hole can tunnel through the shell and is evaluated from the calculated hole wavefunction density at the surface of the particle.[31a] These calculations are described in details above, and give β = 5.4 nm^{-1}. This value is also consistent with studies on similar systems.[92] Thus, the addition of a single layer of shell material (about 0.35 nm) is expected to dramatically slow the quenching, by a factor of about 6.6. Application of this model gives

$$I(t) = I(0)\sum_{i=1}^{3}(A_i \exp(-t/\tau_i))\exp(-k_q t) \qquad \text{equation. 5.11}$$

in which equation 5.11 is evaluated with a Monte-Carlo distribution of values of the hole quenching rate, k_q. Each value of k_q is given by:

$$k_q = \sum_n m_n k_n$$

where m_n is the (randomly selected) number of the quenchers on the part of the particle having *n* monolayers and k_n is the hole quenching rate for an acceptor adsorbed on the shell having a local thickness of *n* monolayers. The hole quenching rates are taken to have an exponential dependence on shell thickness, as given by equation 5.10. Values of m_n are sampled independently from a Poisson distribution, $P_{<m>}(m) = \frac{< m >^m}{m!} e^{-<m>}$ for all $m = m_n$ having an average of $<m_n>$. As in the case of a uniform thickness shell, the averages of these *n* distributions are given by $\langle m \rangle = K_{ads}[PTZ]$. Analogous to the uniform model, this "Poisson model" also has two adjustable parameters, k_0 (in equation 5.10) and the adsorption equilibrium constant, K_{ads}. As in the case of the uniform model, these parameters are varied to minimize the residuals, $R^2_{Poisson} = \sum \left(I_{Poisson} - I_{experimental} \right)^2$. The Poisson shell thickness model gives both faster and slower components than does the uniform surface model. How

well or poorly each of these models fits the experimental results is taken to be the measure of the shell thickness inhomogeneity. This comparison is made quantitative by defining the "Poisson fraction", $PF = \frac{R_{uni}^2}{R_{Poisson}^2 + R_{uni}^2}$, with $R_{Poisson}^2$ and R_{uni}^2 defined above. Values of PF range from 0 to 1.0 as the shell becomes progressively rougher.

An assumption underlying this treatment is that the adsorbed PTZ causes charge transfer quenching, but has no other effect on the PL kinetics. Two observations support this assumption. First, the comparison of the PL decays with and without PTZ and the corresponds to the intensity of the static PL spectra. Specifically, the extent of quenching derived from the integrated, normalized ($I_{t=0}$ = 1.0) decay curve closely follows that obtained from the static PL intensities. Second, one can also consider the possibility that the presence of the PTZ can affect the shell morphology. This possibility is excluded by a simple observation: we find that the PF values are PTZ concentration independent. As the PTZ concentration is raised, the extent of hole transfer quenching increases, making the kinetics easier to analyze, but within the uncertainties of the measurements, the same PF values are extracted from the kinetics. This is not surprising; PTZ attaches to the particle surface about as strongly as other ligands, and would not be expected to result in large changes in surface energies or morphology.

5.4Results and Discussion

5.4.1 Effect of strain energy on shell morphology.

The absorption and PL of wurtzite CdSe/CdS particles having a core diameter of 2.6 nm and a shell thickness of 0.60 nm are shown in figure 5.1. Also shown in figure 5.1 are the static spectra with and without adsorbed PTZ and the corresponding PL decay curves. The presence of PTZ at a concentration of 7.5 mM quenches the luminescence by about a factor of 3, and dramatically shortens the PL decay kinetics.

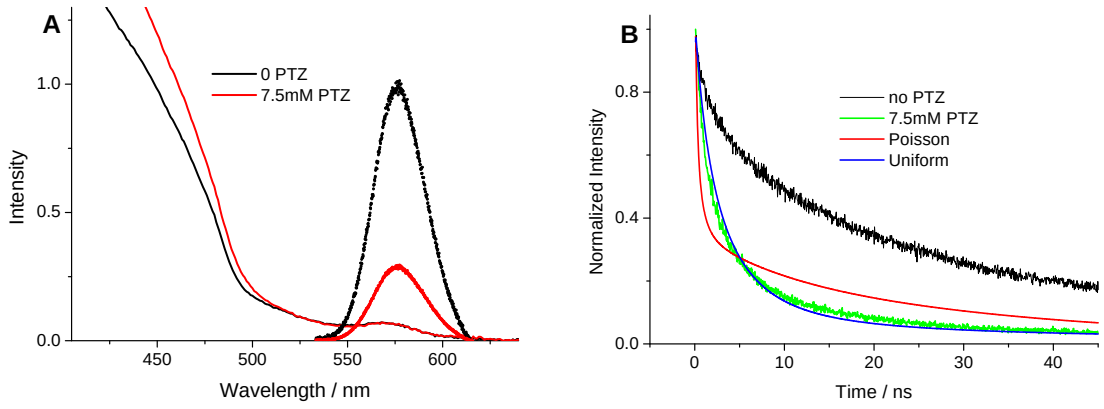

Figure 5.1. (A) Absorbance (solid curves) and PL (dotted curves); (B) PL decays of core/shell particles having a 2.60 nm diameter CdSe core with 0.60 nm CdS shell.

The fit with the uniform model is much better than with the Poisson model, indicating that the shell is relatively uniform. This is not a surprising result. In this case the core is relatively small, the shell is thin and the CdSe/CdS lattice mismatch is not very large (about -4%). All three of these considerations suggest that the extent of lattice strain and hence the total lattice strain energy is small. Thus, there is only a small lattice energy associated with minimizing the particle surface area.

A very different situation is encountered with the deposition of a slightly thicker CdS shell on a larger CdSe core, as shown in figure 5.2. In this case the larger core (4.05 nm), and the slightly thicker shell (0.51 nm) contribute to producing a larger lattice strain energy. Figure 5.2 shows that the shell morphology is better described by the Poisson shell thickness model.

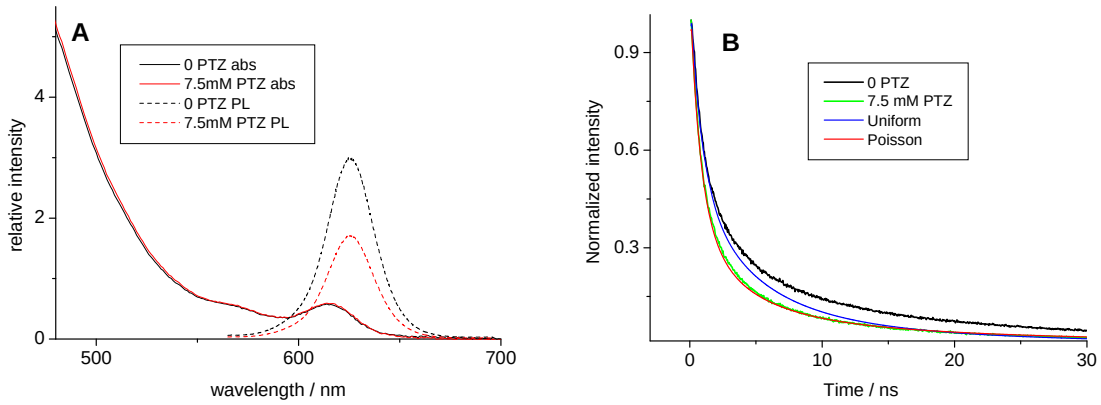

Figure 5.2. (A) Absorbance (solid curves) and PL (dotted curves); (B) PL decays of zincblende core/shell particles having a 3.9 nm diameter CdSe core with 1.0 nm CdS shell. The shell deposition was at 215 °C.

The above results along with those from several different sizes of CdSe cores and several different thicknesses of CdS shells are summarized in table 5.2. The spectra and PL decay curves for each of these particles are given in the Supplemental Material. The results in table 5.2 can be understood in terms of elastic continuum calculations. In each case, the total strain energy density is calculated as described above. The lattice strain energy is the energy density multiplied by the core surface area. Values of the total strain energy and energy density are collected in table 5.2. Figure 5.3 shows two plots of the Poisson fractions as functions of the total lattice strain energy and the lattice strain energy density (energy per core area).

Table 5.2. Core and shell dimensions, observed Poisson fraction and calculated strain energies.

Sample	core diameter (nm)	shell thickness (nm)	Poisson fraction	lattice strain energy(eV)	lattice strain energydensity (eV/nm^2)

CdSe/CdS	2.60	0.60	0.08	9.36	0.44
	2.60	1.30	0.22	12.23	0.576
	4.05	0.68	0.80	31.2	0.606
	4.05	1.35	0.75	42.5	0.824
	3.56	0.62	0.20	21.4	0.539
	3.90*	1.00	0.96	33.9	0.71
	3.90**	1.90	0.09[a]	41.9	0.877
	3.90**	0.90	0.22	32.6	0.682
	3.90**[b]	0.90	0.90	32.6	0.682

*zincblende cores, shells deposited at 210 °C.
** zincblende cores, shells deposited at 140 °C.
[a] value obtained using the same adsorption constant as the QDs with the 0.90 nm shell, see text.
[b] annealed for 20 minutes at 210 °C

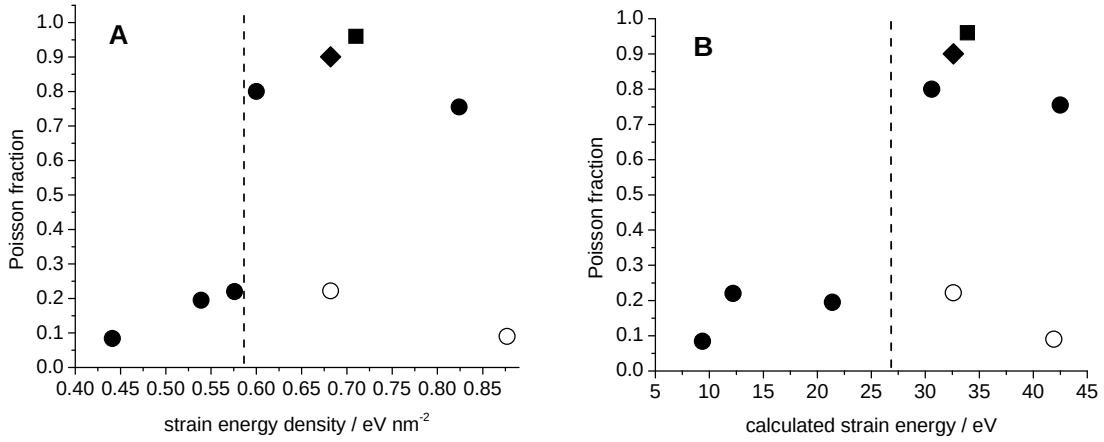

Figure 5.3. Plots of experimentally observed Poisson fraction versus (A) calculated strain energy densities, and (B) calculated total strain energies, taken from table 5.1. The symbols are as follows: wurtzite CdSe/CdS grown under normal conditions (shell growth at 210 °C), solid circles; zincblende CdSe/CdS with the shells grown at 140 °C, open circle; zincblende CdSe/CdS with the shell grown at 140 °C, and then annealed at 210 °C, solid diamond; zincblende CdSe/CdS with the shell grown at 210 °C, solid square. Also shown is are dashed lines at 0.59 eV/nm^2 and 27 eV of strain energy.

These plots show a dramatic change in the Poisson fraction when the calculated strain energy exceeds24 – 30 eV or when the calculated strain energy density exceeds 0.59 eV/nm^2. This is independent of core and shell dimensions as long as the shell is either grown or annealed at ≥210 °C. This observation indicates that the shell morphology responds in such a way as to minimize the total (surface + lattice strain) energy – it is in thermodynamic equilibrium. Both plots shown in figure 5.3 show an abrupt change in the Poisson fraction with increasing strain energy or strain energy density. The results here do not allow us to say which quantity (total strain energy or strain energy density) best describes the change in surface morphology.

Because island or defect formation initially requires a discontinuity at a specific site on the particle, we speculate that the strain energy density is a better measure of the transition. The two exceptions in table 5.2 and figure 5.3 occur when the shell is deposited at 140 °C and not subsequently annealed (indicated with open circles) and are discussed below. We also note that for the same core size and shell thickness, less quenching is associated with smooth shells. An appropriate comparison is the zincblende 3.9 nm cores with 0.9 nm shells, before and after annealing. Before annealing the shells are smooth (Poisson fraction of 0.22), and 7.5 mM PTZ gives 23% quenching. After annealing, the shells are rough (Poisson fraction of 0.90) and 7.5 mM PTZ gives 53% quenching. The difference in quenching efficiency can be qualitatively understood in terms of the exponential decrease of the hole tunneling rate with shell thickness. Rough shells will have thin sections where an adsorbed PTZ will result in very rapid quenching. These fast quenching process result in an overall greater quenching rate. This also explains why the Poisson fraction result could not be directly determined for the low temperature 3.9 nm core, 1.9 nm shell zincblende QDs. In this case, there is very little quenching (a few percent) and the small change in the decay curves makes it difficult to uniquely determine all the parameters of the both uniform and Poisson models and thereby discriminate between the models. However, we find that if the adsorption parameter (K_{ads}, above) is simply taken to be that determined for the comparable particles having a 0.9 nm shell, then a Poisson fraction value 0.09 is obtained. This is consistent with the lack of significant quenching in that both suggest that these shells are quite smooth.

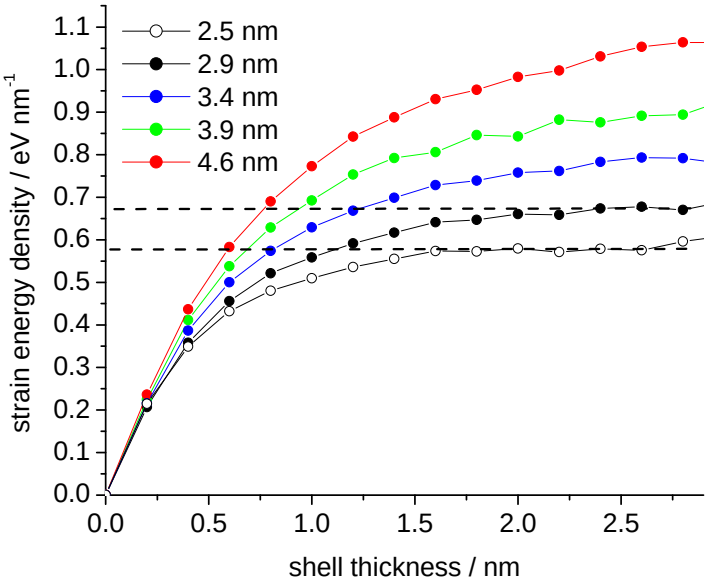

Figure 5.4. Calculated values of the strain energy density as a function of shell thickness for several different core diameters, as indicated. These calculations assume a 3.9% lattice mismatch, the CdSe/CdS elastic parameters and a sharp core/shell interface. Also indicated with dashed lines is the smooth to rough transition region.

The results of the elastic continuum calculations as functions of core size and shell thickness for a 3.9% lattice mismatch and the CdSe/CdS elastic parameters are shown in figure 5.4.

Although these curves are calculated for CdSe/CdS, they are easily adapted to understand strain energies in other II-VI core/shell QDs. This is because the strain energies in different types of core/shell QDs are very simply related: the strain energies scale as the square of the lattice mismatch. Strain energies also scale with the bulk modulus, and these elastic parameters are roughly comparable to those of the other II-VI semiconductors. These scaling can be applied to the case of CdSe/ZnS, where the lattice mismatch is about 11%, 2.9 times as large as in the CdSe/CdS case.[35a] Thus, based on this factor alone, the lattice strain energy is expected 8.4 times as large as indicated in figure 5.4. The bulk modulus of ZnS is also about 18% larger than for CdS,[93] and this factor also multiplies the strain energies. Comparison of scaled curves in figure 5.4 give very good agreement with the corresponding calculations on CdSe/ZnS QDs.

Several conclusions follow immediately from these plots in figure 5.4. When the core size is less than about 2.5 nm, the CdSe/CdS lattice strain remains below the critical value for even very thick shells. In this case the transition to a shell that is rough or has a high defect density does not occur. Figure 5.4 also shows that the calculated strain energy density at 1 monolayer (0.35 nm) is about 0.3 – 0.4 eV/nm^2, about 50 – 60% of the critical value, depending on core size. The case of a monolayer shell is at the extreme limit of the applicability of this model: an elastic continuum is a poor approximation to describe a single monolayer. One therefore needs to view this limit only semiquantitatively. With that limitation, this model predicts that when the lattice mismatch is much greater than about 5 – 6%, it becomes very difficult to grow a coherent multilayer shell. In particular, the model predicts that a monolayer shell of ZnS on a CdSe core exceeds the critical strain. This is consistent with the variation of PL quantum yield observed in CdSe/ZnS QDs. The QY of a CdSe QD is observed to increase upon deposition of a single ZnS shell, but the deposition of a second shell gives no further QY improvement, and deposition of subsequent shells decreases the QY.[80a, 94] This indicates that defect and/or island formation associated multilayer shell deposition limits the extent to which the core can be passivated with a semiconductor shell having such a large lattice mismatch.

5.4.2 TWO CAVEATS: CAN THE STRAIN BE RELIEVED? AND IS THE SHELL IN THERMAL EQUILIBRIUM?

The above model suggests that synthesizing core/shell particles having strain energy densities of more than about 0.65 eV/nm^2 may be inherently problematic. However, such particles have many technological applications and one would like to be able to overcome this limitation. There are two very different ways to do this: by relieving the strain through alloy formation or by synthesizing particles that are metastable with respect to surface restructuring.

The strain energy calculations described above assume that the core-shell interface is sharp – there is very little selenium-sulfur interdiffusion. A graded, alloyed core-shell interface can be obtained by particle annealing at high temperature and has less lattice strain than a sharp interface. Alloying from cation interdiffusion in (Cd,Zn)Se occurs at about 220 °C and proceeds rapidly above 280 °C.[95] Anions can also diffuse through II-VI semiconductor lattices, but are less mobile and require somewhat higher temperatures.[7, 50] Thus, one way to relieve lattice strain is to anneal the particles at a sufficiently high

temperature that core and shell materials interdiffuse, the same calculations indicate that forming an alloyed interface results in greatly reduced lattice strain. Consistent with these calculations, previous reports have shown that several sizes of CdSe/CdS particles annealed at 310 °C for 60 minutes are quite uniform and have high quantum yields.[73a]

A critical assumption of the above model is that the shell morphology corresponds to the minimum energy configuration – the system is in equilibrium. This may not be the case if the shell is deposited at a sufficiently low temperature. In this case, shell deposition starts out coherent and continues to remain coherent to thicknesses that where the strain energy exceeds the amount needed to favor rough shell growth. The smooth to rough surface reconstruction or even defect formation requires the concerted motion of many different surface atoms, and is therefore a strongly activated process. At the usual (relatively high) shell deposition temperatures this transition readily occurs and the shell morphology changes to relieve the strain. Consistent with this, literature reports of most thick shelled CdSe/CdS particles indicate that the PL quantum yield decreases with increasing shell thickness, consistent with the results presented above. However, at low temperature there may be insufficient thermal energy to overcome the smooth to rough activation barrier even when the shell becomes sufficiently thick for this to be energetically favorable. As a result, continued shell deposition can result in a metastable shell having very high lattice strain energy, but very few defects. Although such a shell is metastable with respect to defect formation, the lack of defects may result in high luminescence QYs and excellent optical properties. Nan et al.[8] have recently reported the synthesis and optical properties of zincblende CdSe/CdS core/shell particles in which the shells are deposited at very low temperatures, less than 160 ºC. This is done using thermal cycling method and a single source CdS precursor that decomposes at low temperature. They report excellent optical properties and very high luminescence QYs. We have synthesized similar zincblende cores and subsequently deposited 1.0 or 0.90 nm thick CdS shells at either the normal high temperature (210 ºC), or at low temperature (140 °C), as described in reference 8. High temperature shell deposition gives results that are quite similar to those obtained with wurtzite cores. For these core and shell dimensions, the calculated lattice strain energy is about 0.7 eV/nm^2 (see table 5.2 and figure 5.3), which is greater than the observed roughening threshold of about 0.59 eV/nm^2. When the shells are grown at 210 °C, addition of PTZ results in considerable quenching (52% for 7.5 mM PTZ) and the decays are best fit with the Poisson model (see figure 5.3). We conclude that the shells are rough.

The shells deposited at low temperature provide exceptions to the predictions of this model. In the case using the same zincblende cores and low temperature shell deposition, the shell thickness is comparable and calculated strain energy is 32.6 eV. However, these particles show relatively little quenching (22%) upon the addition of 7.5 mM PTZ. The decay for the low temperature deposition shells is much better fit with a uniform model, and we obtain a Poisson fraction of 0.22. The conclusion is that despite the large strain energy, the shells deposited at low temperature remain smooth and do not relax to a rough morphology. Particles with thicker shells (1.90 nm) deposited at low temperature correspond to much larger strain energies (41.9 eV), but as discussed above, show only a few percent quenching even at very high PTZ concentrations (50 mM), and give a Poisson ratio consistent with smooth shells. Also consistent with the idea that the thicker shell QDs have very uniform, close to defect free shells, we find that these QDs are very stable and have luminescence QYs of about 95%. The lack of defects seems to be unique to the zincblende

crystal structure. We find that analogous low-temperature shell deposition on wurtzite cores give much lower luminescence QYs, consistent with the original reports.[8]

A further experiment is to anneal the zincblende particles having 0.90 nm thick shells at the normal shell deposition temperature (210 °C). This is comparable to the normal shell deposition temperature, but is too low to cause significant radial diffusion of the seleniums or sulfurs. The calculated strain energy density is greater than the 0.59 eV/nm^2 needed to cause relaxation to a rough surface morphology. As expected, annealing results in a much rougher shell, as indicated by the increased amount of quenching and the much larger Poisson fraction (see table 5.1 and figure 5.3). This indicates that prior to this low temperature annealing, there is a very large amount of lattice strain energy and that the shells are not in thermodynamic equilibrium. Annealing at 210 °C is sufficient to cause relaxation to the energetically favored shell morphology.

5.4.3 Lattice strain limit in zincblende CdSe/CdS core/shell QDs.

In previous paragraph, we suggest two ways to put on thicker shells without degrading the optical properties and lowering the PL QY.[96] One way to do this is to diminish the lattice strain by synthesizing particles having an alloyed core/shell interface. High temperature annealing causes interdiffusion of the core and shell materials creating an alloy region. The presence of an alloy region with the core continuously changing to the shell greatly reduces the extent of the lattice strain. If the alloy region is sufficiently broad then in principle, any thickness of shell can be deposited without exceeding the critical strain energy density. Very high quantum yield particles can be obtained using this approach.[73a] The practical limitation associated with doing this is that annealing can also result in particle ripening, which increases the inhomogeneity. The other approach to limit the extent to which lattice strain degrades the optical properties of core/shell QDs is to synthesize particles that are not in thermodynamic equilibrium. This can be accomplished by depositing the shell at a sufficiently low temperature that the equilibrium (irregular) morphology is not achieved. Nan et al.[8] have recently reported the synthesis and optical properties of zincblende (ZB) CdSe/CdS core/shell particles in which the shells are deposited at very low temperatures (~140 °C). They report excellent optical properties and very high PL QYs for very thick shell growth, i.e. 85% for 2~4 CdS monolayers (ML) and >50% for 8~10 CdS ML. In the present studies and consistent with what is reported in reference 8, we find that this synthetic methodology yields higher quantum yield zincblende QDs, compared to when it is applied to their wurtzite counterparts. (Wurtzite CdSe/CdS QD having high QYs are typically synthesized or annealed at temperatures above 210 °C.) The low temperature does not give sufficient thermal energy to overcome the smooth to rough activation barrier when the shell becomes sufficiently thick for this to be energetically favorable. Therefore, continued shell deposition can result in a metastable shell having smooth shell surface with very few defects, but very high lattice strain energy. This approach does, however, have its limitations. At some shell thickness, the lattice strain energy becomes sufficiently large that it will not maintain the smooth-shell metastable state. Otherwise stated, there is a limit to the thickness of shell that can be deposited, even at the lower temperature. To understanding these limiting conditions, the effects of lattice strain on the spectroscopy and photoluminescence QYs of zincblende CdSe/CdS core/shell quantum dots are examined.

The results reported here elucidate the maximum thickness that can be obtained while keeping the shell surface relatively uniform. This is done by depositing CdS shells of increasing thickness on various sizes of CdSe cores and examining the PL QY as a function of shell thickness. The PL QYs of CdSe/CdS core/shell particles with several different sizes of zincblende CdSe cores and different CdS shell thicknesses are summarized in figure 5.5A.

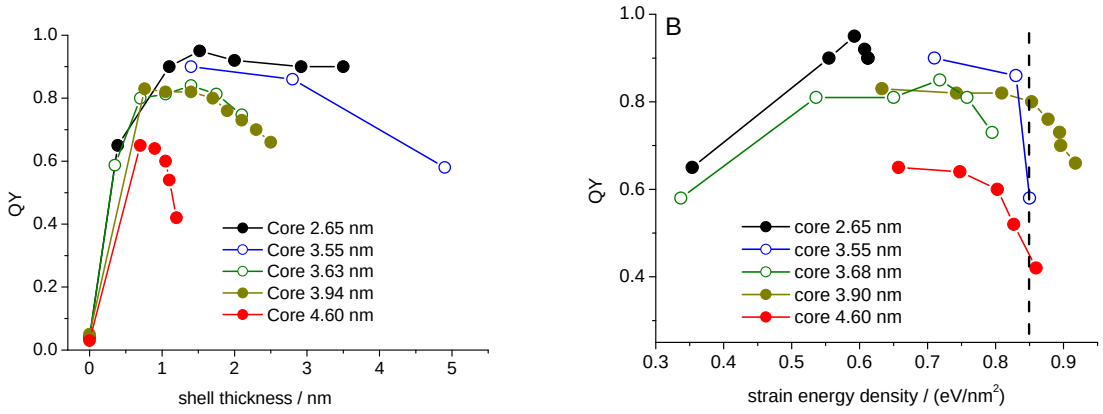

Figure 5.5.Comparison of QY as a function of (A) CdS shell thickness, and (B) calculated strain energy density for different CdSe core sizes, as indicated. The vertical dashed line in (B) corresponds to a strain energy density of 0.85 eV/nm^2. The points for the 3.63 nm core are extracted from the data of Nan et al.[8] and the points for the 3.55 nm cores are from Qin et al.[74b]

Some of the results (open circles) in figure 5.5 come from the analysis of data reported by Nan et al.[8] and Qin et al.[74b] Sizing maps (exciton energy as a function of core size and shell thickness) vary slightly from one report to another. We have analyzed all of the spectroscopic data using sizing map reported in chapter 2. This results in slightly different sizes and shell thickness than originally reported, but ensures self-consistency throughout the results. A CdS monolayer (ML) shell corresponds to about 0.33 nm, and the figure shows that the QY increases dramatically upon deposition of 1 – 2 MLs of CdS. Lattice strain is minimal with such a thin shell and we conclude that 1 – 2 CdS MLs are needed to passivate the defects on the surface of the CdSe core. Two other trends are also apparent. First, higher maximum QYs are achieved with smaller cores, and second, particles having smaller cores maintain high QYs with much thicker shells. We suspect that the first trend is simply a surface area effect. The larger core has more surface area, and therefore a higher probability of surface defects that are not well passivated. The loss of quantum yield with the thickest shells is assigned to a lattice strain effect. This effect can be quantitatively understood in terms of elastic continuum calculations, where the total lattice strain energy is calculated as a function of core size, shell thickness and the properties of the core and shell materials, as described in references96, 31a, 31b and 7.The core (rather than the shell) surface area is most relevant because the elastic strain is concentrated at the core-shell interface.

This model assumes that the core and shell have the elastic properties of bulk CdSe and CdS, respectively, and that the crystal structure is continuous across the sharp core-shell interface, i.e., the interface is coherent. Figure 5.5B shows the same data as figure 5.5A, except plotted as a function of the calculated lattice strain energy density (lattice strain energy divided by core surface area). By plotting the QYs as a function of the calculated strain energy density, figure 5.5B shows that the QY drop-off at the larger shell thicknesses occurs when the strain energy density exceeds a specific maximum value, about 0.85 eV/nm^2. As mentioned earlier, CdSe/CdS particles are stable with respect to shell defect formation below a strain energy density of about 0.59 eV/nm^2. So this range, 0.59 to 0.85 eV/nm^2, defines the core/shell morphologies that can maintain smooth, relatively defect free surfaces, despite being thermodynamically unstable. The range of core sizes and shell thicknesses that fall into each of the categories of stable, metastable and unstable are shown in figure 5.6, in terms of lowest exciton absorption wavelength. The exciton wavelengths corresponding to different core sizes and shell thickness are similar to other recently reported sizing "maps",[32, 69] and were calculated is the same way as the zincblende core/shell map in reference 69.

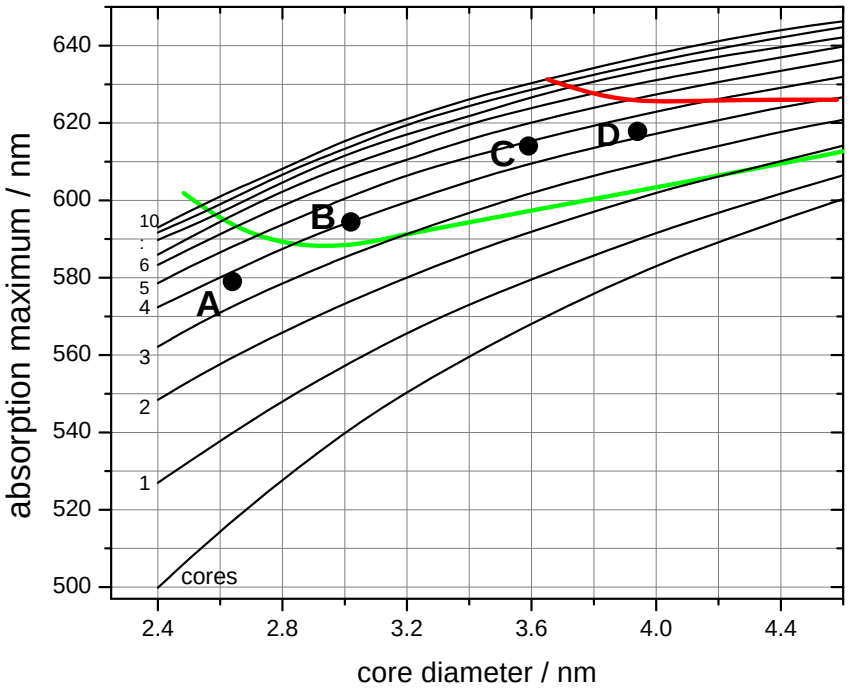

Figure 5.6. Absorption maximum (nm) of lowest exciton of zincblende CdSe/CdS core/shell particles as a function of CdSe core sizes and CdS shell thickness (monolayers). The green and red lines correspond to strain energy densities of 0.59 and 0.85 eV/nm^2, defining the stable/metastable and metastable/unstable boundaries, respectively. Points labeled A, B, C and D indicate samples for which annealing spectral shifts were measured. The region between these lines corresponds to core/shell particles that are smooth, but metastable with respect to defect formation.

Particles with dimensions falling below the green line in figure 5.6 can have high QYs and smooth surfaces that are thermodynamically stable. The maximum shell thickness for which stability is maintained varies with core size. It is of interest to note that cores having diameters less than about 2.5 nm can support very thick, bulk-like CdS shells. In this case the energy needed to compress the core to a lattice parameter that it is compatible with being embedded in the lattice of the CdS shell is less than the energy needed to produce shell defects. In contrast, particles with dimensions falling above the red line have sufficiently high strain energies that defect formation will spontaneously occur, even at low shell deposition temperature, < 140 °C. The set of wavelength curves in the figure 5.6 map were calculated assuming that the core-shell interface is coherent. However, the region above the red line in figure 5.6 represents core/shell particles for which smooth shells and a coherent core/shell interface is unstable. Strain release will cause at least partial reduction in the pressure of the particle core. Core compression causes a significant blue shift spectrum and its loss at the metastable/unstable boundary results in a discontinuity in the lowest exciton absorption wavelength. Thus, for core/shell particles above the red line in figure 5.6, the interpretation of wavelengths in this map must be viewed cautiously.

Shell deposition producing core/shell particles in the intermediate regime can be accomplished at low temperatures, and these particles can have very high PL QYs and extremely good optical characteristics. However, these optical properties will be lost if the particles are annealed at a sufficiently high temperature that thermodynamic equilibrium is reached, > 210 °C. Associated with relaxation to thermodynamic equilibrium is the partial loss of core compression. The bulk CdSe bandgap is pressure dependent, $\frac{dE_{gap}}{dP} = 4.5\ meV / kbar$.[35b] Thus, the release of the strain energy results in the absorption spectrum shifting to longer wavelengths. Table 5.3 gives the observed spectral shifts following 15~20 minutes of annealing at 210 °C for the core/shell particles indicated in figure 5.6.

Table 5.3. Spectroscopic and annealing results for stable and metastable particles.

sample	core[a]	shell[a]	λ / nm	energy density[b]	Δλ /nm (obs.)	Δλ /nm (equilib.)[c]	Δλ /nm (relaxed)[c]
A	2.65	1.20	578.9	0.57	-2.0	0.0	0.0
B	3.02	1.31	594.4	0.66	+4.1	+0.6	+7.5
C	3.59	1.59	614.0	0.78	+4.1	+1.8	+7.9
D	3.94	1.40	617.8	0.82	+3.0	+2.4	+9.1

[a]core diameters and shell thicknesses are in nm.
[b] eV/nm^2.
[c] Calculated wavelength shifts for complete release of lattice strain (relaxed) and release to the 0.59 eV/nm^2 thermodynamic maximum (equilibrium).

Sample A is in the stable regime, and shows only a slight blue shift upon annealing. This is due to an etching effect and a blue shift of this magnitude often occurs upon annealing. In contrast, samples B, C and D are in the metastable region and show the opposite behavior, despite the possibility of etching. A significant red shift upon annealing occurs, due to the release of pressure on the core. Table 5.3 also gives the calculated red shift assuming that all of lattice strain is removed and assuming that the lattice strain energy is diminished to the maximum equilibrium value of 0.59 eV/nm^2. The observed values fall between these two extremes, indicating that following strain relaxation, there is still considerable core pressure, but less than the thermodynamic limiting value. This observation indicates that the short, 210 °C annealing is sufficient to relax the coherency of the shell, but does not cause the shell to reach equilibrium. We also not that the results in reference 97 showed that annealing of metastable particles allowed surface adsorbates to get closer to the core. Based on the combination of these results, we speculate annealing under these conditions results in the production of many shell defects, but not a complete change in shell morphology or crystal structure.

5.5 Conclusions

The experimental results and computational model reported here lead to a few very simple conclusions about the morphology of core/shell QDs. The results show that smooth shell growth is thermodynamically favored during the initial deposition of CdS shell on a CdSe core. As shell deposition proceeds the lattice strain energy increases. At some point, depending on the core size and shell thickness, the strain energy density becomes sufficiently great (27 eV or 0.59 eV/nm^2) that the shell undergoes reconstruction to a higher surface area, lower strain morphology. This typically creates defects and thereby lowers the luminescence QY. Shell reconstruction is an activated process and if the shell is deposited at a sufficiently low temperature, much higher strain energies will be obtained before the shell undergoes reconstruction. This is desirable for making well passivated, highly luminescent CdSe/CdS particles.

High quantum yields of zincblende CdSe/CdS quantum dots are achieved as long as the lattice strain energy density is below about 0.85 eV/nm^2, which is considerably greater than the limiting value of 0.59 eV/nm^{2}for thermodynamicstability of a smooth, defect free shell, as previously reported in chapter 2 and previous work.[97] Thus, core/shell quantum dots having strain energy densities between 0.59 and 0.85 eV/nm^2 can have very high PL QYs, but are metastable with respect to surface defect formation. Such metastable core/shell QDs can be produced by shell deposition at comparatively low temperatures (< 140 °C).Annealing of these particles causes partial loss of core pressure, and a red shift of the spectrum.

BIBLIOGRAPHY

1. (a) Strickler, S. J.; Berg, R. A., Relationship between Absorption Intensity and Fluorescence Lifetime of Molecules. *J. Chem. Phys.* **1962,***37*, 814 - 822;(b) Birks, J. B.; Dyson, D. J., The Relations Between the Fluorescence and Absorption Properties of Organic Molecules. *Proc. R. Soc. Lond. A* **1963,***275*, 135 - 148;(c) Kelley, A. M., *Condensed-Phase Molecular Spectroscopy and Photophysics*. Wiley: Hoboken, NJ, 2013.
2. Kamal, J. S.; Gomes, R.; Hens, Z.; Karvar, M.; Neyts, K.; Compernolle, S.; Vanhaecke, F., Direct determination of absorption anisotropy in colloidal quantum rods. *Phys. Rev. B* **2012,***85*, 35126 - 35132.
3. (a) Califano, M.; Franceschetti, A.; Zunger, A., Temperature Dependence of Excitonic Radiative Decay in CdSe Quantum Dots: The Role of Surface Hole Traps. *Nano Lett.* **2005,***5*, 2360 - 2364;(b) An, J. M.; Franceschetti, A.; Zunger, A., The Excitonic Exchange Splitting and Radiative Lifetime in PbSe Quantum Dots. *Nano Lett.* **2007,***7*, 2129 - 2135.
4. (a) Efros, A. L.; Rosen, M.; Kuno, M.; Nirmal, M.; Norris, D. J.; Bawendi, M., Band-Edge Exciton in Quantum Dots of Semiconductors With a Degenerate Valence Band: Dark and Bright Exciton States. *Phys. Rev. B* **1996,***54*, 4843 - 4856;(b) Moreels, I.; Raino, G.; Gomes, R.; Hens, Z.; Stoferle, T.; Mahrt, R. F., Band-Edge Exciton Fine Structure of Small, Nearly Spherical Colloidal CdSe/ZnS Quantum Dots. *ACS Nano* **2011,***5*, 8033 - 8039.
5. Gong, K.; Zeng, Y.; Kelley, D. F., Extinction Coefficients, Oscillator Strengths, and Radiative Lifetimes of CdSe, CdTe, and CdTe/CdSe Nanocrystals. *J. Phys. Chem. C* **2013,***117*, 20268-20279.
6. Efros, A. L.; Rosen, M., Quantum Size Level Structure of Narrow-Gap Semiconductor Nanocrystals: Effect of Band Coupling. *Phys. Rev. B* **1998,***58*, 7120 - 7135.
7. Cai, X.; Mirafzal, H.; Nguyen, K.; Leppert, V.; Kelley, D. F., The Spectroscopy of CdTe/CdSe type-II Nanostructures: Morphology, Lattice Mismatch and Band-Bowing Effects. *J. Phys. Chem. C* **2012,***116*, 8118 - 8127.
8. Nan, W.; Niu, Y.; Qin, H.; Cui, F.; Yang, Y.; Lai, R.; Lin, W.; Peng, X., Crystal Structure Control of Zinc-Blende CdSe/CdS Core/Shell Nanocrystals: Synthesis and Structure-Dependent Optical Properties. *J. Am. Chem. Soc.* **2012,***134*, 19685−19693.
9. Qu, L.; Peng, X., Control of Photoluminescence Properties of CdSe Nanocrystals in Growth. *J. Am. Chem. Soc.* **2002,***124*, 2049 - 2055.
10. (a) Reiss, P.; Bleuse, J.; Pron, A., Highly Luminescent CdSe/ZnSe Core/Shell Nanocrystals of Low Size Dispersion. *Nano Lett.* **2002,***2*, 781–784;(b) Reiss, P.; Carayon, S.; Bleuse, J., Large fluorescence quantum yield and low size dispersion from CdSe/ZnSe core/shell nanocrystals. *Physica E* **2003,***17*, 95 - 96.
11. Leatherdale, C. A.; Woo, W.-K.; Mikulec, F. V.; Bawendi, M. G., On the Absorption Cross Section of CdSe Nanocrystal Quantum Dots *J. Phys. Chem. B.* **2002,***106*, 7619 - 7622.
12. Yu, W. W.; Qu, L.; Guo, W.; Peng, X., Experimental Determination of the Extinction Coefficient of CdTe, CdSe, and CdS Nanocrystals. *Chem. Mater.* **2003,***15*, 2854 - 2860.
13. Jasieniak, J.; Smith, L.; van Embden, J.; Mulvaney, P.; Califano, M., Re-examination of the Size-Dependent Absorption Properties of CdSe Quantum Dots. *J. Phys. Chem. C* **2009,***113*, 19468 - 19474.

14. Capek, R. K.; Moreels, I.; Lambert, K.; Muynck, D. D.; Zhao, Q.; Tomme, A. V.; Vanhaecke, F.; Hens, Z., Optical Properties of Zincblende Cadmium Selenide Quantum Dots. *J. Phys. Chem. C* **2010,***114*, 6371 - 6376.
15. de Mello Donega, C.; Koole, R., Size Dependence of the Spontaneous Emission Rate and Absorption Cross Section of CdSe and CdTe Quantum Dots. *J. Phys. Chem. C* **2009,***113*, 6511 - 6520.
16. Kim, J.; Wong, C. Y.; Nair, P. S.; Fritz, K. P.; Kumar, S.; Scholes, G. D., Mechanism and Origin of Exciton Spin Relaxation in CdSe Nanorods. *J. Phys. Chem. B* **2006,***110*, 25371 - 25382.
17. van Driel, A. F.; Allan, G.; Delerue, C.; Lodahl, P.; Vos, W. L.; Vanmaekelbergh, D., Frequency-Dependent Spontaneous Emission Rate from CdSe and CdTe Nanocrystals: Influence of Dark States. *Phys. Rev. Lett.* **2005,***95*, 236804
18. Leistikow, M. D.; Johansen, J.; Kettelarij, A. J.; Lodahl, P.; Vos, W. L., Size-dependent oscillator strength and quantum efficiency of CdSe quantum dots controlled via the local density of states. *Phys. Rev. B* **2009,***79*, 45301 - 45309.
19. Crooker, S. A.; Barrick, T.; Hollingsworth, J. A.; Klimov, V. I., Multiple temperature regimes of radiative decay in CdSe nanocrystal quantum dots: Intrinsic limits to the dark-exciton lifetime. *App. Phys. Lett.* **2003,***82*, 2793 - 2795.
20. Jiang, Z.-J.; Kelley, D. F., Surface Charge and Piezoelectric Fields Control Auger Recombination in Semiconductor Nanocrystals. *Nano Lett.* **2011,***11*, 4067 - 4073.
21. Kamal, J. S.; Omari, A.; Hoecke, K. V.; Zhao, Q.; Vantomme, A.; Vanhaecke, F.; Capek, R. K.; Hens, Z., Size-Dependent Optical Properties of Zinc Blende Cadmium Telluride Quantum Dots. *J. Phys. Chem. C* **2012,***116*, 5049 - 5054.
22. Groeneveld, E.; Delerue, C.; Allan, G.; Niquet, Y.-M.; Donegá, C. d. M., Size Dependence of the Exciton Transitions in Colloidal CdTe Quantum Dots. *J. Phys. Chem. C* **2012,***116*, 23160 - 23167.
23. (a) Kim, S.; Fisher, B.; Eisler, H.-J.; Bawendi, M. G., Type-II Quantum Dots: CdTe/CdSe(Core/Shell) and CdSe/ZnTe(Core/Shell) Heterostructures. *J. Am. Chem. Soc.* **2003,***125*, 11466 - 11467;(b) Chin, P. T. K.; Donega, C. d. M.; Bavel, S. S. v.; Meskers, S. C. J.; Sommerdijk, N. A. J. M.; Janssen, R. A. J., Highly Luminescent CdTe/CdSe Colloidal Heteronanocrystals with Temperature-Dependent Emission Color. *J. Am. Chem. Soc.* **2007,***129*, 14880 - 14886.
24. Smith, A. M.; Mohs, A. M.; Nie, S., Tuning the Optical and Electronic Properties of Colloidal Nanocrystals by Lattice Strain. *Nature Nanotechnology* **2009,***4*, 56 - 63.
25. de Mello Donegá, C., Formation of nanoscale spatially indirect excitons: Evolution of the type-II optical character of CdTe/CdSe heteronanocrystals. *Physical Review B* **2010,***81*, 165303 - 165323.
26. Ma, X.; Mews, A.; Kipp, T., Determination of Electronic Energy Levels in Type-II CdTe-Core/CdSe-Shell and CdSe-Core/CdTe-Shell Nanocrystals by Cyclic Voltammetry and Optical Spectroscopy. *J. Phys. Chem. C* **2013,***117*, 16698 - 16708.
27. (a) Chuang, C.-H.; Lo, S. S.; Scholes, G. D.; Burda, C., Charge Separation and Recombination in CdTe/CdSe Core/Shell Nanocrystals as a Function of Shell Coverage: Probing the Onset of the Quasi Type-II Regime. *J. Phys. Chem. Lett.* **2010,***1*, 2530 - 2535;(b) Chuang, C.-H.; Doane, T. L.; Lo, S. S.; Scholes, G. D.; Burda, C., Measuring Electron and Hole Transfer in Core/Shell Nanoheterostructures. *ACS Nano* **2011,***5* (7), 6016 - 6024;(c)

Kumar, S.; Jones, M.; Lo, S. S.; Scholes, G. D., Nanorod Heterostructures Showing Photoinduced Charge Separation. *Small* **2007,***3*, 1633 - 1639.
28. Brus, L. E., Electron–electron and electron-hole interactions in small semiconductor crystallites: The size dependence of the lowest excited electronic state. *J. Chem. Phys.* **1984,***80*, 4403 - 4409.
29. (a) Rogach, A. L.; Kornowski, A.; Gao, M.; Eychmuller, A.; Weller, H., Synthesis and Characterization of a Size Series of Extremely Small Thiol-Stabilized CdSe Nanocrystals. *J. Phys. Chem. B* **1999,***103*, 3065 - 3069;(b) Masumoto, Y.; Sonobe, K., Size-dependent energy levels of CdTe quantum dots. *Phys. Rev. B* **1997,***56*, 9734 - 9737.
30. Cai, X.; Martin, J. E.; Shea-Rohwer, L. E.; Gong, K.; Kelley, D. F., Thermal Quenching Mechanisms in II-VI Semiconductor Nanocrystals. *J. Phys. Chem. C* **2013,***117*, 7902 - 7913.
31. (a) Jiang, Z.-J.; Kelley, D. F., Effects of Inhomogeneous Shell Thickness in the Charge Transfer Dynamics of ZnTe/CdSe Nanocrystals. *J. Phys. Chem. C* **2012,***116*, 12958 - 12968;(b) Jiang, Z.-J.; Kelley, D. F., Stranski-Krastanov Shell Growth in ZnTe/CdSe Core/Shell Nanocrystals. *J. Phys. Chem. C* **2013,***117*, 6826 - 6834.
32. van Embden, J.; Jasieniak, J.; Mulvaney, P., Mapping the Optical Properties of CdSe/CdS Heterostructure Nanocrystals: The Effects of Core Size and Shell Thickness. *J. Am. Chem. Soc.* **2009,***131*, 14299 - 14309.
33. (a) Yu, P. Y.; Cardona, M., *Fundamentals of Semiconductors*. third ed.; Springer: Berlin, 2001;(b) Norris, D. J., Electronic Structure in Semiconductor Nanocrystals: Optical Experiment. In *Nanocrystal Quantum Dots*, 2'd ed.; Klimov, V. I., Ed. CRC Press: 2010.
34. (a) Saada, A. S., *Elasticity Theory and Applications*. Permagon Press: New York, 1974;(b) Rockenberger, J.; Troger, L.; Rogach, A. L.; Tischer, M.; Grundmann, M.; Eychmuller, A.; Weller, H., The Contribution of Particle Core and Surface to Strain, Disorder and Vibrations in Thiol-Capped CdTe Nanocrystals. *J. Chem. Phys.* **1998,***108* (18), 7807-7815.
35. (a) West, A. R., *Basic Solid State Chemistry*. Wiley Chichester, 1988;(b) Shan, W.; Walukiewicz, W.; Ager, J. W., III; Yu, K. M.; Wu, J.; Haller, E. E., Pressure Dependence of the Fundamental Band-gap Energy of CdSe. *Appl. Phys. Lett.* **2004,***84* (1), 67-69;(c) San-Miguel, A.; Polian, A.; Itie, J. P.; Marbuef, A.; Triboulet, R., Zinc Telluride Under High Pressure: An X-Ray Absorption Study. *High Pressure Research* **1992,***10*, 412 - 415.
36. (a) Talapin, D. V.; Koeppe, R.; Gtzinger, S.; Kornowski, A.; Lupton, J. M.; Rogach, A. L.; Benson, O.; Feldmann, J.; Weller, H., Highly Emissive Colloidal CdSe/CdS Heterostructures of Mixed Dimensionality. *Nano Letters* **2003,***3*, 1677 - 1681;(b) Steiner, D.; Dorfs, D.; Banin, U.; Della Sala, F.; Manna, L.; Millo, O., Determination of Band Offsets in Heterostructured Colloidal Nanorods Using Scanning Tunneling Spectroscopy. *Nano Lett.* **2008,***8*, 2954 - 2958;(c) Wu, K.; Rodrıguez-Cordoba, W. E.; Liu, Z.; Zhu, H.; Lian, T., Beyond Band Alignment: Hole Localization Driven Formation of Three Spatially Separated Long-Lived Exciton States in CdSe/CdS Nanorods. *ACS Nano* **2013,***7*, 7173 - 7185.
37. (a) Bailey, R. E.; Nie, S., Alloyed Semiconductor Quantum Dots: Tuning the Optical Properties without Changing the Particle Size. *J. Am. Chem. Soc.* **2003,***125*, 7100 - 7106;(b) Regulacio, M. D.; Han, M.-Y., Composition-Tunable Alloyed Semiconductor Nanocrystals. *Acc. Chem. Res.* **2010,***43*, 621–630;(c) Wei, S.-H.; Zhang, S. B.; Zunger, A., First-Principles Calculation of Band Offsets, Optical Bowings, and Defects in CdS, CdSe, CdTe, and Their Alloys. *J. Appl. Phys* **2000,***87*, 1304 - 1311.

38. Palik, E. D., *Handbook of Optical Constants of Solids*. Academic Press: 1998; Vol. II.
39. Ricard, D.; Chanassi, M.; Schanne-Klein, M., Dielectric Confinement and the Linear and Nonlinear Optical Properties of Semiconductor-Doped Glasses. *Opt. Commun.* **1996,***108*, 311 - 318.
40. (a) Wuister, S. F.; Houselt, A. v.; Donega, C. d. M.; Vanmaekelbergh, D.; Meijerink, A., Temperature Antiquenching of the Luminescence from Capped CdSe Quantum Dots. *Angew. Chem. Int. Ed.* **2004,***43*, 3029 -3033;(b) de Mello Donegá, C.; Bode, M.; Meijerink, A., Size- and temperature-dependence of exciton lifetimes in CdSe quantum dots. *Phys. Rev. B* **2006,***74*, 85320.
41. (a) Walker, G. W.; Sundar, V. C.; Rudzinski, C. M.; Wun, A. W.; Bawendi, M. G.; Nocera, D. G., Quantum-dot optical temperature probes. *App. Phys. Lett.* **2003,***83*, 3555;(b) Liu, T.-C.; Huang, Z.-L.; Wang, H.-Q.; Wang, J.-H.; Li, X.-Q.; Zhao, Y.-D.; Luo, Q.-M., Temperature-dependent photoluminescence of water-soluble quantum dots for a bioprobe. *Analytica Chimica Acta* **2006,***559*, 120;(c) Jones, M.; Lo, S. S.; Scholes, G. D., Signatures of Exciton Dynamics and Carrier Trapping in the Time-Resolved Photoluminescence of Colloidal CdSe Nanocrystals. *J. Phys. Chem. C* **2009,***113*, 18632-18642.
42. Valerini, D.; Cretí, A.; Lomascolo, M.; Manna, L.; Cingolani, R.; Anni, M., Temperature dependence of the photoluminescence properties of colloidal CdSe/ZnS core/shell quantum dots embedded in a polystyrene matrix. *Phys. Rev. B* **2005,***71*, 235409.
43. Zhao, Y.; Riemersma, C.; Pietra, F.; Koole, R.; Donega, C. d. M.; Meijerink, A., High-Temperature Luminescence Quenching of Colloidal Quantum Dots. *ACS Nano* **2012**, ASAP.
44. Ebenstein, Y.; Mokari, T.; Banin, U., Fluorescence quantum yield of CdSe/ZnS nanocrystals investigated by correlated atomic-force and single-particle fluorescence microscopy. *Appl. Phys. Lett.* **2002,***80*, 4033.
45. (a) Talapin, D. V.; Mekis, I.; Gotzinger, S.; Kornowski, A.; Benson, O.; Weller, H., CdSe/CdS/ZnS and CdSe/ZnSe/ZnS Core-Shell-Shell Nanocrystals. *J. Phys. Chem. B* **2004,***108*, 18826–18831;(b) Jiang, Z.-J.; Leppert, V.; Kelley, D. F., Static and Dynamic Emission Quenching in Core/Shell Nanorod Quantum Dots With Hole Acceptors. *J. Phys. Chem. C* **2009,***113*, 19161-19171.
46. Jasieniak, J.; Mulvaney, P., From Cd-Rich to Se-Rich - the Manipulation of CdSe Nanocrystal Surface Stoichiometry. *J. Am. Chem. Soc.* **2007,***129*, 2841-2848.
47. Gómez, D. E.; Embden, J. v.; Mulvaney, P.; Fernée, M. J.; Rubinsztein-Dunlop, H., Exciton−Trion Transitions in Single CdSe-CdS Core-Shell Nanocrystals. *ACS Nano* **2009,***3*, 2281-2287.
48. Efros, A. L.; Rosen, M., Electronic structure of semiconductor nanocrystals. *Ann. Rev. Matter. Sci.* **2000,***30*, 475.
49. Hartmann, L.; Kumar, A.; Welker, M.; Fiore, A.; Julien-Rabant, C.; Gromova, M.; Bardet, M.; Reiss, P.; Baxter, P. N. W.; Chandezon, F.; Pansu, R. B., Quenching Dynamics in CdSe Nanoparticles: Surface-Induced Defects upon Dilution. *ACS Nano* **2012**, ASAP.
50. (a) Woodbury, H. H.; Hall, R. B., Se self-diffusion in CdSe and the Defect Structure of the II-VI Compounds. *Phys. Rev. Lett.* **1966,***17*, 1093;(b) Shaw, D., Diffusion mechanisms in II-VI materials. *Journal of Crystal Growth* **1988,***86*, 778.
51. (a) Jiang, Z.-J.; Kelley, D. F., Hot and relaxed electron transfer from CdSe core and core/shell nanorods. *J. Phys. Chem. C* **2011,***115*, 4594–4602;(b) Klimov, V. I.; Milhailosky, A. A.; McBranch, D. W.; Leatherdale, C. A.; Bawendi, M. G., Mechanisms for intraband

relaxation in semiconductor quantum dots: The role of electron-hole interactions. *Phys. Rev. B* **2000,***61*, R13349;(c) Cooney, R. R.; Sewall, S. L.; Dias, E. A.; Sagar, D. M.; Anderson, K. E. H.; Kambhampati, P., Unified picture of electron and hole relaxation pathways in semiconductor quantum dots *Phys. Rev. B* **2007,***75*, 245311;(d) Xu, S.; Mikhailovsky, A. A.; Hollingsworth, J. A.; Klimov, V. I., Hole intraband relaxation in strongly confined quantum dots: Revisiting the "phonon bottleneck" problem. *Phys. Rev. B* **2002,***65*, 45319;(e) Burda, C.; Link, S.; Mohamed, M.; El-Sayed, M. A., The Relaxation Pathways of CdSe Nanoparticles Monitored with Femtosecond Time-Resolution from the Visible to the IR: Assignment of the Transient Features by Carrier Quenching. *J. Phys. Chem. B* **2001,***105*, 12286;(f) McGuire, J. A.; Joo, J.; Pietryga, J. M.; Schaller, R. D.; Klimov, V. I., New Aspects of Carrier Multiplication in Semiconductor Nanocrystals. *Acc. Chem. Res* **2008,***41*, 1810;(g) El-Sayed, M. A., Small Is Different: Shape-, Size-, and Composition-Dependent Properties of Some Colloidal Semiconductor Nanocrystals. *Acc. Chem. Res.* **2004,***37*, 326-333;(h) Mohamed, M. B.; Burda, C.; El-Sayed, M. A., Shape Dependent Ultrafast Relaxation Dynamics of CdSe Nanocrystals: Nanorods vs Nanodots. *Nano Lett.* **2001,***1*, 589.

52. Varshni, Y. P., Temperature Dependence of the Energy Gap in Semiconductors. *Physica* **1967,***34*, 149 - 154.

53. Nirmal, M.; Dabbousi, B. O.; Bawendi, M. G.; Macklin, J. J.; Trautman, J. K.; Harris, T. D.; Brus, L. E., Fluorescence intermittency in single cadmium selenide nanocrystals. *Nature* **1996,***383*, 802.

54. Kim, W.; Lim, S. J.; Jung, S.; Shin, S. K., Binary Amine-Phosphine Passivation of Surface Traps on CdSe Nanocrystals. *J. Phys. Chem. C* **2010,***114*, 1539-1546.

55. Hu, J.; Wang, L.-w.; Li, L.-s.; Yang, P.; Alivisatos, A. P., Semiempirical Pseudopotential Calculation of Electronic States of CdSe Quantum Rods. *J. Phys. Chem. B* **2002,***106*, 2447.

56. Liu, H.; Owen, J. S.; Alivisatos, A. P., Mechanistic Study of Precursor Evolution in Colloidal Group II-VI Semiconductor Nanocrystal Synthesis. *J. Am. Chem. Soc.* **2007,***129*, 305 - 312.

57. (a) Kalyuzhny, G.; Murray, R. W., Ligand Effects on Optical Properties of CdSe Nanocrystals. *J. Phys. Chem. B* **2005,***109*, 7012-7021;(b) Becerra, L. R.; Murray, C. B.; Griffin, R. G.; Bawendi, M. G., Investigation of the Surface Morphology of Capped CdSe Nanocrystallites by 31 P Nuclear Magnetic Resonance *J. Chem. Phys.* **1994,***100*, 3297-3300.

58. Anderson, N. C.; Hendricks, M. P.; Choi, J. J.; Owen, J. S., Ligand Exchange and the Stoichiometry of Metal Chalcogenide Nanocrystals: Spectroscopic Observation of Facile Metal-Carboxylate Displacement and Binding. *J. Am. Chem. Soc.* **2013,***135*, 18536−18548.

59. Leung, K.; Whaley, K. B., Surface Relaxation in CdSe Nanocrystals *J. Chem. Phys.* **1999,***110*, 11012-11022.

60. (a) Hines, D. A.; Kamat, P. V., Recent Advances in Quantum Dot Surface Chemistry *ACS Applied Materials and Interfaces* **2014,***6*, 3041-3057;(b) Abdellah, M.; Karki, K. J.; Lenngren, N.; Zheng, K.; Pascher, T.; Yartsev, A.; Pullerits, T., Ultra Long-Lived Radiative Trap States in CdSe Quantum Dots *J. Phys. Chem. C* **2014,***118*, 21682-21686;(c) Wheeler, D. A.; Zhang, J. Z., Exciton Dynamics in Semiconductor Nanocrystals. *Advanced Materials* **2013,***25*, 2878-2896;(d) Mooney, J.; Krause, M. M.; Saari, J. I.; Kambhampati, P., A Microscopic Picture of Surface Charge Trapping in Semiconductor Nanocrystals. *J. Chem. Phys.* **2013,***138*, 204705 - 204713;(e) Keene, J. D.; McBride, J. R.; Orfield, N. J.; Rosenthal, S. J., Elimination of Hole-Surface Overlap in Graded CdSxSe1-x Nanocrystals Revealed by

Ultrafast Fluorescence Upconversion Spectroscopy. *ACS Nano* **2014,***8*, 10665-10673;(f) Gómez-Campos, F. M.; Califano, M., Hole Surface Trapping in CdSe Nanocrystals: Dynamics, Rate Fluctuations, and Implications for Blinking. *Nano Lett.* **2012,***12*, 4508-4517;(g) Zhu, H.; Song, N.; Lian, T., Charging of Quantum Dots by Sulfide Redox Electrolytes Reduces Electron Injection Efficiency in Quantum Dot Sensitized Solar Cells. *J. Am. Chem. Soc.* **2013,***135*, 11461-11464;(h) Rowland, C. E.; Schaller, R. D., Exciton Fate in Semiconductor Nanocrystals at Elevated Temperatures: Hole Trapping Outcompetes Exciton Deactivation *J. Phys. Chem. C* **2013,***117*, 17337-17343;(i) Califano, M., Photoinduced Surface Trapping and the Observed Carrier Multiplication Yields in Static CdSe Nanocrystal Samples. *ACS Nano* **2011,***5*, 3614-3621.

61. Park, Y.-S.; Bae, W. K.; Pietryga, J. M.; Klimov, V. I., Auger Recombination of Biexcitons and Negative and Positive Trions in Individual Quantum Dots. *ACS Nano* **2014,***8*, 7288–7296.

62. Manceau, M.; Vezzoli, S.; Glorieux, Q.; Pisanello, F.; Giacobino, E.; Carbone, L.; De Vittorio, M.; Bramati, A., Effect of Charging on CdSe/CdS dot-in-Rods Single-Photon Emission. *Phys. Rev. B* **2014,***90*, 035311 - 35319.

63. Qin, W.; Liu, H.; Guyot-Sionnest, P., Small Bright Charged Colloidal Quantum Dots *ACS Nano* **2014,***8*, 283-291.

64. Jha, P. P.; Guyot-Sionnest, P., Trion Decay in Colloidal Quantum Dots. *ACS Nano* **2009,***3*, 1011-1015.

65. Qin, W.; Shah, R. A.; Guyot-Sionnest, P., CdSeS/ZnS Alloyed Nanocrystal Lifetime and Blinking Studies under Electrochemical Control. *ACS Nano* **2012,***6* 912-918.

66. (a) Cohn, A. W.; Rinehart, J. D.; Schimpf, A. M.; Weaver, A. L.; Gamelin, D. R., Size Dependence of Negative Trion Auger Recombination in Photodoped CdSe Nanocrystals. *Nano Lett., , (1), pp* **2014,***14*, 353-358;(b) Robel, I.; Gresback, R.; Kortshagen, U.; Schaller, R. D.; Klimov, V. I., Universal Size-Dependent Trend in Auger Recombination in Direct-Gap and Indirect-Gap Semiconductor Nanocrystals. *Phys. Rev. Lett.* **2009,***102*, 177404-177407;(c) Klimov, V. I.; Mikhailovsky, A. A.; McBranch, D. W.; Leatherdale, C. A.; Bawendi, M. G., Quantization of Multiparticle Auger Rates in Semiconductor Quantum Dots. *Science* **2000,** *287*, 1011-1013.

67. (a) Galland, C.; Ghosh, Y.; Steinbruck, A.; Sykora, M.; Hollingsworth, J. A.; Klimov, V. I.; Htoon, H., Two Types of Luminescence Blinking Revealed by Spectroelectrochemistry of Single Quantum Dots. *Nature* **2011,***479*, 203-207;(b) Galland, C.; Ghosh, Y.; Steinbrück, A.; Hollingsworth, J. A.; Htoon, H.; Klimov, V. I., Lifetime Blinking in Nonblinking Nanocrystal Quantum Dots. *Nature Communications* **2012,***3*, 908-914.

68. García-Santamaría, F.; Brovelli, S.; Viswanatha, R.; Hollingsworth, J. A.; Htoon, H.; Crooker, S. A.; Klimov, V. I., Breakdown of Volume Scaling in Auger Recombination in CdSe/CdS Heteronanocrystals: The Role of the Core-Shell Interface. *Nano Lett.* **2011,***11*, 687-693.

69. Gong, K.; Martin, J. E.; Shea-Rohwer, L. E.; Lu, P.; Kelley, D. F., Radiative Lifetimes of Zincblende CdSe/CdS Quantum Dots. *J. Phys. Chem. C* **2015,***119*, 2231-2238.

70. Pu, C.; Zhou, J.; Lai, R.; Niu, Y.; Nan, W.; Peng, X., Highly Reactive, Flexible Yet Green Se Precursor for Metal Selenide Nanocrystals: Se-Octadecene Suspension (Se-SUS). *Nano Res.* **2013,***6*, 652-670.

71. (a) Hassinen, A.; Moreels, I.; Nolf, K. D.; Smet, P. F.; Martins, J. C.; Hens, Z., Short-Chain Alcohols Strip X-Type Ligands and Quench the Luminescence of PbSe and CdSe

Quantum Dots, Acetonitrile Does Not. *J. Am. Chem. Soc.* **2012,***134*, 20705−20712;(b) Dai, M.-Q.; Yung, L.-Y. L., Ethylenediamine-Assisted Ligand Exchange and Phase Transfer of Oleophilic Quantum Dots: Stripping of Original Ligands and Preservation of Photoluminescence. *Chem. Mater.* **2013,***25*, 2193−2201.
72. Tu, H.; Mogyorosi, K.; Kelley, D. F., Intraband Spectroscopy and Photophysics in GaSe Nanoparticles. *Phys. Rev. B* **2005,***72*, 205306-205318.
73. (a) Chen, O.; Zhao, J.; Chauhan, V. P.; Cui, J.; Wong, C.; Harris, D. K.; HeWei; Han, H.-S.; Fukumura, D.; Jain, R. K.; Bawendi, M. G., Compact High-Quality CdSe-CdS Core-Shell Nanocrystals With Narrow Emission Linewidths and Suppressed Blinking. *Nature Materials* **2013,***12*, 445;(b) Hohng, S.; Ha, T., Near-Complete Suppression of Quantum Dot Blinking in Ambient Conditions. *J. Am. Chem. Soc.* **2004,***126*, 1324-1325;(c) Hammer, N. I.; Early, K. T.; Sill, K.; Odoi, M. Y.; Emrick, T.; Barnes, M. D., Coverage-Mediated Suppression of Blinking in Solid State Quantum Dot Conjugated Organic Composite Nanostructures. *J. Phys. Chem. B* **2006,***110*, 14167-14171.
74. (a) Chen, Y.; Vela, J.; Htoon, H.; Casson, J. L.; Werder, D. J.; Bussian, D. A.; Klimov, V. I.; Hollingsworth, J. A., "Giant" Multishell CdSe Nanocrystal Quantum Dots with Suppressed Blinking. *J. Am. Chem. Soc.* **2008,***130*, 5026–5027;(b) Qin, H.; Niu, Y.; Meng, R.; Lin, X.; Lai, R.; Fang, W.; Peng, X., Single-Dot Spectroscopy of Zinc-Blende CdSe/CdS Core/Shell Nanocrystals: Nonblinking and Correlation with Ensemble Measurements. *J. Am. Chem. Soc.* **2014,***136*, 179-187;(c) Wang, X.; Ren, X.; Kahen, K.; Hahn, M. A.; Rajeswaran, M.; Maccagnano-Zacher, S.; Silcox, J.; Cragg, G. E.; Efros, A. L.; Krauss, T. D., Non-Blinking Semiconductor Nanocrystals. *Nature* **2009,***454*, 686;(d) Spinicelli, P.; Buil, S.; Que´lin, X.; Mahler, B.; Dubertret, B.; Hermier, J.-P., Bright and Grey States in CdSe-CdS Nanocrystals Exhibiting Strongly Reduced Blinking. *Phys. Rev. Lett.* **2009,***102*, 136801;(e) Mahler, B.; Spiniclli, P.; Buil, S.; Quelin, X.; Hermier, J.-P.; Dubertret, B., Towards Non-Blinking Colloidal Quantum Dots. *Nature Materials* **2008,***7*, 659.
75. (a) Shchukin, V. A.; Ledentsov, N. N.; Kop'ev, P. S.; Bimberg, D., Spontaneous Ordering of Arrays of Coherent Strained Islands. *Phys. Rev. Lett.* **1995,***75*, 2968;(b) Daruka, I.; Barabási, A.-L., Dislocation-Free Island Formation in Heteroepitaxial Growth: A Study at Equilibrium. *Phys. Rev. Lett.* **1997,***79*, 3708.
76. (a) Williams, R. S.; Medeiros-Rebeiro, G.; Kamins, T. I.; Ohlberg, D. A. A., Equilibrium Shape Diagram for Strained Ge Nanocrystals on Si(001). *J. Phys. Chem. B* **1998,***102*, 9605-9609;(b) Rudd, R. E.; Briggs, G. A. D.; Sutton, A. P.; Medeiros-Ribeiro, G.; Williams, R. S., Equilibrium Model of Bimodal Distributions of Epitaxial Island Growth. *Phys. Rev. Lett.* **2003,***90*, 146101-146104;(c) Williams, R. S.; Medeiros-Rebeiro, G.; Kamins, T. I.; Ohlberg, D. A. A., Chemical Thermodynamics of the Size and Shape of Strained Ge Nanocrystals Grown on Si(001). *Acc. Chem. Res.* **1999,***32*, 425–433;(d) Eisenberg, H. R.; Kandel, D., Formation, Ripening, And Stability of Epitaxially Strained Island Arrays. *Phys. Rev. B* **2005,***71*, 115423.
77. (a) Ithurria, S.; Guyot-Sionnest, P.; Mahler, B.; Dubertret, B., Mn2+ as a Radial Pressure Gauge in Colloidal Core/Shell Nanocrystals. *Phys. Rev. Lett.* **2007,***99*, 265501;(b) Ithurria, S.; Guyot-Sionnest, P.; Mahler, B.; Dubertret, B., Radial Pressure Measurement In Core/Shell Nanocrystals. *Proc. of SPIE* **2009,***7189*, 718908;(c) Duan, H. L.; Karihaloo, B. L.; Wang; Yi, X., Strain Distributions in Nano-Onions With Uniform and Non-Uniform Compositions. *Nanotechnology* **2006,***17*, 3380.

78. Hines, M. A.; Guyot-Sionnest, P., Synthesis and characterization of strongly luminescent ZnS-capped CdSe nanocrystals. *J. Phys. Chem.* **1996,***100*, 468.
79. Yu, Z.; Guo, L.; Du, H.; Krauss, T.; Silcox, J., Shell Distribution on Colloidal CdSe/ZnS Quantum Dots. *Nano Lett.* **2005,***5*, 565–570.
80. (a) Dabbousi, B. O.; Rodriguez-Viejo, J.; Mikulec, F. V.; Heine, J. R.; Mattoussi, H.; Ober, R.; Jensen, K. F.; Bawendi, M. G., (CdSe)ZnS Core−Shell Quantum Dots: Synthesis and Characterization of a Size Series of Highly Luminescent Nanocrystallites. *J. Phys. Chem. B* **1997,***101*, 9463;(b) Mokari, T.; Banin, U., Synthesis and Properties of CdSe/ZnS Core/Shell Nanorods. *Chem. Mater.* **2003,***15*, 3955 - 3960.
81. (a) Zhang, J.; Zhang, X.; Zhang, J. Y., Dependence of Microstructure and Luminescence on Shell Layers in Colloidal CdSe/CdS Core/Shell Nanocrystals. *J. Phys. Chem. C* **2010,***114*, 3904;(b) Chen, X.; Lou, Y.; Samia, A. C.; Burda, C., Coherency Strain Effects on the Optical Response of Core/Shell Heteronanostructures. *Nano Lett.* **2003,***3*, 799.
82. (a) Simashkevich, A. V.; Tsiulyanu, R. L., Liquid-phase epitaxy of CdSe, ZnSe and ZnTe layers *J. Crystal Growth* **1976,***35*, 269-272 ;(b) Gashin, P. A.; Sherban, D. A.; Simashkevich, A. V., Radiative recombination in ZnTe-CdSe and ZnSe-CdTe heterojunctions *J. Lumin.* **1977,***15*, 109-113 ;(c) Xie, R.; Zhong, X.; Basché, T., Synthesis, Characterization, and Spectroscopy of Type-II Core/Shell Semiconductor Nanocrystals with ZnTe Cores. *Adv. Mater.* **2005,***17*, 2741–2745.
83. Cai, X.; Martin, J. E.; Shea-Rohwer, L. E.; Gong, K.; Kelley, D. F., Thermal Quenching Mechanisms in II–VI Semiconductor Nanocrystals. *J. Phys. Chem. C* **2013,***117* (15), 7902-7913.
84. (a) Banerjee, S.; Jia, S.; Kim, D. I.; Robinson, R. D.; Kysar, J. W.; Bevk, J.; Herman, I. P., Raman Microprobe Analysis of Elastic Strain and Fracture in Electrophoretically Deposited CdSe Nanocrystal Films. *Nano Lett.* **2006,***6*, 175;(b) Consonni, V.; Feuillet, G.; Gergaud, P., Plasticity induced texture development in thick polycrystalline CdTe: Experiments and modeling *J. Appl. Phys.* **2008,***103*, 63529.
85. John, R.; Catherine, D. H.; Pushpalata, S., Theoretical investigations on II-VI binary semiconductors. *Chalcogenide Lett* **2010,***7*, 263-268.
86. Reimann, K.; Haselhoff, M.; Rübenacke, S.; Steube, M., Determination of the Pressure Dependence of Band-Structure Parameters by Two-Photon Spectroscopy. *physica status solidi (b)* **1996,***198* (1), 71-80.
87. van Embden, J.; Jasieniak, J.; Gómez, D. E.; Mulvaney, P.; Giersig, M., Review of the Synthetic Chemistry Involved in the Production of Core/Shell Semiconductor Nanocrystals. *Aust. J. Chem.* **2007** *60*, 457 - 471.
88. Villa-Angulo, J. R.; Villa-Angulo, R.; Solorio-Ferrales, K.; Ahumada-Valdez, S. E.; Villa-Angulo, C., Effect of effective mass mismatch in CdS/CdTe heterojunctions on the fundamental design parameters of nanophotonic devices. *NANOP* **2014,***8* (1), 083096-083096.
89. (a) Bernard, J. E.; Zunger, A., Electronic structire of ZnS, ZnSe, ZnTe and their pseudobinary alloys. *Phys. Rev. B* **1987,***36*, 3199;(b) Muthukumarasamy, N.; Jayakumar, S.; Kannan, M. D.; Balasundaraprabhu, R., Structural phase change and optical band gap bowing in hot wall deposited CdSexTe1−x thin films. *Solar Energy* **2009,***83* (4), 522-526.
90. Swafford, L. A.; Weigand, L. A.; Bowers, M. J.; McBride, J. R.; Rapaport, J. L.; Watt, T. L.; Dixit, S. K.; Feldman, L. C.; Rosenthal, S. J., Homogeneously Alloyed

CdSxSe1-x Nanocrystals: Synthesis, Characterization, and Composition/Size-Dependent Band Gap. *Journal of the American Chemical Society* **2006,***128*, 12299-12306.
91. Geller, M. R.; Kohn, W., Quantum Mechanics of Electrons in Crystals with Graded Composition. *Phys. Rev. Lett.* **1993,***70*, 3103.
92. Zhu, H.; Song, N.; Lian, T., Controlling Charge Separation and Recombination Rates in CdSe/ZnS Type I Core−Shell Quantum Dots by Shell Thicknesses. *J. Am. Chem. Soc.* **2010,***132*, 15038-15045.
93. Madelung, O.; Rossler, U.; Schultz, M., *II-VI and I-VII Compounds, Landolt-Börnstein* Springer 1999; Vol. 41B.
94. (a) Talapin, D. V.; Rogach, A. L.; Kornowski, A.; Haase, M.; Weller, H., Highly Luminescent Monodisperse CdSe and CdSe/ZnS Nanocrystals Synthesized in a Hexadecylanine-Trioctylphosphine Oxide-Trioctylphosphine Mixture. *Nano Lett.* **2001,***1*, 207;(b) Banin, T. M. a. U., Synthesis and Properties of CdSe/ZnS Core/Shell Nanorods. *Chem. Mater.* **2003,***15*, 3955–3960;(c) Protiere, M.; Reiss, P., Highly Luminescent Cd1-xZnxSe/ZnS Core/Shell Nanocrystals Emitting in the Blue-Green Spectral Range. *Small* **2007,***3*, 399;(d) Baranov, A. V.; Rakovich, Y. P.; Donegan, J. F.; Perova, T. S.; Moore, R. A.; Talapin, D. V.; Rogach, A. L.; Masumoto, Y.; Nabiev, I., Effect of ZnS shell thickness on the phonon spectra in CdSe quantum dots. *Phys. Rev. B* **2003,***68*, 165306.
95. (a) Groeneveld, E.; Witteman, L.; Lefferts, M.; Ke, X.; Bals, S.; Tendeloo, G. V.; Donega, C. d. M., Tailoring ZnSe-CdSe Colloidal Quantum Dots via Cation Exchange: From Core/Shell to Alloy Nanocrystals. *ACS Nano* **2013,***7*, 7913;(b) Panda, S. K.; Hickey, S. G.; Waurisch, C.; Eychmuller, A., Gradated alloyed CdZnSe nanocrystals with high luminescence quantum yields and stability for optoelectronic and biological applications. *J. Mater. Chem.* **2011,***21*, 11550;(c) Sung, Y.-M.; Lee, Y.-J.; Park, K.-S., Kinetic Analysis for Formation of Cd1-xZnxSe Solid-Solution Nanocrystals. *J. Am. Chem. Soc.* **2006,***128*, 9002;(d) Zhong, X.; Han, M.; Dong, Z.; White, T. J.; Knoll, W., Composition-Tunable ZnxCd1-xSe Nanocrystals with High Luminescence and Stability. *J. Am. Chem. Soc.* **2003,***125*, 8589-8594.
96. Gong, K.; Kelley, D. F., A Predictive Model of Shell Morphology in CdSe/CdS Core/Shell Quantum Dots. *J. Chem. Phys.* **2014,***141*, 194704 - 194712.
97. Gong, K.; Kelley, D. F., A predictive model of shell morphology in CdSe/CdS core/shell quantum dots. *J. Chem. Phys.* **2014,***141* (19), 194704.
98. Berger, L. I., *Semiconducting Materials*. CRC Press: 1997.

APPENDIX. SUPPORTING INFORMATION

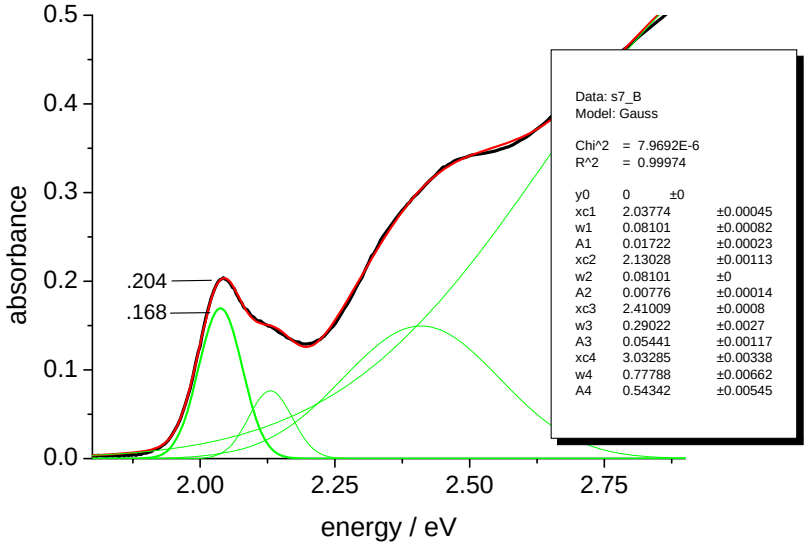

Figure SI-1. An example of a four Gaussian fit to the absorption spectrum of 5.0 nm CdSe QDs. The width of the two lowest transitions has been constrained to be the same. The extinction coefficient correction factor in this case is 0.823 (= .168/.204).

We note that the effect of overlapping transitions becomes more significant for the larger particles, in which the $1S_e$-$1S_{3/2}$ and $1S_e$-$2S_{3/2}$ transitions are more closely spaced. The result is that simply taking the product of the maximum extinction coefficient and the spectral width gives a good estimate of the integrated extinction coefficients only for the smallest particles. An increasingly large correction must be applied to this estimate for the larger particles.

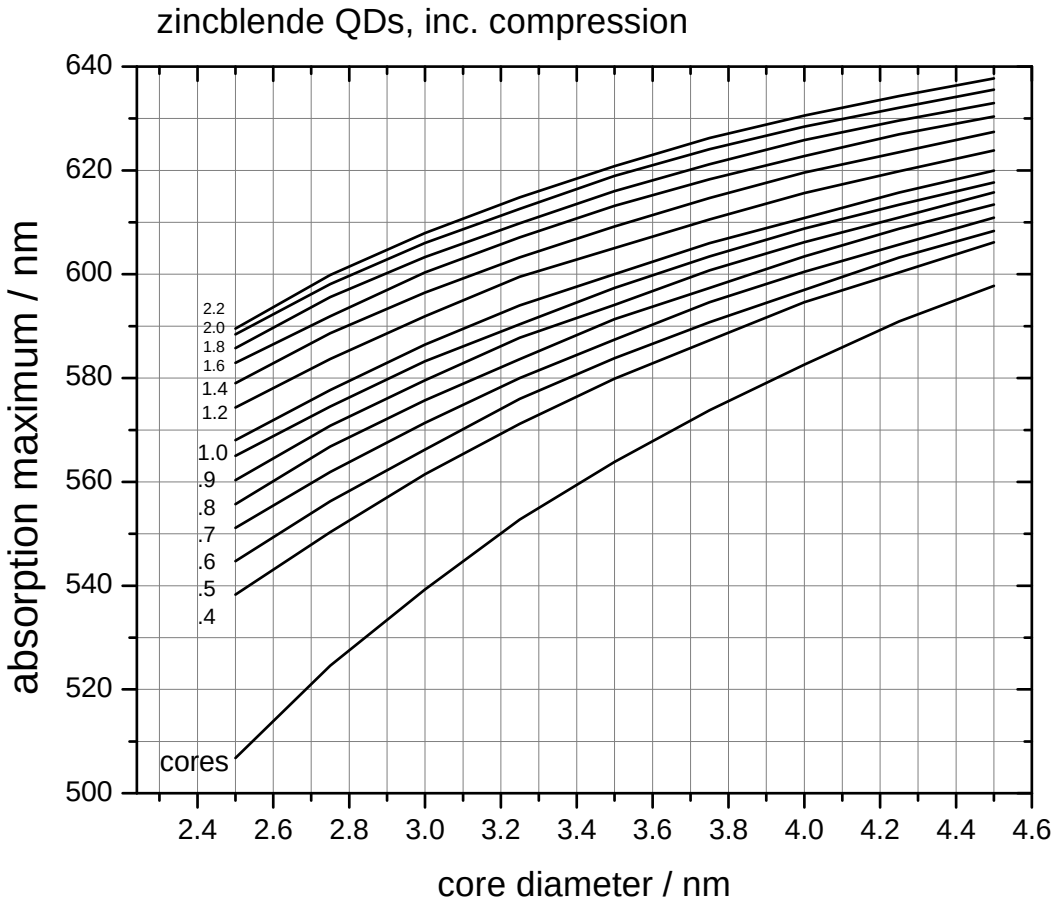

Figure SI-2. Exciton wavelength map assuming no core-shell interdiffusion and core compression calculated with bulk elastic parameters.

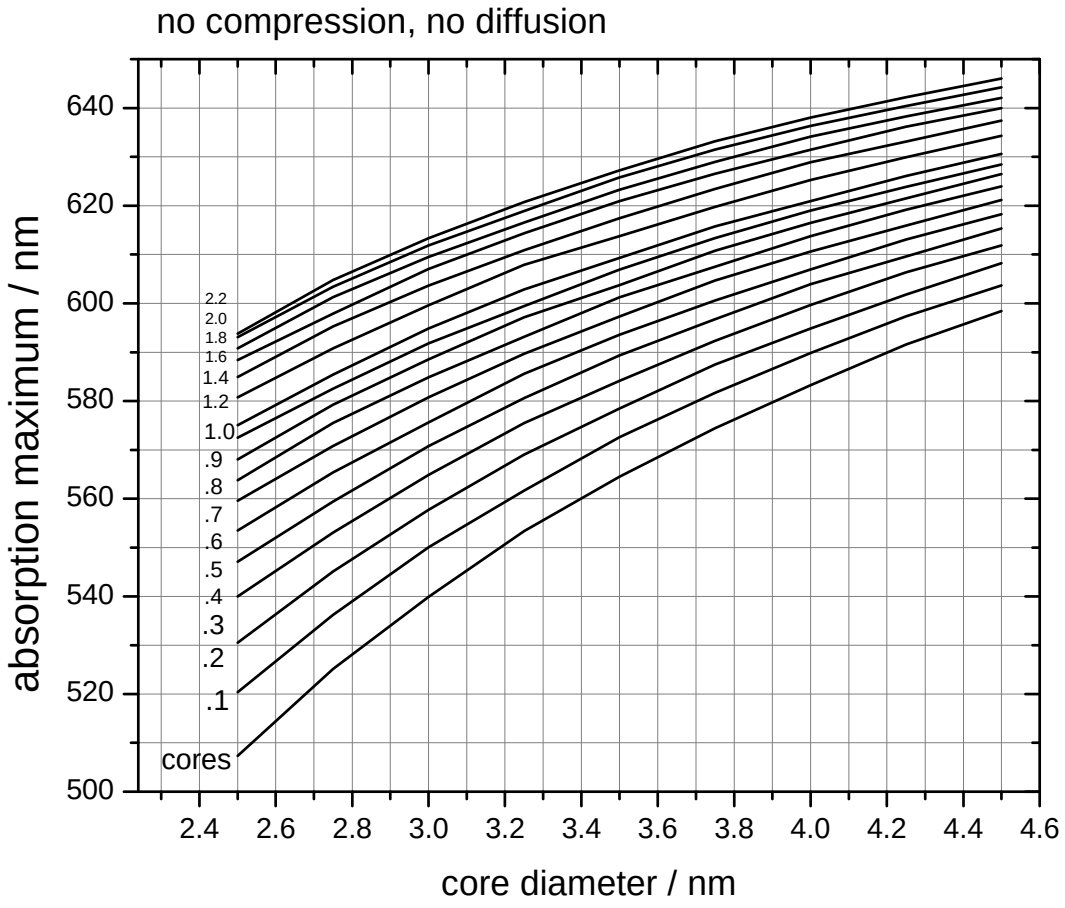

Figure SI-3. Exciton wavelength map assuming no core-shell interdiffusion and no core compression.

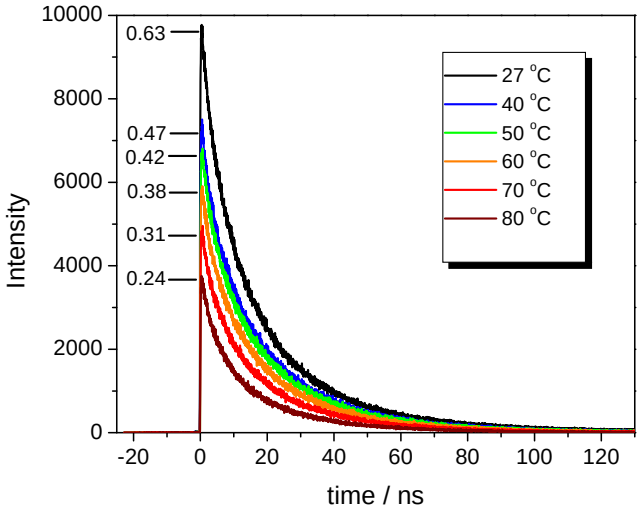

Figure SI-4. Decay curves obtained at different temperatures for CdSe/ZnSe nanoparticles (3.5 nm diameter cores with 1.0 nm thick shells) having TBP/ODA ligands. Also shown are the fractions of bright particles at each temperature. The areas under the curves can be accurately determined from these data.

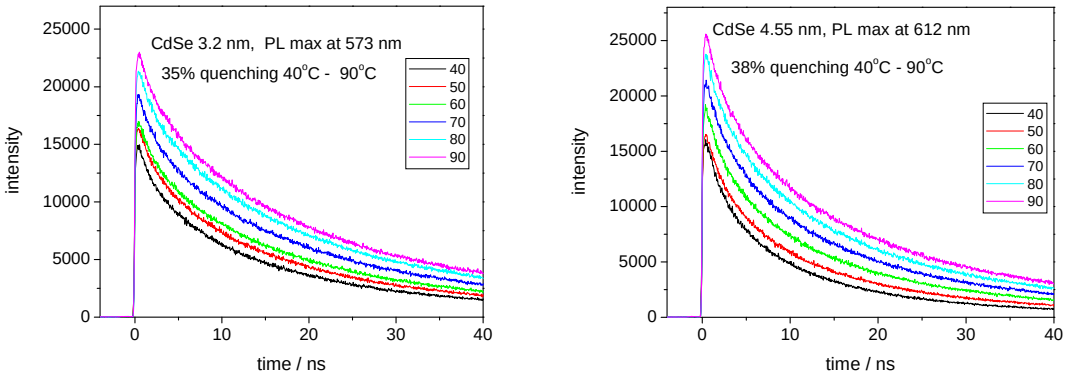

Figure SI-5. Thermal quenching over a range of 40 °C to 90°C for 3.2 nm (left panel) and 4.55 nm (right panel) CdSe particles. The 3.2 and 4.55 nm particles exhibit 35% and 38 % static thermal quenching, respectively, over that temperature range.

CdTe/CdSe thermal quenching.

CdTe/CdSe core/shell particles are type-II, with the hole localized in the core and the electron localized in the shell. Figure S1 shows that as a result of hole localization in the (lower energy) CdTe core, these particles exhibit somewhat less thermal quenching the do CdSe particles.

One can also consider the effects of temperature-dependent band shifts in the thermal quenching of these particles. The band gap shifts are primarily due to temperature-dependent changes in the volume of the unit cell, defined as $\alpha = \frac{\partial E_g}{\partial \ln V}$. Most of the band gap shift is due to changes in the conduction band. Values of α are -3.7 and -2.3 eV for CdTe and CdSe, respectively[35c]. The temperature dependent changes in the conduction band offset can be calculated using these values and the coefficients of thermal volume expansion, which are 1.47 x 10^{-5}/K and 0.93 x 10^{-5}/K for CdTe and CdSe, respectively.[98] We get that the conduction bands shift by 2.14 x 10^{-5} and 5.44 x 10^{-5} eV/K. The conclusion is that the difference in the CdTe and CdSe conduction band energies over the 22 ºC – 80 ºC range studied here is about 1.8 meV, which compared to the approximately 300 meV offset at room temperature, is negligible.

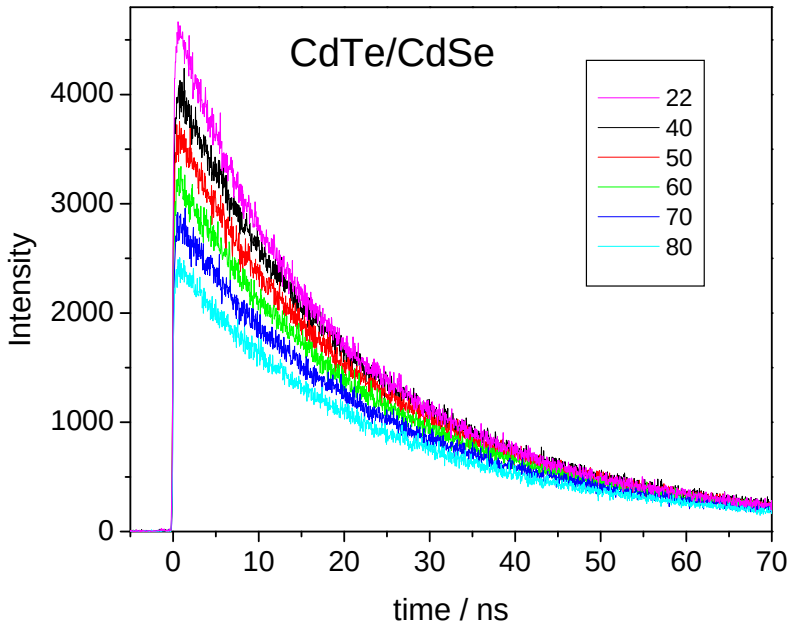

Figure SI-6. Temperature dependent PL decay curves for CdTe/CdSe particles consisting of an approximately 3.4 nm CdTe core with a two layer (0.62 nm) CdSe shell.

Excitation wavelength effects.

Excitation wavelength has no effect on the extent of thermal quenching as shown below.

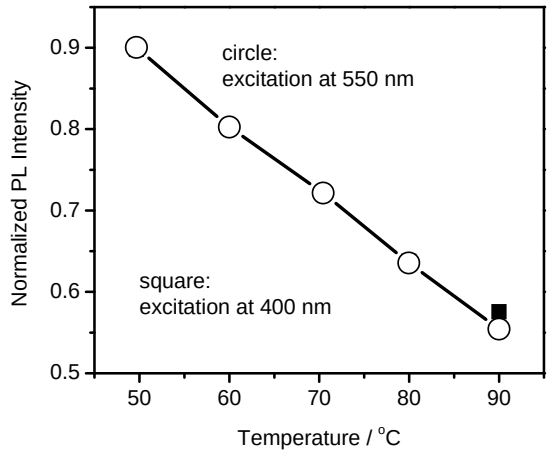

Figure SI-7. Normalized PL intensities as a function of temperature following excitation at 400 (squares) and 550 nm (circles).

Ligand exchange of CdSe and CdSe/ZnSe particles.

Ligand exchange has been shown to result in small blue shifts as a result of removing pendant surface metal and chalcogenide atoms.[54] In the case of CdSe/ZnSe particles, removal of the most weakly bound surface atoms have little effect on the absorption spectrum shows below.

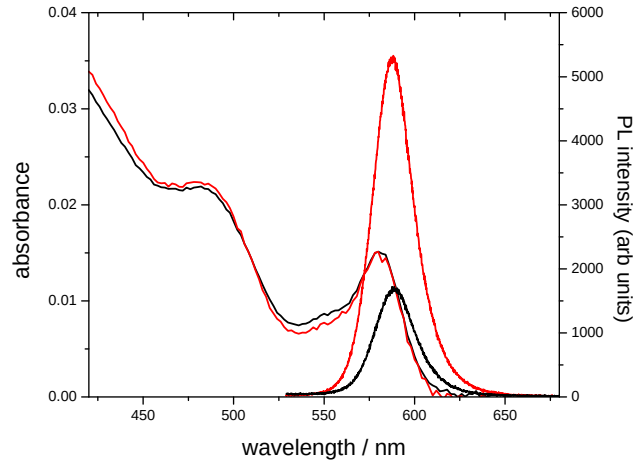

Figure SI-8. Absorption and PL spectra of CdSe/ZnSe as synthesized (black curves) and following TBP/ODA ligand exchange (red curves). The only significant difference following ligand exchange is the increase in PL intensity.